Surface Morphology Characterization of Industrial Zinc Electrodeposits as a Function of Chemical Additives Using Atomic Force Microscopy and Scaling Analysis

By

Said Sharif Mahboob

A thesis submitted in partial fulfillment of the requirements for the degree of Master of Science (M.Sc.) in Chemical Sciences

The Faculty of Graduate Studies

Laurentian University

Sudbury, Ontario, Canada

THESIS DEFENCE COMMITTEE/COMITÉ DE SOUTENANCE DE THÈSE
Laurentian Université/Université Laurentienne
Faculty of Graduate Studies/Faculté des études supérieures

Title of Thesis Titre de la thèse	Surface Morphology Characterization of Industrial Zinc Electrodeposits as a Function of Chemical Additives Using Atomic Force Microscopy and Scaling Analysis
Name of Candidate Nom du candidat	Mahboob, Said Sharif
Degree Diplôme	Master of Science
Department/Program Département/Programme	Chemical Sciences
Date of Defence Date de la soutenance	November 16, 2017

APPROVED/APPROUVÉ

Thesis Examiners/Examinateurs de thèse:

Dr. Jeffrey Shepherd
(Supervisor/Directeur de thèse)

Dr. M'hamed Chahma
(Committee member/Membre du comité)

Dr. Gustavo Arteca
(Committee member/Membre du comité)

Dr. Michael Moats
(External Examiner/Examinateur externe)

Approved for the Faculty of Graduate Studies
Approuvé pour la Faculté des études supérieures
Dr. David Lesbarrères
Monsieur David Lesbarrères
Dean, Faculty of Graduate Studies
Doyen, Faculté des études supérieures

ACCESSIBILITY CLAUSE AND PERMISSION TO USE

Abstract

The influence of chemical additive and deposition time on the morphology of short-time zinc electrodeposits was studied using Scanning Electron Microscopy (SEM), Atomic Force Microscopy (AFM) and scaling analysis. SEM and AFM were utilized to capture high-resolution images of zinc samples produced between 10 and 90 minutes of deposition from an electrolyte with a composition similar to that being used in the industry. Scaling analysis of the 3D AFM images was used to quantify surface roughness including root-mean-squared (*rms*) roughness, feature widths, roughness to width ratios, and their rates of change. Insight on the growth mechanism for these short-term deposits was achieved using scaling analysis. Within the deposition conditions studied, results showed that zinc deposit morphology is influenced by the relative proportions of bone glue, sodium silicate and licorice additives.

Keywords: Zinc Deposition, Atomic Force Microscopy (AFM), Scaling Analysis, Electrowinning, Leveling Agents

Dedication

To the memory of my grandmother and niece, both of whom passed away during my time away from them. I miss you both greatly and trust that you are resting in peace.

Acknowledgements

Firstly, I would like to express my most sincere appreciation and thanks to my supervisor and mentor Dr. Jeffrey L. Shepherd for the endless support, guidance and patience during my M.Sc. study. Furthermore, I thank Dr. Shepherd for providing me with the knowledge, skills and training to be able to conduct this research to completion.

Also, I would like to thank Teck Metals Ltd (Teck) and, in particular, Dr. José Alberto Gonzalez for providing the opportunity for a wonderful research project and Presley Hlushak for sending samples, electrolytes, and additives to conduct this research.

My sincere thanks also goes to Dr. Eduard Guerra from the Bharti School of Engineering at Laurentian University for his informative, motivating and supportive conversations regarding this project.

I thank Prof. Gustavo Arteca for his patience and invaluable time that he took to go over key scaling theory concepts with me. Furthermore, I thank him and Dr. M'hamed Chahma for being supportive graduate committee members.

As well, I am grateful to Prof. Hélène Joly for always being supportive and providing guidance and mentoring to me during my time at Laurentian University. I would like to acknowledge that it was her suggestion that lead me to Dr. Shepherd's research group and I thank her endlessly.

I would like to acknowledge and thank Luc Beaudet, François Brunet, Kevin Chartrand, Paul Guérin and Adam Walli, Technologists, at Laurentian University for always being willing to provide help.

In addition I would like to acknowledge the Goodman School of Mines for granting me a very generous scholarship which allowed me to focus exclusively on my studies and research. This project was also funded in part by Natural Sciences and Engineering Research Council Canada (NSERC). Also, I thank the Department of Chemistry and Biochemistry at Laurentian University for their numerous awards and scholarships which motivated and provided me with financial assistance.

Last but by no measure the least, I would like to thank my family: my parents for their sacrifices and support throughout my life and in particular during this stage. Also, I thank my sister and brother for always showing their support and stating their pride in me.

Table of Contents

List of Tables

List of Figures

Abbreviations and Symbols

δ/L_c	Limiting Roughness/Critical Length. Related to aspect ratio
AFM	Atomic Force Microscopy
ACF	Autocovariance function
L_c	Critical length
CE	Current Efficiency
δ	Limiting roughness
γ	Optical roughness exponent
ξ	Root-mean-squared deviation (rmsd)
SEM	Scanning Electron Microscopy
SPD	Spectral power density
α	Static growth exponent
β	Temporal growth exponent
3D	Three-dimensional
M	mass recovered in grams (g)
Q	total electric charge in coulombs (C)
F	Faraday constant (96485 C mol^{-1})
z	# of electrons passed
I	Current (A)
L	Scaling length

Chapter 1: Introduction

Zinc is the 24th most abundant element on earth and due to its electrochemical properties, low cost and availability it has a wide variety of applications. It is used to make brass (zinc-copper alloy) as well as galvanized steel and batteries. Also, its oxide is useful in paints, rubber production, hygiene and cosmetic products and pharmaceuticals, to name a few examples [1]. As such, the production of zinc is very important and necessary in modern civilization.

Historically, pyrometallurgical approaches were used to produce zinc from zinc carbonate ores where the physical properties of zinc such as its specific gravity (7.133g cm^{-3}), melting (419.5°C) and boiling (907°C) points were exploited during the production process [1]. However, recent advances in hydrometallurgical and electrolytic technologies have allowed the extraction of zinc from zinc sulfides ores, which are the major zinc containing raw material [2]. While the entire extraction process is detailed, it will at some stage result in zinc ions dissolved in solution which must be recovered and this is typically achieved through electrodeposition. This is an electrolytic process where zinc is electrocrystallized on to a substrate with a hexagonal close packed (HCP) structure [1]. While the history of zinc production is broad, the focus and results of this thesis will be mainly on the electrodeposition recovery method, also known as electrowinning. That said, a brief history of zinc production is presented in the following sections ending with the current understanding of electrowinning and the issues that may be encountered during this process of producing zinc.

1.1 A brief history of zinc

The metallurgy of zinc and its history have been described in great detail in the literature [2]. In this section of the thesis, a brief outline of it is presented. Zinc metal production has been performed since before the 14th century on the Asian continent, by the 18th century in Europe and by the 20th century in North America. The technology and procedures involved in the production of zinc metal have evolved with time. Historically, a pyrometallurgical process called retorting was used to produce zinc metal until the early 20th century when a new electrolytic process was developed. The electrolytic process, termed electrowinning, results in higher yields with relatively lower energy and labour requirements, hence it is employed to produce over 80 percent of today's zinc metal. Early production of zinc used mostly zinc carbonates since zinc sulphide ores were not desired due to the presence of other species such as lead, copper, and iron. Separation techniques at that time used specific gravity which allowed for easy separation of lead due to the large difference in its specific gravity and therefore sulphide ores were mostly used to produce lead. Once discovery of large zinc sulphide resources occurred, it prompted advancements in separation techniques which lead to the development of the froth flotation process. This separation technique allowed for differential mineral separation causing zinc sulphide ores to be the major raw material for the zinc production industry today. Sphalerite is in fact the major zinc containing ore at 67.1% zinc content [2] but a list of other zinc containing minerals is presented in Table 1.

Table 1. Zinc containing minerals and percent Zn content (data from [2]**)**

Mineral	Formula	Zinc content (%)
Sphalerite, Zinc Blende or Wurtzite	ZnS	67.1
Marmatite (iron in solid solution)	$(Zn, Fe)S$	< 67.0
Smithsonite or 'Calamine'	$ZnCO_3$	52.2
Hydrozincite	$3ZnO \cdot 2ZnCO_3 \cdot 3H_2O$	59.5
Willemite	$2ZnO \cdot SiO_2$	58.7
Hemimorphite	$4ZnO \cdot 2SiO_2 \cdot 2H_2O$	54.3
Zincite	ZnO	80.4

1.2 Zinc solution purification process

There are four main stages involved in the conventional process of zinc solution purification that are depicted in Figure 1. In the first stage, the sulfide ore is crushed to fine particles that go through a separation technique called froth flotation. Here, the different minerals in the ore are made into their respective concentrates and after flotation the zinc concentrate is ~50 percent zinc [2]. In the second stage, the zinc sulfide (ZnS) concentrate is roasted in an air and oxygen rich environment to separate the sulfide and produce zinc oxide. In the third stage the zinc oxide is leached in various steps using acid thereby

dissolving the zinc into an aqueous solution. The fourth and final stage before electrowinning takes place is further purification to remove metallic impurities.

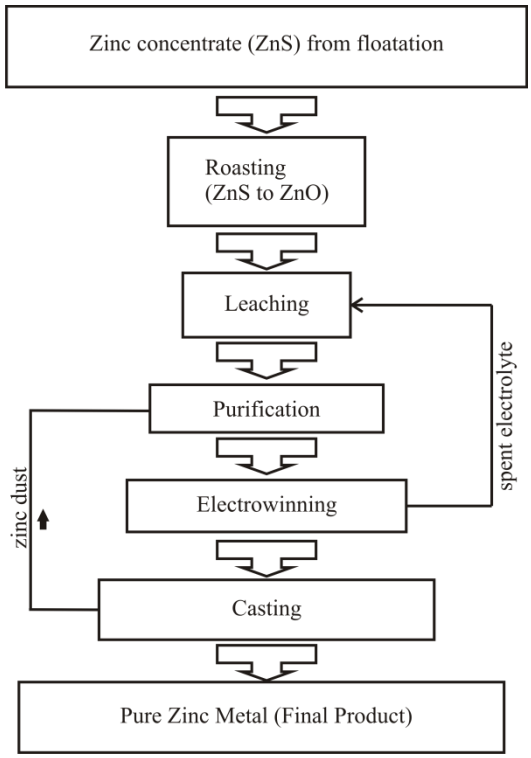

Figure 1: Flow chart for the process of zinc solution preparation and electrowinning

1.2.1 Froth flotation

Separation by froth flotation has been used in a range of industries such as metal (Cu, Pb, Zn, Co, Ni, Mo, Sb, etc.), chemical (CaF_2, $BaSO_4$, NaCl, KCl, S, alumina, silica, clay, etc.), paper (removal of ink from recycled paper) and gasoline (from oil sands) production [3]. The steps involved in the process of froth flotation have been described in detail [3] and here only a summary is presented.

Flotation, as it is commonly referred to, takes advantage of the principles of separation by hydrophobicity. In the mining industry, and as related to this thesis, metal ores are ground to very fine particles (maximum size less than 300 μm) and in the case of sulfide mineral particles smaller than 10 μm make this process less effective and therefore this size is considered as the minimum. Once a slurry/flotation pulp of particulates with the appropriate size and water content is achieved then separation can take place. The sequential separation of each constituent into a concentrate is achieved by changing the hydrophobicity of the particles through pH adjustments. This prepares the surfaces of particles for addition of two types of modifying agents that include both a depressant and activator. Depressant modifying agents ensure that the particles designed to be hydrophilic will maintain this physical property within the bulk, whereas activators are used to make other particles hydrophobic and float to the top of the bulk solution. Once these hydrophobic particles are on the top layer of the solution, a third agent labelled as frother (surfactants) cause the hydrophobic layer to be attached to air bubbles, thereby producing a top layer of froth or foam when the mixture slurry is aerated. In frothing of zinc sulphide ores, dithiophosphates and xanthates are used as frothing agents [2,3]. Moreover, pH control of the slurry is most important in a successful selective separation because the surfactants that act as frothers have a certain range of pH which allows them to be more effective in frothing.

1.2.2 Roasting zinc concentrate (ZnS)

Once the ZnS concentrate is gathered from flotation, it is treated with a process known as roasting that is used to separate the zinc from the sulfide. Fluid bed roasters are used to

oxidize the ZnS concentrate at temperatures of 900 to1000°C. This produces zinc oxide (ZnO), also known as calcine, and a by-product sulfur dioxide (SO_2) [2] as shown in equation 1.1. The by-product can be used to produce sulfuric acid which can be useful in the zinc leaching process.

$$ZnS + \frac{3}{2}O_2 \leftrightarrow ZnO + SO_2 \qquad 1.1$$

1.2.3 Leaching

In this step the calcine is purified as a zinc sulfate solution which is used in electrowinning. Leaching normally occurs in multiple reaction vessels; at least four different leaching tanks are used [2]. Typically, the calcine is mostly ZnO, however it can also contain zinc ferrite (iron complex), zinc silicates and to some other sulfides. As such, purification and removal of impurities is required during the leaching of zinc and the process is controlled by the pH and temperature of the leaching solutions [2,4].

The primary steps of leaching are called neutral and weak-acid leach. During primary leaching, calcine is mixed with spent electrolyte (containing sulfuric acid) and the pH is kept between 4 and 5.5 with the temperature maintained near 60°C. This produces an impure solution of zinc sulphate, as shown in equation 1.2 and is further purified in a later step.

$$ZnO + H_2SO_4 \leftrightarrow ZnSO_4 + H_2O \qquad 1.2$$

During secondary leaching, hot acid and strong acid leaching are used to remove iron impurities that may exist as jarosite ($R_2 Fe_6(SO_4)_4(OH)_{12}$ where R may be K^+, NH_4^+, Na^+, Ag^+, or Pb^{2+}), Hematite (Fe_2O_3) or goethite ($FeO{\cdot}OH$). Extreme conditions are used during this step, including high sulfuric acid concentrations compared to the primary leaching steps and a temperature ≥ 90°C [2,4]. The processes for removal of iron are discussed in detail in [2]. After secondary leaching the zinc solutions are further purified.

1.2.4 Purification of impure zinc solution

The resulting impure zinc sulfate solution from the primary leaching steps is further purified until it is suitable for electrowinning through cementation. During which copper, cadmium, cobalt and nickel impurities are removed [2,4]. Impurities result in lower current efficiency and grade of final product which is highly undesirable.

The final purified zinc sulfate solution, which contains 160 g L^{-1} $ZnSO_4$ and impurities less than 1 mg L^{-1}, is named "neutral feed" [4]. Now this purified aqueous solution of $ZnSO_4$ is used to recover the zinc metal through electrowining.

1.3 Industrial electrowining background

Electrowinning is not restricted to zinc production and it is a method employed around the world by various mining companies to produce many base metals. In this approach, the metal ions are dissolved in an aqueous solution from which they are recovered using electricity. Here, the positively charged metal ions in solution are fluxed towards a negatively charged substrate where they are reduced and deposited as a solid metal onto the

surface. This process follows Faradays law (Eq. 1.3) of electrolysis from a complex electrolyte:

$$m=\left(\frac{Q}{F}\right)\left(\frac{M}{z}\right) \qquad 1.3$$

where:

- m is the mass recovered in grams (g)
- Q is total electric charge in coulombs (C)
- F is the Faraday constant (96485 C mol^{-1})
- M is the molar mass (g mol^{-1})
- z is the number of electrons transferred in the electrochemical half reaction.

During electrowinning, fresh neutral feed is mixed with spent electrolyte which may contain a host of chemical additives. The deposition occurs onto a conductive substrate at a desired pH and temperature range to produce a solid metal product, which is then separated from the substrate and used for various commercial and industrial applications. Each metal production process will have variations in the actual electrowinning procedure. For this thesis, the focus will be on zinc electrowinning and is described in more detail next.

1.4 Zinc electrowinning

The industrial scale production of zinc metal is achieved predominately through the use of an aluminum cathode as the substrate, a lead-silver alloy as the anode and an acidic sulphate electrolyte which contains zinc ions and chemical additives [2]. The electrodes are placed in an alternating series in an electrowinning tank (cell – Figure 2) and the electrolyte with the appropriate concentrations of each component is then pumped through the cell

while a current density of ~ 450 A m^{-2} (i.e., 45 mA cm^{-2}) is maintained at the cathode [2]. From a review of various plant operations, zinc electrowinning is typically achieved with a temperature of the electrolyte in the range of 36 to 46°C and the sulfuric acid and zinc concentrations are in the range of 125 - 180 g L^{-1} or 50 - 80 g L^{-1}, respectively [2,4–6]. Typically, the electrowinning cells and the cell house are structured in such a way that it would maximize zinc production, while minimizing waste and energy consumption. The size of the anode is generally smaller than the cathode, where the cathode is 70 cm wide and 90 cm long [7]. The cathodes are placed with a spacing of 7.5 - 9 cm between them and the immersed area of the cathodes are typically 1.2 - 1.8 m^2. In some plants larger cathodes with areas as big as 2.6 m^2 are used and are labelled "jumbo cathodes" [7].

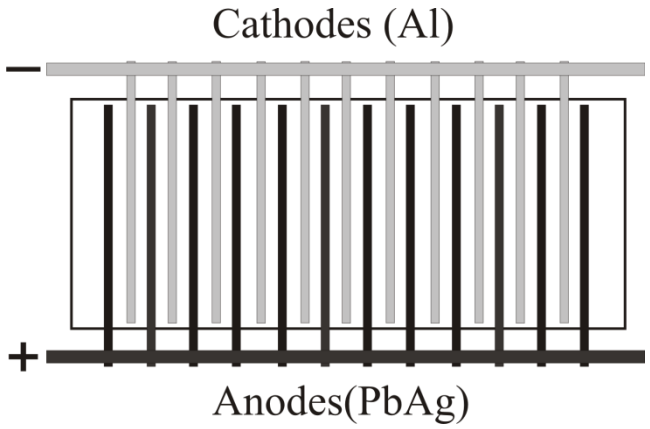

Figure 2: Top view depiction of an industrial electrowinning tank containing aluminium cathodes and lead-silver anodes.

Once the electrodes are in the cell, a current density ranging from 400 to 650 A m^{-2} is applied for up to 48 hours with a high current efficiency near 90% [2,4–7]. The current efficiency is obtained by calculating a theoretical mass of zinc that would result from the

current used and the deposition time. This is achieved through Equation 1.4 which can be substituted into Equation 1.3. The ratio of actual and theoretical masses recovered results in the current efficiency, denoted in Eq. 1.5:

$$Q = It \tag{1.4}$$

where:

- I is the current in amps (A)
- t is the time of deposition in seconds (s)

$$\%CE = \frac{m'}{m} \times 100 \tag{1.5}$$

where:

- m' is the actual mass recovered in grams (g)
- m is the theoretical mass recovered in grams (g)

In general, the current efficiency is less than 100% due to some additional electrochemical reactions that do not result in deposited zinc. There are three principal reactions that take place during zinc electrowinning. At the cathode, the reduction of zinc ions and protons occurs to produce the metal zinc (Eq. 1.6) and hydrogen gas (Eq. 1.7). At the anode, the decomposition of water takes place to produce protons and oxygen gas (Eq. 1.8).

Cathode:

$$Zn^{2+} + 2e^- \rightarrow Zn \qquad E^0 = -0.763\ V_{SHE} \tag{1.6}$$

$$2H^+ + 2e^- \rightarrow H_2 \qquad E^0 = 0.00\ V_{SHE} \tag{1.7}$$

Anode:

$$H_2O \rightarrow 2H^+ + 2e^- + \frac{1}{2}O_2 \qquad E^0 = +1.23\ V_{SHE} \tag{1.8}$$

Initially, during electrowinning, the primary reaction of zinc deposition (Eq. 1.6) occurs on the aluminum substrate, and eventually all of the substrate is covered with deposited zinc. After this point, electrodeposition continues on this layer of zinc through the process of crystal growth which may be influenced by various factors.

1.4.1 Influences on crystal growth in metal deposition

As described in the literature [8], crystal growth is the cooperative process of depositing particles to join to develop a new crystal. Overall, deposition is the sequence of events that each ion experiences from the instant it reaches the electric double layer until it becomes a part of the crystal. However, there are many factors that can influence electrodeposition and electrocrystallization which can be either direct or indirect [9]. A direct electrochemical influence may occur if electrode potential controls the nucleation and growth kinetics; in contrast, an indirect influence may be due to side electrochemical reactions caused by impurities in the electrolyte resulting in local alteration of pH and or hydrogen reactions stemming from impurity metal co-deposition. Therefore, as the system becomes more complex, a combination of such influences can affect the overall process.

As shown in Figure 3 and described in reference [8], the basic steps of electrodeposition and crystallization are as follows: 1) the reactants (zinc ion) approach the cathode by a combination of convection, migration and diffusion, 2) surface adsorption occurs via charge transfer, 3) surface diffusion of the adsorbed metal adatom occurs to kink or step sites on the surface resulting in a nucleation site, and, 4) growth of the nucleation site to a

crystal. It is important to state that all of these steps occur in the interfacial region of the electrode and many factors can influence one or all of these steps.

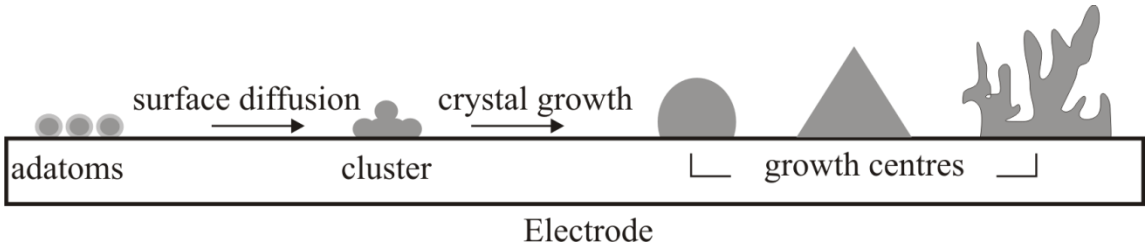

Figure 3: Schematic diagram demonstrating the key steps involved after solvated ions have become adatoms during electrocrystallization of a metal onto a substrate.

Figure 4 shows the interface where the red-ox reaction between electrolyte and electrode surface during electrodeposition. In this region there is a charge separation and results in potential distribution over the electrical double layer [10]. Also, in the interfacial region there may be a concentration gradient of species due to electrochemical reactions and chemical reactions causing formation, depletion and convection. Therefore, in theory, electrodeposition and crystallization processes can be influenced by factors such as: a) cell reactions (cathodic and anodic), b) chemical and electrochemical steps, c) solubility of reactants and products, d) charge of species, and e) solid phase changes (transformation, deposition and dissolution) [9].

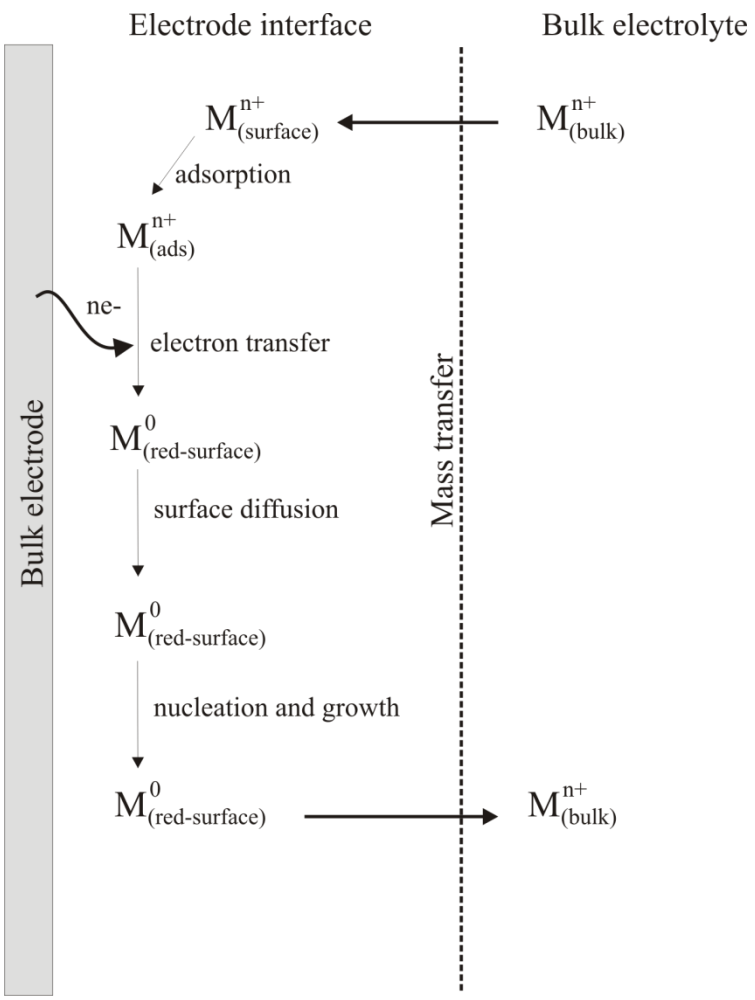

Figure 4: Simple schematic of the interfacial region between electrode and electrolyte demonstrating the fundamental steps that can influence, and cause changes in the crystallization.

In practice, as outlined in [9], further complications may arise due to such factors as: a) solid phase mixing (alloys, metal-oxide composites) b) chemical steps causing extreme pH changes, c) underpotential deposition leaving only a monolayer of adatoms, d) surface state and composition affecting adsorption or nucleation, e) morphology of the surface that gives rise to improved mass transfer due to increase surface area, and f) localized electrode potentials and current that change morphology, chemical and phase composition of

deposits. All of these effects can be time-dependent. As such, the process of electrodeposition is complex and the morphology of the zinc deposit can be affected by the above named factors.

These examples emphasize the need to purify the zinc sulfate solution prior to electrowinning because during the industrial production of zinc, it is desirable that the electrodeposits be pure, compact, level and easy to remove from the substrate [11]. It is also important to form these deposits under conditions that favour high current efficiency [12]. However, even though the zinc sulfate solutions are highly pure before electrowinning takes place, non-uniform zinc deposits and low current efficiency occasionally arise within the plant. The inclusion of chemical additives in the zinc electrolyte is often used to improve the final product quality. These additives have been classified as levelling agents, grain refiners, acid mist suppressing, and impurity complexing agents [4].

Leveling agents are used to reduce uneven or non-uniform growth of the metal deposit which would result in lower product quality and/or a plant interruption if a protruding part of the uneven zinc deposit makes contact with the anode resulting in a short-circuit causing damage to the cathode and/or anode. While leveling agents reduce occurrences of non-uniform electrodeposition of zinc, they do not completely eliminate them all together. The nature by which zinc deposits grow and the current efficiency of the system may be influenced by many parameters including, but not limited to: cathode (substrate) and anode material and morphology [13–21], concentrations of chemical additives [6,22–36], chemical and metal impurities [6,37–40], electrolyte pH [6,41], temperature and current density [6,42,43]. These parameters have been studied with electrochemical methods and in

the studies on growth morphology and crystalline structure, x-ray diffraction and high-resolution imaging such as Scanning Electron Microscopy (SEM) have been used. Even still, the problems associated with electrolyte impurities and additive concentrations remains an important aspect of the zinc electrowinning process. Some of these considerations are described in the next section.

1.5 Impurities

The minimal concentrations of impurities that continue to be present in the electrolyte, even after considerable purification steps are taken, result in negative outcomes with respect to current efficiency and product quality [2,44]. These impurities can be chemical and metallic. Metallic impurities are the most influential because zinc is less noble than the majority of metal impurities and hence low concentrations of other dissolved metals such as As, Bi, Cd, Co, Cu ,Ga, Ge, Fe, Mg, Mn, Ni, Pb, Sb, Se, Sn, Te and Tl have drastic effects on the current efficiency and morphology of the final product [2,12,33,37,39,40,44–48]. Chemical impurities may originate from the ore and these can be silica and halides [2,33,36,49]. Also organic chemical impurities might be introduced during the flotation process and also through machine lubricating oils [50]. However, some of these effects can be minimized by intentionally adding certain additives to the electrolyte mixture.

1.6 Chemical additives

During zinc electrowinning, chemical agents are included with the electrolyte not only to improve the deposition process by reducing impurities, but they are also used for acid mist suppression in the cell house [23,51], which is an unavoidable by product of the electrochemical process. Addition of strontium carbonate is used as way to remove lead

impurities in the electrolyte which are primarily caused by the dissolution of Pb from anodes [4]. Foaming agents are used to counteract acid misting that results from the bursting bubbles of oxygen and hydrogen gases formed on electrodes during deposition (Equations 1.8 and 1.9). These agents develop a thick foam layer at the surface of the cell which would impede the bursting process and result in lower levels of acid aerosol. Furthermore, additives are used to improve deposit morphology of the product. The ideal zinc deposit would be one that is level and compact and is easily removed from the aluminium substrate. To achieve such qualities, two main additives are used, namely, bone glue and sodium silicate [11,12]. Glue is thought to act as a levelling agent by interacting to areas of the deposit that grow and protrude resulting in higher local current densities, whereas sodium silicate is believed to interact with impurities in the electrolyte to reduce their influence.

Another additive used that influences current efficiency and morphology is licorice plant extract [28], however, it is primarily used as an acid mist suppressing foaming agent and not as a levelling agent [4,23,26,52].

1.6.1 Pearl glue (bone glue)

Bone glue is a subcategory of animal glue, which is produced from animal bones or hides. It is the hydrolysis of collagen protein molecules of the animal bones and hides that result in such glues. Collagens are a fibrous material composed of many polar and non-polar amino acids and the structure is made of triple helices primarily consisting of three amino acids (Figure 5): alanine, proline and glycine polymer chains [53,54]. Collagen itself cannot be used directly as an additive since the native collagen comes from animal tissues

and is not water soluble and has a large molecular weight (3×10^5 Da). Therefore, hydrolysis is required to alter this property. This is achieved by treatment of the animal tissues with heated water, acids, alkalines or enzymes which result in various fractions of molar weight species (200 - 250000 Da), including proteose, peptone and amino acid fractions. In the production of pearl glue, little attention is paid to separation and purification of each fraction and is usually a combination of proteose and other fractions [54]. Moreover the mechanism by which glue influences the deposit morphology is suggested to occur where the positively charged protein colloids interacts with negatively charged protruding active growth sites and ultimately increasing zinc crystallite nucleation resulting in a continuous fine grain development [54].

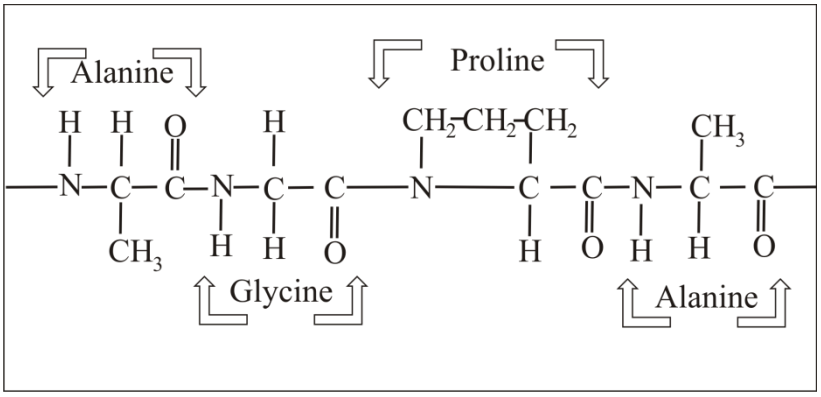

Figure 5: Schematic diagram of a portion of animal glues (bone glue) proteins.

In a study by Kerby *et al.* [54], the effects of pearl glue on current efficiency and morphology of zinc deposits were evaluated. Here they compared pearl glue with other standard glues individually. Using electrochemical and microscopy (SEM) methods, it was shown that pearl glue, which is the least hydrolyzed and has a molecular weight of 25 000

to 30 000 Da, had a higher leveling performance than other glues. Furthermore, the action of the glue was studied as a function of time that it was exposed to the acid electrolyte. This was done to understand the robustness of the additive after being exposed to the hydrolysing condition of the electrolyte acid at elevated temperature. The results of this test indicated that as the animal glue is exposed to a reduced pH and increased temperatures of the electrolyte, its ability to act as a good levelling agent is reduced with time. Therefore, while it is a good leveling agent, it must be continually supplied to the electrolyte feed in order to be effective at elevated temperature in an acidic medium. In the animal glue evaluation study by Kerby *et al*., it was also suggested that animal glue has the ability to reduce the negative effects of metallic impurities such as Sb. This is achieved by increasing overpotentials for metal deposition. It was noted that with increasing glue concentration in the electrolyte, an increased Sb concentration resulted in the final zinc deposit while an increase current efficiency was observed. This result suggested that the glue inhibits the resolution of zinc which may be normally caused by impurities. While it might seem counter-intuitive to have impurities included in the final deposit, these impurities in the industrial zinc electrolyte would be minimal (less than 1 mg L^{-1}) while maintaining a high current efficiency for zinc deposition. In order to further purify the zinc product, the very last stage of production includes a purification step which is achieved through pyrometallurgy.

1.6.2 Sodium silicate

Sodium silicate is an inorganic water-soluble compound. It is a common additive used in flotation for dispersing colloidal particles and slime as a result from grinding of the more

friable ore components [3]. It is produced by a reaction of sodium carbonate and silica as shown in equation 1.9 and typically occurs at temperatures ranging between 1200 to 400 °C [55].

$$Na_2CO_3 + SiO_2 \rightarrow Na_2O \cdot SiO_2 + CO_2 \qquad 1.9$$

Sodium silicate has been reported in multiple sources to be used in the process of zinc electrowinning as a beneficial additive for refinement of deposited zinc grains [4,7,47,56,57]. Information in regards to mechanism of action in zinc electrowinning is lacking in literature. Sodium silicate in aqueous solution may be acting as a depressing or dispersing agent on electrolyte impurities in the same fashion as it does during froth floatation.

1.6.3 Licorice

Licorice sapponin, *Glycyrrhizic* acid, is a natural product extracted from the roots of the plant *Glycyrrhiza spp* [26]. The chemical structure of *Glycyrrhizic* acid has been determined by high resolution ^{1}H and ^{13}C NMR and is presented in [58]. Licorice is a natural surface-active compound that provides stable foam in aqueous solutions, similar to surfactants. Saponins are regularly used in the zinc electrowinning cell house to limit the acid misting that occurs due to the gas bubbles that are produced, as previously discussed. Foaming behavior and acid mist suppressing ability of surfactants (including licorice) have been evaluated and can be found in [23,26].

1.7 Current understanding of zinc deposit morphology

There have been extensive studies to understand the role of impurities and additives on zinc electrowinning current efficiency, electrode polarization and morphology and these are typically achieved using cyclic voltammetery [59] and SEM. As a result of such studies a general schematic of zinc crystal growth (Figure 6) has been presented [60].

Influence of conditions on orientation of zinc crystal structure

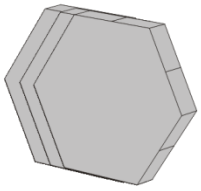

Hexagonal crystal structure

Overpontentials	Electrolytes containing	Platelet orientation & angle	Profile view of Zn crystal on substrate
Low	- Metallic impurities (Sb, As, Ge, Co, Ni, Cu)	Basal 0-30	
Medium	- Metallic impurities - Organic additives	Random 30-70	
High	- Organic additives (bone glue)	Vertical 70-90	

Figure 6: Schematic diagram of zinc deposit morphology types and platelet angle with respect to the cathode as a function of electrolyte and electrochemical conditions.

These structures were also observed in the studies conducted by Mackinnon *et al.* [39] when investigating electrolyte impurities and additives. The sample characterization was performed on zinc deposits electro-won from acid zinc electrolytes containing a range of metallic impurities with varying concentrations (Table 2) using SEM and x-ray diffraction to make observations of the impact on morphology.

Table 2: Metallic impurities with varying concentrations used in the study by Mackinnon *et al.* [39]

Impurity	Concentration in solution ($mg\ L^{-1}$)
Ga	50
As(III)	50
As(V)	10
In	50
Sn	10
Sn	20
Sn	50
Tl	50
Pb	3
Pb	9
Bi	30
Cu	5
Cu	50
Cd	5
Cd	50

It is reported in [39] that the morphology of zinc is affected by the elements in Table 2 which produced four distinct morphology types: 1) an intermediate-type having platelet

angles of 30-70° and well-defined hexagonal platelets of zinc from electrolytes that had no added impurities and additives and/or from electrolytes which contained Co, Ni, Cu, Ga, Ge, As(III), Cd. Type 2) is a triangular type deposit with platelets aligned to ~70° with respect to the substrate resulting from electrolytes with low glue concentrations (this corresponds well with Figure 7 which is an SEM image of a sample produced under low glue concentrations for this thesis) and low Tl, Pb. Type 3) has a vertical-type morphology with ~90° platelet resulting from high glue or electrolytes containing both glue and Pb and 4) shows a basal morphology type with low platelet angles (≤ 30) was associated with electrolytes containing Sb, Se, Te, As(V), Sn and Bi.

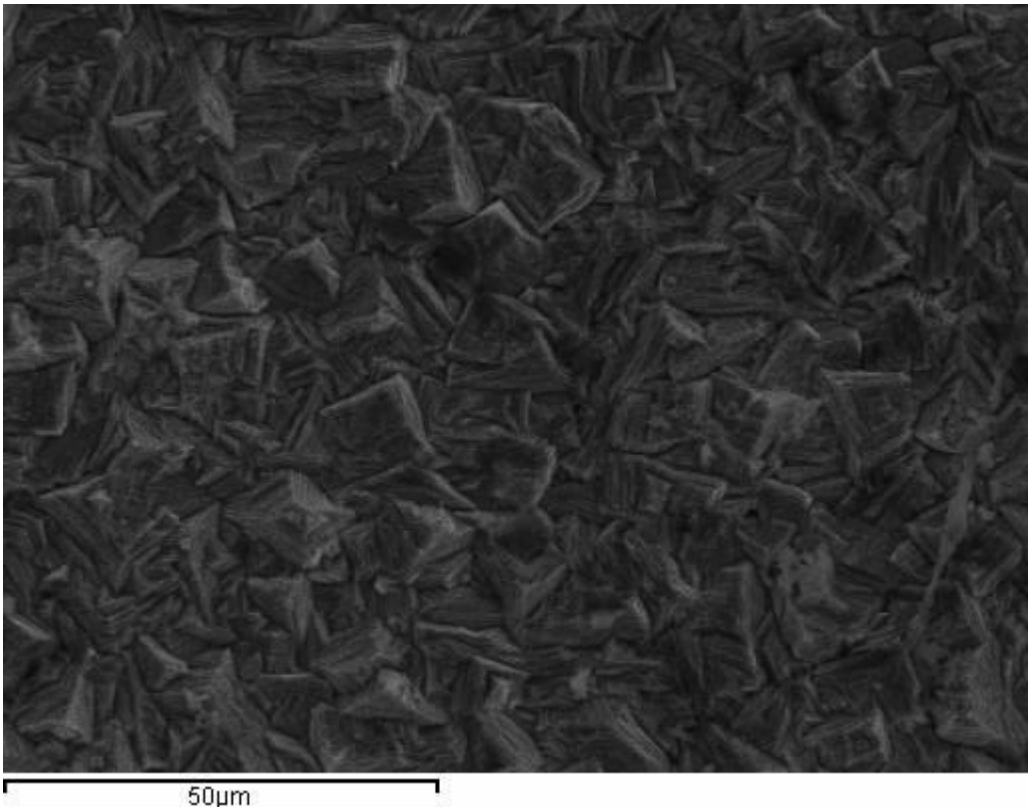

Figure 7: SEM image of zinc electrodeposit produced in this thesis showing triangular type morphology platelets. This sample was produced with a low glue concentration in the electrolyte.

As just described, there have been many studies that have employed electrochemical and microscopic methods to study different aspects of zinc electrodeposition yet the quantification of roughness properties as a function of additive levels is lacking in the literature. In this thesis, AFM and scaling analysis will be utilized to not only characterize but also quantify the roughness parameters of zinc deposits as a function of additive levels.

1.8 Characterization techniques

When investigating the influence of parameters such as substrate, impurity, additive, etc. on electrodeposits there are essentially two approaches that can be ventured, namely, electrochemical and surface observation [8].

There are numerous methods of electrochemical characterization that could be employed to study reactions occurring at or near the electrode surface. Reactions such as hydrogen evolution, zinc deposition and re-dissolution can be examined by cyclic voltammetry. Moreover, electrode (cathode and anode) polarization studies [61] can be conducted through potentiostatic and galvanostatic experiments. Also, current efficiency can be measured as a function of any parameter.

1.9 Objectives

In this thesis, the influence of chemical additives such as bone glue, sodium silicate and licorice on the morphology and current efficiency of zinc electrodeposition was examined with respect to deposition time and additive concentration. While some studies have been conducted on influence of glue on zinc morphology, they commonly have used SEM imaging for visual inspection of the surface. However, these studies have not quantified roughness characteristics of the deposit morphology. Therefore, in this thesis, the roughness characteristics of zinc deposits produced from a range of glue concentrations and deposition times has been further studied by 3D AFM analysis which allows one to quantify the variations in surface heights. In combination with scaling analysis (discussed further in Chapter 4) one can then obtain information on the deposition mechanism. Moreover, in contrast to glue, there is limited information pertaining to influence of sodium silicate and

licorice in the literature, especially from the perspective of quantifying the actual surface roughness. Again, this thesis contributes to this gap (Chapter 5) in the literature using AFM and scaling analysis. Also, in Chapter 6, ternary diagrams are utilized to provide information on the influence of relative concentrations of the three additives (glue, sodium silicate and licorice) on current efficiency and surface roughness characteristics.

Chapter 2: Theory

2.1 High-resolution imaging techniques

High-resolution imaging techniques are useful to get magnified images of a surface. Once a high-resolution image of the surface is taken it can be studied and characterized and sometimes the surface features can be quantified. There are many imaging techniques that would result in a high-resolution image or a topographical map of a surface. In this thesis, Scanning Electron Microscopy (SEM) and Atomic Force Microscopy (AFM) have been used and while both result in high-magnification images, conventional SEM does not provide 3-dimensional information without further modification of samples whereas AFM provides direct 3D information. SEM has the advantage of a larger field of view compared to AFM. However, in order to gain information on height variation on the sample surface using conventional SEM, it is required to cut samples and image the cross-section. Therefore AFM images are useful in characterizing the surface roughness characteristics quantitatively while SEM images are used for qualitative comparison and its advantages and disadvantages are discussed below.

2.2 Scanning electron microscopy (SEM)

A Scanning Electron Microscope is an instrument that uses an electron beam to interact with a conductive surface of solid samples. Examples of samples, instrument schematics and detailed information regarding instrument operating conditions may be found in [62]. Briefly, imaging is typically achieved under a vacuum of 1.33×10^{-5} - 10^{-6} mbar and the textural/morphological images of the surface result from the secondary electrons (SE) that are generated and captured by the detector. Besides textural morphology, SEM can provide qualitative information on other aspects of the sample such chemical composition and crystalline structure when coupled with Energy Dispersive X-ray Spectroscopy (EDS) and Electron Backscatter Diffraction (EBSD), respectively. These modes may be used to produce chemical composition and crystalline structural maps of the sample surface which can be coupled with the regular SEM image to show variations in chemical and crystalline composition with respect to surface morphology.

The electron beam is produced from a thermionic or field-emission electron gun and the electrons are accelerated by a voltage of 1-50 kV between the anode and cathode. The image resolution is dependent on the diameter size of the electron beam. The electron beam produced from a thermionic gun has a diameter in the order of 10-50 μm whereas a field-emission gun may provide a better resolution with electron beam diameter of 10-100 nm. These are further reduced in size by a two- or three-stage electron probe-forming lens system, which results in a1 nm to 1 μm diameter beam at the surface of the sample and having an electron probe current of 10^{-8} to 10^{-12} A depending on the mode of operation (i.e., EDS, EBSD, etc). In order to achieve the highest possible resolution, the electron-probe

current, aperture and size can be manipulated at once by adjusting the excitation of the first condenser lenses and aperture-limiting diaphragm in the last probe-forming lens. With the aid of a scan generator (deflection coil system) the electron probe is scanned in a raster across the sample and the detectors (SE, EDS and EBSD) receive the signal and the results are presented on an output display.

In conventional SEM, the sample holder can vary and depends on the size of the instrument's sample chamber. Also, the area of the sample being imaged is based on the desired magnification since higher magnifications result in a smaller area of the sample being imaged. At lower magnification, large areas or whole samples can be imaged but in order to get detailed information on the micrometer scale, high-magnification is required. Furthermore, the samples must be dry and solid with a conductive surface which would allow it to be placed in a vacuum and for electron-probe to interact with it to produce secondary electrons. Samples which do not have a conductive surface, but are dry, require a conductive coating typically achieved with a sputter coater to produce a film of either gold or carbon in order to have it be conductive for imaging in SEM.

2.3 Atomic force microscopy (AFM)

Atomic force microscopy is a technique, where the changes in the atomic forces between a probe and sample are measured. AFM was developed in 1986 by Binning and Quate and Gerber of IBM [63] and is categorized under the family of scanning probe microscopy (SPM) where an atomically sharp probe is scanned in a raster over a sample. The interactions and movements of the probe with the sample are then converted to a 3D image. As shown in Figure 8, the most common components of all AFMs are the piezoelectric

scanner, cantilever, laser, position-sensitive photodiode sensor, controller and computer [64–66].

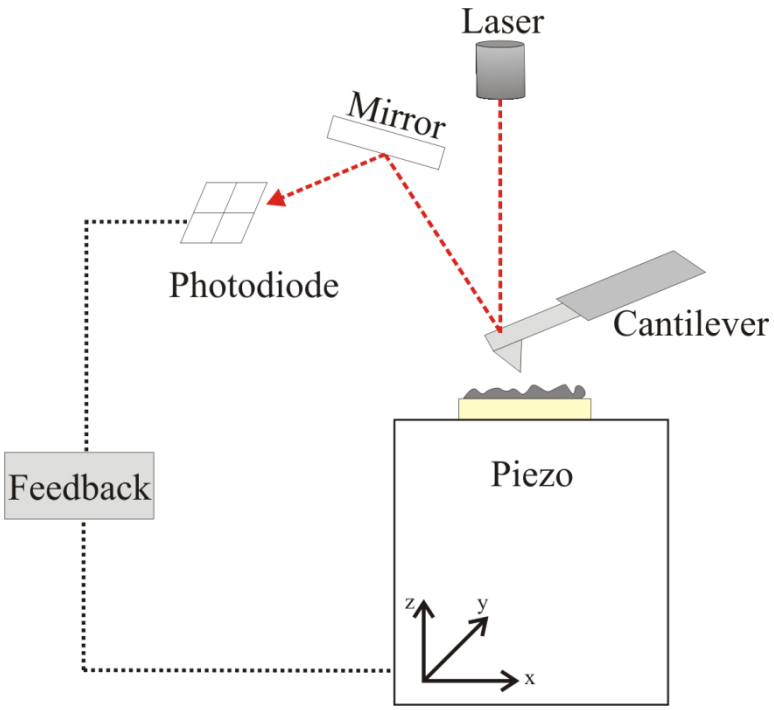

Figure 8: Schematic of the main working parts of an atomic force microscope (AFM).

Each of these main components has a specific purpose in the operation of the AFM. Starting with the cantilever, it has a reflective coating on the back and the underside has a sharp probe that ultimately interacts with the surface. The reflective side of the cantilever acts as a mirror to reflect a laser onto the photodiode sensor. As the cantilever is scanned across the surface, it will deflect as the tip encounters surface features. These vertical displacements cause changes in the laser position on the photodiode which are converted to height of surface features. The controller manages the precise voltages that are applied to the piezo-scanner and determine the extent to which the piezoelectric scanner expands or

contracts. These changes allow the sample to move. For this type of AFM, it is in fact the sample that is rasterred under a stationary probe, but the surface recording principles are the same. The motion of the piezoelectric device can be relatively small and very precise, thus enabling the AFM to collect high- resolution data. Therefore, the features of the scanner determine the sampling area size in the AFM. Lastly, images are displayed and analyzed on a computer with the appropriate software [64–66].

Measurements over the scanned area are not restricted to height variations alone and can reveal different properties of the surface such as friction or electronic information [64–67]. The user may characterize any of these properties using the appropriate operating modes of the AFM. There are three modes which may be utilized; contact, tapping and non-contact modes [65]. Briefly, contact mode is where the probe is in direct contact with the surface and experiences repulsive forces from the surface features (Figure 9). This mode would be used on solid and hard samples which are relatively smooth and not likely to be damaged or modified with the hard and sharp probe contacting it [64]. Tapping mode occurs when the probe is set to oscillate within a desired amplitude and frequency and it comes into intermediate contact with the surface making it more suited for softer solids that may be distorted by the tip in contact mode. Non-contact mode imaging is where the oscillating probe with small amplitude is scanned near the surface without ever making contact to detect attractive forces (Figure 9), a technique that is useful for very soft surfaces. Contact and tapping mode can be employed in air or liquid. In contrast, non-contact mode is only applicable in a vacuum [66] and is the least frequently used imaging mode in AFM. Furthermore, the type of cantilever used in each mode and or medium (air, liquid, vacuum)

differ in their spring constant in order to counteract different types of forces involved in each medium.

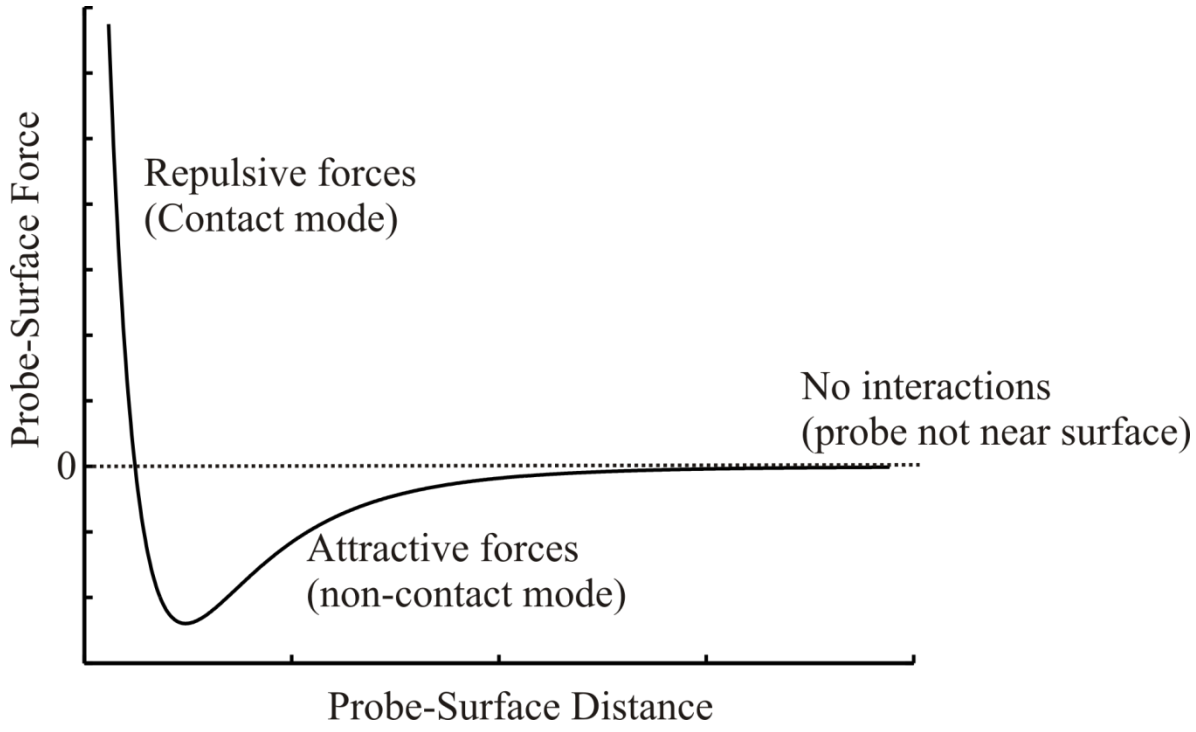

Figure 9: Schematic of a force curve demonstrating types of forces experienced by the AFM probe as a function of distance to the surface of the sample

In this thesis, AFM-tapping mode imaging in air was used on zinc electrodeposits to collect 3D surface images. Tapping mode has the advantage of collecting 3D images with excellent resolution without damaging the soft zinc surfaces. While stylus profilometery does allow for data to be collected in the x-, y- and z-axis, it lacks the resolution in the nanometer scale due to the tip size of the stylus. Furthermore, the stylus might damage samples that are softer than the stylus tip that comes in contact with the sample surface when collecting data.

Optical profilometery, although not utilized for this thesis, would allow for larger 3D images with nanometer scale resolution to be captured in a relatively short time.

In Figure 10, an image of the AFM calibration grid collected with tapping mode is shown. The calibration grid is manufactured out of silicon with features of known dimensions in x, y and z. The grid imaged in Figure 10 was manufactured with square features (troughs or recesses) that are nominally 180 nm in depth (z-axis), 5 μm in width (y-axis) and 5 μm in length (x-axis). These features are also separated by 5 μm from each other. These characteristics are clearly visualized in Figure 10 and are consistent with the manufactures specifications. The grid is utilized to calibrate and maintain reliable data collection and also demonstrates the high resolution of the AFM used in this thesis.

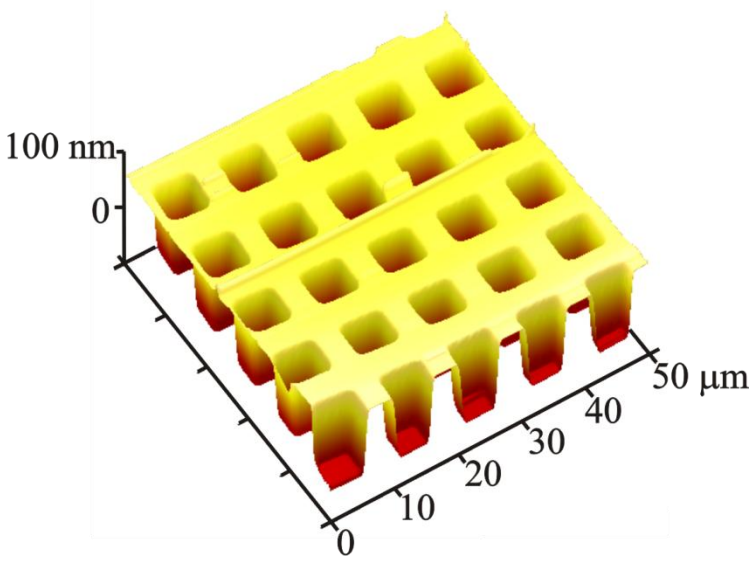

Figure 10: 3D image of the AFM Calibration Grid captured in tapping mode. Imaged using J-scanner from Bruker Instruments. The image shows that features are separated by 5 μm and are also 5 μm in width and length which match the manufacturer's specifications for this calibration sample. The depth of each feature is shown to be in the nanometer scale. Note, the aspect ratio of x and y are 1:1 but not in z.

While the image resolution is excellent, the size of the sampling area being characterized is limited in all x, y and z directions to the ability of the piezoelectric material that governs the movements of the sample stage and cantilever oscillations [64–67]. The piezoelectric material used in different models of AFM can vary in their scanning range. Therefore, depending on the size of the image and measurements being sought, the appropriate piezo-scanner and cantilever are needed. Figure 10, was captured using a J-scanner from Bruker instruments which is limited to 125 μm in both x- and y-axis and 6 μm in z-axis. These are the maximum sizes available to the AFM; for this thesis, the deposition time of zinc and the image sizes were restricted by these operating parameters. For example, the deposition time was limited to a maximum of 90 minutes because the heights of zinc features made from certain electrolyte conditions are outside of the J-scanners height limit when deposition times exceeded this value.

With the 3D information inherent in AFM, it offers a means to quantify surface roughness. Typically this is done with the average roughness, that is measured from the root-mean-square deviation (*rmsd*) in surface heights across the whole image. From now on, this roughness parameter will be referred to as the "*rms* roughness". However, *rms* roughness is not the only parameter of interest when quantifying surface features. One might be interested in the relative surface height of one feature to another or the variation in height to width ratios. These and other surface feature measurements can be obtained with scaling analysis.

2.4 Scaling analysis

In recent decades, there have been advancements in the science of surface growth processes stemming from developments made in fractal concepts, random deposition (stochastic growth), linear theory (stochastic growth with surface relaxation) and scaling. There are models for different types of growths (e.g., deposition with non-linear relaxation), some of which are Edwards-Wilkinson (EW), Kardar-Parisi-Zhang (KPZ), and Wolf-Villain (WV) [68,69]. Discrete and continuous models for all of them have been developed and these mathematical models have also been compared with experimental data of various surface growth mechanisms which have been made possible due to the ability to collect high-resolution data of rough surfaces. These developments now allow for quantifying and in some cases predicting rough surfaces. These models have been discussed and explained with extensive detail in [69], but will not be discussed individually here. Rather, a general description of scaling analysis is provided.

When studying rough surfaces, an obvious quantifiable parameter is the variance in the heights of a surface. This is a measure of the surface roughness and could be obtained by extracting either the root-mean square (*rms*) of the surface height or the standard deviation of heights. However, *rms* only describes changes in the vertical height, while the corrugation of the surface features, or the changes in the horizontal distribution of features may also be important. As such, the height-to-width ratio of three-dimensional surface features become important when quantifying surface roughness parameters [68]. In order to gain insight on surface variance, height and corrugation, autocovariance function (ACF) and spectral power density (SPD) could be applied. These approaches alone are limited to

providing numerical values that describe the variance in surface height and its correlation length and its frequency. Therefore, no insight is gained into the mechanism by which a surface has grown [68]. However, the method of scaling analysis, which can be related to ACF and SPD, additionally provides mechanistic information and roughness characteristics [68]. This is an important factor when the aim of an experimentalist is to determine how and what is influencing the growth of the surface. In order to get roughness characteristic and mechanistic information, scaling analysis has been employed in this thesis on 3D surface images of zinc electrodeposits that were captured with AFM in a similar manner to the copper electrodeposits produced in the study by Zhao *et al.* [70].

In scaling analysis, the *rms* roughness (ξ) of the surface is calculated at different scale lengths (L) through:

$$\xi(L,t) = \sqrt{< [H_L(r,t) - < H_L(r,t) >]^2 >} \qquad 2.0$$

where:

H is the height (nm)
r is a given point or range of pixels on the image (μm)
t is the deposition time (s)

Although this equation is applied to 3D images in this thesis (described further in the experimental chapter), it is convenient to explain it using a hypothetical 2D data set. Consider a line with variations in heights with a given length as shown in Figure 11a.

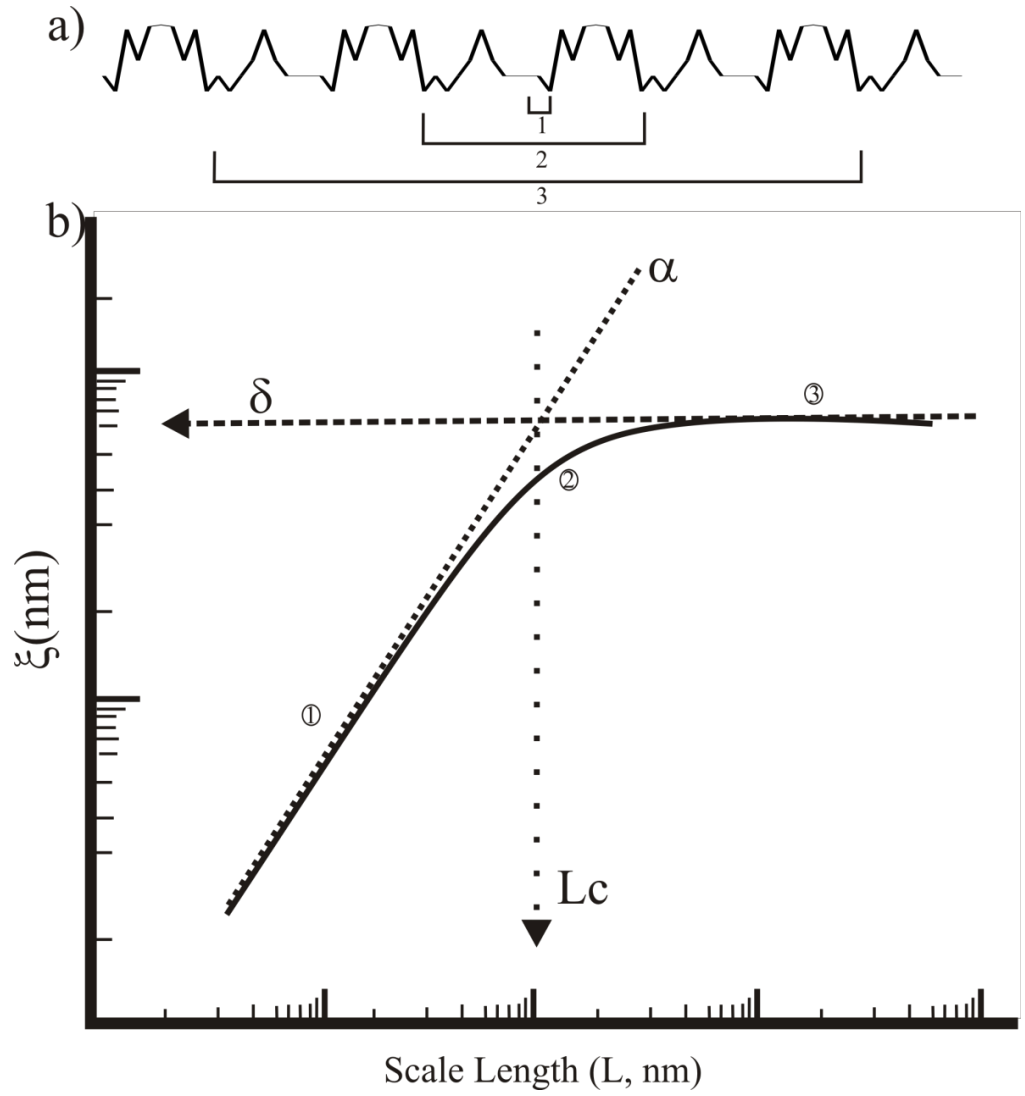

Figure 11: a) Line representing a surface with periodic variations in heights and b) Schematic scaling analysis plot showing a linear increase in roughness (ξ) with scale length (L) and where the static exponent (α) is extracted. Following the linear region reaching a critical length where the roughness saturates. The plateau is extrapolated to obtain the overall roughness value (δ). The critical length (L_c) represents surface feature widths or surface periodicity and is extracted at the intersection of α and δ.

The *rms* roughness, similar to the standard deviation of heights, is calculated over all possible scale lengths on the line. These are indicated in Figure 11a by a short length scale segment 1, and two longer length scales in segments 2 and 3. As shown in the figure, the

standard deviation of height or *rms* roughness in segment 1 should be relatively small. In comparison, length scales between segment 1 and segment 2 would have increasingly larger standard deviation of height or *rms* roughness values. Segment 2 is a unique scale that marks the length for a repeating pattern in this hypothetical periodic plot. The length in segment 2 then indicates the critical length at which the *rms* roughness has reached a maximum. Any length scales greater than segment 2, such as that shown in segment 3, will have the same *rms* roughness or standard deviation. In scaling analysis, the *rms* roughness is given by the symbol $\xi(L,t)$ which is a function of all possible scale lengths over the line and is also a function of the deposition time (t). Once all of the roughness values at a particular time have been computed, a log-log plot of ξ vs L (nm) is generated and is schematically represented in Figure 11b. This plot has a characteristic trend where roughness increases linearly for scale lengths between segments 1 and 2, until the critical length (L_c) is reached after which point the roughness saturates. This plateau is the overall roughness, or limiting roughness and is given the symbol δ.

As scaling theory states [68,70], there is a power law relation between ξ and the time-independent static roughness exponent α, (Equation 2.1) at scales smaller than the critical length.

$$\xi \propto L^{\alpha} \quad for\, L \ll L_c \qquad 2.1$$

where:
ξ is *rms* roughness (nm)
L is scaling length (nm)
α is the static growth exponent
L_c is the critical scaling length (nm)

Another power law relation exists between δ and the dynamic or temporal roughness exponent, β. This exponent describes the time-dependence of growth through Equation 2.2 [68,70].

$$\delta \propto t^{\beta} \quad for\ L \gg L_c \tag{2.2}$$

where:
t is time (s)
β is dynamic growth exponent

The third power law that exists is a relation between L_c and the ratio of temporal to static exponents with a time-dependence (Equation 2.3) [68,70].

$$L_c \propto t^{\left(\frac{\beta}{\alpha}\right)} \tag{2.3}$$

The fourth power law relation which is time-dependent exists between the δ to L_c ratio and what is said to be an optical roughness exponent, γ (Equation 2.4) [68,70].

$$\frac{\delta}{L_c} \propto t^{\gamma} \tag{2.4}$$

where :
γ is the optical roughness exponent

As such, there are three relations that are time-dependent and one that is not. Scaling relations and their exponents are useful for gaining insight on growth mechanism and open the possibility to predicting limiting roughness and critical lengths of a long-term growth system from a series of short-time experiments. Therefore, it is important to understand

what each roughness parameter and exponent represent as well as how to apply them when studying the surface roughness of electrodeposits.

2.4.1 Limiting roughness (δ)

The overall roughness of the sampled area is called the limiting roughness (δ). This value is extracted from the saturated regime of the scaling plot (Figure 11b). It is time-dependent since electrodeposits will grow in surface roughness with deposition time as more material is being deposited. While this parameter is important it can be misleading if judgements regarding a surface are made only considering this parameter at a single deposition time. It can be misleading because surfaces created under different deposition conditions may result in a similar limiting roughness value but the feature widths may differ. As such this value should be considered with other roughness parameters such the corrugation and aspect ratios of the surface features (see below).

2.4.2 Critical length (L_c)

The length at which the surface becomes saturated in roughness is called the critical or corrugation length (L_c) (See Figure 11b). This parameter represents the width of surface features or the periodicity of the surface, i.e., how often a feature repeats with respect to a lateral length of the surface. Critical length on its own can give a good idea of how the lengths of surface features are affected by the deposition conditions [70].

2.4.3 Ratio of limiting roughness to critical length (δ/L_c)

The ratio of the limiting roughness to the feature widths (δ/L_c) is related to the aspect ratio of surface features and provides a better understanding of how one dimension grows with

respect to the other. For instance, surface features might grow more rapidly in one dimension compared to the other under different deposition conditions. Therefore, making judgment of surface roughness is best achieved through comparison of the roughness to width ratio of surface features. If related to the aspect ratio of surface features, a large value can be considered as the roughest because they would arise from large limiting roughness over narrow features thereby giving a needle-like appearance for a given feature. If features have low aspect ratios, it would mean that the features are much wider than they are high, resulting in a less rough surface. For a given *rms* roughness, the one with the larger δ/L_c ratio is considered the rougher sample [68].

2.4.4 Static exponent (α)

The static exponent is extracted from the slope of the linear regime of the scaling plot (Figure 11b). The static exponent α serves two purposes. First, it is used as an indicator of relative uniformity over a measured surface, where a value of α is between 0 to 1 for fractal like surfaces [69]. A growing surface that has an α value of 1 is said to be self-similar at any time; meaning that the critical length and limiting roughness have the same time dependence [68]. Furthermore, if the value is less than 1 then it is said that the surface is self-affine. Therefore, the first purpose of α is to make a statement on how relatively uniform the growing surface is at all scalable lengths.

The second use of α is to provide insight on the surface growth mechanism through equation 2.5 and an appropriate scaling model (e.g. KPZ as introduced in section 2.4).

$$n = 2(a + 1) \qquad 2.5$$

The relationship between coefficient *n* and the static scaling exponent α (explained in detail in [68]) is developed and gives insight on the dominating growth mechanism. As described in [68], when *n* = 1, the smoothing of the surface is due to viscous flow of an amorphous material; for *n* = 2 smoothing is from dissolution and re-deposition; *n* = 3 indicates bulk diffusion or the progressive nucleation; and *n* = 4 suggests that surface diffusion is the mechanism of the growing surface [68,70].

2.4.5 Dynamic or temporal exponent (β)

The temporal exponent β characterizes the rate of change in limiting roughness and is extracted from the slope of a log-log plot of δ versus deposition time. This is used in Equation 2.2, which has been used to predict the limiting roughness of a sample at longer deposition times provided that the deposition mechanism remains unchanged [68,70]. Furthermore, the ratio of β/α characterizes the rate of change in critical length; when used in Equation 2.3 it can predict the critical length of a surface at a given time [68,70]. In summary, surface limiting roughness and critical length can be extracted if a series of timed deposition studies are performed.

2.4.6 Optical roughness exponent (γ)

Similar to β, the optical roughness exponent γ can be extracted from the slope of a δ/L_c versus deposition time plot on a log-log graph. When this value is used in Equation 2.4, the height to width growth rate can be predicted at a given time [68,70]. It is important to state

that this can only be achieved if a series of timed experiments have been done for a given system.

2.5 Scaling program and image treatment

In this thesis, scaling analysis was performed on the AFM image data by employing a MATLAB algorithm that was programmed in-house by Dr. Shepherd. The scaling algorithm was initially written to apply Equation 2.0 to calculate the average *rms* value within all possible pixel arrays of the image, starting with all possible 2 × 2 arrays until reaching the maximum of a 512 × 512 pixel array. For example, the *rms* value was calculated for all possible 2 × 2 pixel arrays (which has a known length (L)), and these values were averaged to obtain ξ at the given scaling length. This process is then repeated with increasing pixel array size by 1 (i.e., 3 × 3, 4 × 4 etc) until the maximum 512 × 512 pixel array is achieved. The ξ versus scaling length (L) was then plotted on a log-log plot and the scaling exponents extracted. This is called the full scaling program. This program however is heavy on computation time since more than 44 million calculations are required for a 512 × 512 pixel image.

A truncated scaling program was written in an attempt to reduce computation time while maintaining accurate scaling plots. In the truncated version of the program, the n × n pixel array increases by 1 for the first 10 computations of ξ. In this regard, ξ is calculated for all possible 2 × 2 pixel arrays and then averaged. The next iteration continues for all possible 3×3, 4×4, ⋯ , 11×11 pixel arrays. This gives at least 10 consecutive data points at the low scaling length regime. The next 10 computations of ξ were performed over pixel arrays that

skip by 2, or all possible 13×13, 15×15, ⋯ , 31×31 pixel arrays. This process continues over the next 10 computations skipping by 4, then 8 for the next 10 computations and so on. This is done so as to not lose data at the smaller scaling lengths, albeit some data is lost at the larger scaling lengths where the log-log plot of ξ versus L saturates. The skipping of points in this truncated scaling program reduces computation to less than 9.5 million calculations thereby reducing the program time substantially.

To show the impact this has on the scaling output, these two programs were applied to an AFM image of the calibration grid (Figure 12a) and the results are shown in Figure 12b, c and d.

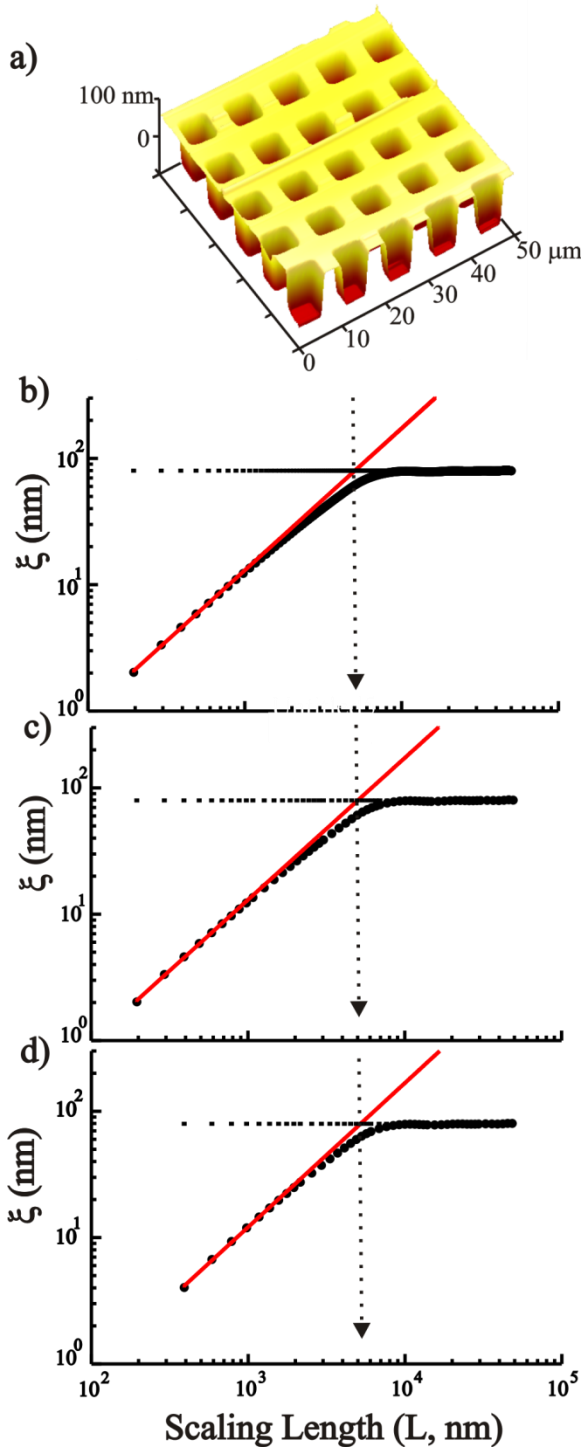

Figure 12: a) 3D AFM image of calibration grid, b) scaling plot produced from full scaling program, c) scaling plot resulting from truncated scaling program, d) scaling plot resulting from binning to 256 by 256 pixel and truncated scaling program

In this case the AFM image of the calibration grid is 50 × 50 μm with 512 × 512 pixels in total. The scaling plot that results from the full scaling program is shown in Figure 12b and that of the truncated scaling program is shown in Figure 12c. By comparing these two plots, it is clear that the first 10 data points are identical between each method but as the scaling length increases, it is evident that, even though there are fewer points on Figure 12c compared to Figure 12b, this produces little change in the limiting roughness (δ), between the two methods. However, the critical length (L_c) extracted from the truncated program is slightly lower than that extracted from the full program, which would result in a slightly different δ/L_c ratio. The actual values are compared in Table 3 showing that the difference is not substantial. Furthermore, since the first 10 points on the graph are identical between the two programs, they result in the same slope in the linear region where α is extracted. It is instructive to note that the results of scaling analysis performed on the AFM calibration grid from both scaling programs are close to what is expected when comparing to the manufactures' specifications of the grid. The most obvious parameter of the scaling result is the critical length (L_c) as this represents the periodicity or width of the features on the imaged surface. This value is about 5000 nm (or 5 μm) from both scaling programs. Next, it is known that the grid wells have a nominal depth of 180 nm or a variation of plus/minus 90 nm centered about a zero mean. This results in an *rms* variation of close to 90 nm. The limiting roughness (δ) values extracted with the full and truncated scaling programs are 79.9 and 79.7 nm, respectively, which are again close to the manufacturers specifications for the grid. Also, the δ/L_c ratio on the grid is expected to be 90 nm/5000 nm which is close to 0.018 and the δ/L_c extracted from the full and truncated scaling program is 0.0159, which

again compares reasonably well. Lastly, the static growth exponent (α) output from both scaling programs is 1 and this value makes sense because the calibration grid is manufactured to be very uniform and self-similar.

Table 3: Comparison of the scaling parameters and computation time output from an AFM calibration grid using the full and truncated scaling

Image size (μm)	Resolution, Scaling Program	Program run time (min.)*	δ (nm)	Lc (nm)	δ/Lc	α
50×50	512x512 pixels, Full	170	79.9	5035	0.0159	1
50×50	512x512 pixels, Truncated	15	79.7	5020	0.0159	1
50×50	512x512 binned to 256x256, Truncated	2	79.5	5199	0.0153	1

*** PC laptop with an Intel i7 processor @ 2.30 GHz and Windows 7 was used to run these programs**

Moreover, in this thesis the AFM images were either 100 × 100 μm or 50 × 50 μm depending on experimental limitations. Every image was always captured with a total of 512 × 512 pixels. In order to make relative comparisons between these images, the resolution (i.e., μm/pixel) should be the same between each sample. To achieve this, all images that were originally 100 × 100 μm were manually cropped to 50 × 50 μm and since cropping does not change the resolution, these images were 100 μm/ 512pixels or 50 μm/256 pixels giving an image resolution of 0.195 μm/pixel. All of the raw images collected originally at 50 × 50 μm and 512 × 512 pixels were binned in sets of two, thereby rendering images with 256 × 256 pixels and a resolution of 0.195μm/pixel. Because of this, a third scaling program was written to include the binning of the image at the start of the truncated program. This results in the computation time being reduced further to two

minutes per image analyzed (Table 3) using the PC described in Table 3. Figure 12d, shows the scaling plot that results from the same 50 × 50 μm image that was used to produce the scaling plots in Figure 12b and c. However, the image was treated with the new scaling program and therefore was binned by two at the start of the program. Again, note that the scaling plot in Figure 12d is very similar to those in 12b and 12c albeit there are fewer points on the plot, and the L_c is now a value of 5199 nm compared to 5020 nm without binning. The results of scaling parameters are shown in Table 3. While most parameters compare well in Table 3, there is a slight increase in the critical length as a result of the binning procedure and this is manifested as a decrease in the δ/L_c ratio by 3.8%.

For simplicity, in this thesis, all data presented was analyzed so that all image sizes were 50 × 50 μm with 256 × 256 pixels and each of these were treated with the truncated scaling program.

2.6 Scaling profiles containing two linear regions

Among other examples in the literature, scaling analysis performed on Ni-Zn binary electrodeposits have shown the occurrence of two linear regions in the scaling plot [71]. These regions are schematically visualized in Figure 13b. This phenomena has been studied and reported as an effect of grain size and shape [72,73]. Therefore, when a surface has more than one growth mechanism which results in more than one type of grain shape and/or size, it manifests as two linear and crossover regions on a log-log plot of ξ versus scaling length (L). For instance, the first linear region (α) would represent the static exponent (uniformity and mechanism) of the growth occurring at the smaller scales

whereas the second static exponent (α') represents the morphology at a slightly larger scale length. This is useful because growth information of two types can be characterized and therefore makes scaling analysis a very good approach to investigating surface growths of electrodeposits under changing conditions.

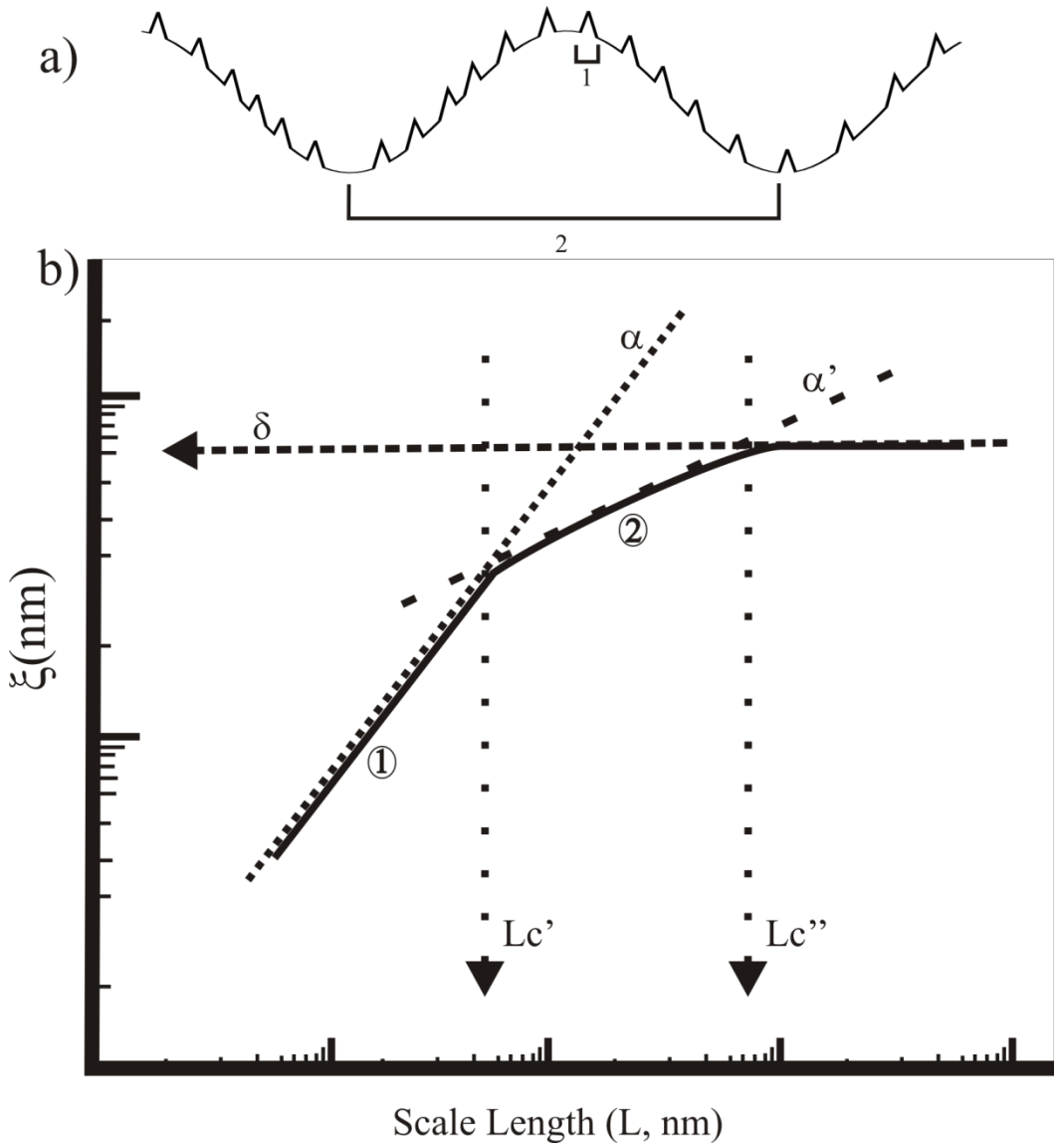

Figure 13 : Schematic representation of a surface cross-section (a) and its scaling profile (b) with two linear regions representing two distinct growth mechanisms. The result is two feature sizes: α and L_c' are for growth mechanism and features occurring at the smaller scale length (L), whereas and α' and L_c'' are for features caused by growth mechanism occurring at the larger scale length (L). Overall limiting roughness is still extracted from the plateau.

Electrochemistry and SEM have been utilized in the past to characterize the influence of industrial deposition conditions on zinc deposits. However, AFM combined with scaling

analysis has been underused. Therefore, in this thesis, AFM combined with scaling analysis was applied to gain insight on the influence of additives (glue, sodium silicate and licorice) on zinc growth and morphology by producing short-time electrodeposit samples from an industrially relevant electrolyte.

Chapter 3: Experimental

3.1 Electrolyte

The electrolyte was always prepared in analytical glassware. Before preparation of the electrolyte solutions, the glassware was first cleaned in a 50:50 (v:v) acid bath mixture of concentrated sulfuric acid and nitric acid. Next, the glassware was thoroughly rinsed with ultrapure water.

There are two types of species in the electrolyte: supporting and electroactive. The supporting electrolyte is sulfuric acid and the electroactive electrolyte is Zn^{2+}. The supporting electrolyte is needed to increase the ionic conductivity and to achieve an acidic pH. Also the electrolyte contains additives (glue, licorice and sodium silicate) that may be surface active.

Electrolyte solutions were always prepared using a purified neutral zinc stock solution containing 168 g L^{-1} zinc sulfate provided by Teck. The zinc concentration in the electrolytes were adjusted using H_2SO_4 (Sigma-Aldrich, 98%) and ultrapure water (Mili-Q, synergy UV, 18.2 MΩ cm) to obtain a concentration of 160 g L^{-1} H_2SO_4 and 60 g L^{-1} $ZnSO_4$. This is referred to as the standard electrolyte and was modified with additives to

study their influence on zinc electrodeposit morphology and current efficiency. Therefore, depending on the composition of additives being studied (Table 4), the amount of each additive was adjusted appropriately. The additives studied in this thesis are glue (supplied by Teck), Licorice (Teck), and sodium silicate (Sigma-Aldrich). The concentrations used in each experiment are listed in Table 4 with their amount in mg L^{-1} indicated by the number preceding the first letter of their name. For example, 2.5G, 3.5SS, 4L would represent an electrolyte that has 2.5, 3.5, and 4 mg L^{-1} of glue, sodium silicate and licorice, respectively, along with the 160 g L^{-1} H_2SO_4 and 60 g L^{-1} Zn previously stated. The electrolytes were always made immediately before electrodeposition to reduce the possibility of degradation of additives such as glue. As aforementioned in the introduction, acid could hydrolyze the proteins of the glue. Therefore, it was important to always use fresh electrolyte to minimize any negative influence that could result from additive degradation. Furthermore, deposition times were randomized and were not in succession to avoid systematic errors.

Table 4: Concentration of additives studied with deposition times and image size studied per study

Study#	Studies shown in Chapter	Additive amounts (mgL^{-1})	Deposition times (minutes)	Number of images/ deposition time	Original image size (μm)
1	4	30G_2.7SS_9L	10, 30, 50, 70, 90^{+}	9	100×100
2		3G_2.7SS_9L	30	9	100×100
3		7.5G_2.7SS_9L	30	9	100×100
4		15G_2.7SS_9L	30	9	100×100
5		22.5G_2.7SS_9L	30	9	100×100
6		37.5G_2.7SS_9L	30	9	100×100
7		60G_2.7SS_9L	30	9	100×100
8	5	30G_0SS_9L	10, 30, 50, 70	3	100×100
9		30G_1.35SS_9L	10, 30, 50, 70	3	100×100
10		30G_5.4SS_9L	10, 30, 50, 70	3	100×100
11		30G_13.5SS_9L	10, 30, 50, 70	3	100×100
12		30G_27SS_9L	10, 30, 50, 70	3	100×100
13		1G_2SS_5L	10*,20,30,50	9	50×50
14		1G_4SS_5L	10*,20,30,50	9	50×50
15		1G_15SS_5L	20,30,50	9	50×50
16		1G_2SS_0L	10,20,30	9	50×50
17		1G_2SS_15L	10,20,30	9	50×50
18	6	2.5G_3.5SS_4L	10, 20, 30	3	100×100
19		6G_50SS_9L	10, 30, 50^{+}, 70^{+}	3	100×100
20		15G_38SS_9L	10, 30, 50,70^{+}	3	100×100
21		22.5G_25SS_9L	10, 30, 50,70^{+}	3	100×100
22		6G_5.4SS_9L	10, 30, 50	3	100×100
23		15G_13.5SS_9L	10, 30, 50	3	100×100

* 10 minute deposits resulting in an incomplete zinc layer
$^{+}$ Deposits that were not able to be imaged due to AFM's operating limit

3.2 Mini electrowinning cell

The mini electrowinning cell used for electrodeposition of zinc was created in-house. The electrochemical cell is made up of two electrodes and the container is a glass beaker. The electrodes were a platinum anode (Alfa Aesar, 1 mm diameter, 99.99%) and aluminium

cathode (provided by Teck). While the industrial practice of electrowinning employs lead-silver anodes, platinum was used in this study to avoid any lead contamination similar to [54]. The anode was formed by shaping a 5 cm length of platinum wire into a loop to achieve a geometric area of 1.6 cm^2. This area was chosen in order to obtain a cathode/anode area ratio similar to what is possible in the AFM electrochemical cell. There were no *in-situ* AFM electrochemical studies done for this thesis. However, the cathode/anode ratio was maintained for potential comparison with future *in-situ* studies. The area of the anode and cathode are 1.6 cm^2 and 1 cm^2, respectively, which results in similar geometry to the mini-cell design of 1:1 used at Teck. The cathode for the mini-electrochemical cell was prepared by cutting the aluminum cathode (provided by Teck) into a square with an area of 1 cm^2. Next, a steel wire was pressed against the back of the square to make electrical contact. Then, both aluminum cut square with the wire attached to its back were fully encased in an epoxy (Leco-Resin epoxy and hardener) and left to cure at room temperature for 24 hours. This was followed by exposing only the front face of the aluminum by sanding the epoxy away with 180, 280, 400, and then 600 grit sandpaper. The exposed face of the cathode was further polished to a mirror finish with 6, 3, and then 1 μm of water-based diamond suspensions (Buehler). After polishing the cathode surface was thoroughly rinsed in ultrapure water to avoid any contamination in the cell. The additional polishing to a mirror finish was performed in order to obtain a uniform substrate area. Between each deposition, the cathode's surface was polished to have a 1 μm mirror finish so that there would be no influence of initial substrate morphology on the zinc deposits. Both electrode contacts were fed through glass rods and the glass rods were mounted in a

rubber stopper to achieve a distance of 0.5 cm between the two electrodes. This distance was maintained for every experiment. It should be noted that the anode (platinum) was also used as a quasi-reference electrode since the studies conducted were galvanostatic, where control of potential is not required.

3.3 Electrochemical procedure

Electrodeposition of zinc was conducted using the mini-electrowinning cell. The mini-cell was always filled with 20 mL of fresh electrolyte and the electrodes were placed into the cell simultaneously. Immediately after, a potentiostat (Pine model AFRDE5 Bi-Potentiostat) was used in galvanostatic mode and the current was maintained at a current density of -44mA cm^{-2} for a set period of time (see Table 4). This galvanostat was controlled using in-house written programs in LabVIEW. After the deposit was prepared, the current is set to nil. The electrodes were immediately removed from the cell and rinsed in ultrapure water to protect the zinc deposit from dissolving back into the acidic electrolyte. The range of deposition times were always above the minimum time required to achieve a complete layer of deposit on the substrate that was easily peeled off. This lower limit of the time is shown in Table 4. Furthermore, the upper limit of deposition time was restricted to AFM's imaging limit. This was dependent on the electrolyte composition. Next, the zinc deposit was peeled off the substrate using tweezers and placed on a Kimwipe® to dry in air at room temperature. Zinc samples were weighed once the samples were completely dried and the mass of each deposit was recorded.

Additionally, once the current is applied to the system, the in-house software (written in LabVIEW) also acquired the current I (μA) and potential E (V) over the deposition time.

This data combined with the mass of each deposit was used to calculate the current efficiency of each deposition using Faraday's law (as described in section 1.3). Dried samples were mounted to sample holders and imaged in SEM and AFM.

3.4 SEM imaging

The zinc samples for SEM imaging did not receive any surface cleaning or additional treatment. A JEOL 6400 scanning electron microscope was used to capture images for this thesis. The SEM instrument was operated at an accelerating voltage of 20 kV and beam current of 1nA and the vacuum chamber was maintained at approximately 10^{-6} mbar.

3.5 AFM imaging

The zinc samples for AFM imaging were not modified in anyway after being dried. A Bruker Instruments Nanoscope 3D Multimode Atomic Force Microscope was operated in tapping mode in air. All images were obtained using a TESPA cantilever (Bruker Probes) which had a nominal frequency of 320 kHz and a force constant of 42 N m^{-1}. Images for this thesis were collected at a raster scan frequency between 0.3-0.5 Hz with the offline plane fit engaged. Images were either 50 × 50 μm or 100 × 100 μm in size with a resolution of 512 × 512 pixel, which results in 0.0977 and 0.1953 μm/pixel respectively. As discussed previously, in order to compare all images equally, all of the raw 100 × 100 μm images were cropped to 50 × 50 μm and 256 × 256 pixels using Nanoscope Analysis 1.5 (Bruker software) and all raw 50 × 50 μm were binned by 2 using in-house program written in MATLAB. Thus, all images are compared at an equal resolution of 0.1953 μm/pixel. Every

sample was imaged at 3 different and random positions on the surface. After images were collected scaling analysis were performed on them.

3.5 Scaling analysis

Scaling analysis in this thesis was performed using either the truncated or truncated-with-binning scaling programs. Both of these scaling programs were written in-house to run in MATLAB (Mathworks) and are described in section 2.8. To perform this, the ACSII data files of each image were extracted using Nanoscope Analysis 1.5 AFM software (Bruker software). ACSII data files of the 50 μm cropped image were individually imported into the truncated scaling program; data files that required binning were imported and analyzed using truncated-with-binning scaling program.

3.6 Statistical analysis of the data

In this thesis, all standard errors were determined using Excel's linear regression with error propagation (LINEST function). This linear regression outputs the standard error of slopes when extracting: α, β, γ and β/α exponents from their associated plots. The roughness parameters δ, L_c and δ/L_c were determined over the multiple image sets and were averaged. For these parameters, the standard deviation rather than the standard error are used.

Results and Discussion

Chapter 4: Influence of Deposition Time and Glue Concentration

4.1 Comparison of imaging techniques

This section begins with a comparison between SEM and AFM imaging techniques on zinc deposits. Figure 14 shows an image obtained from a) SEM, b) AFM top view and c) AFM 3D view of a zinc sample that was electrodeposited for 30 minutes on an aluminum substrate from the standard electrolyte containing 3 mg L^{-1} glue, 2.7 mg L^{-1} sodium silicate and 9 mg L^{-1} of Licorice, or 3G, 2.7SS, 9L. The SEM image shows a morphology of electrodeposited zinc that compares well with other deposits produced from an electrolyte with similar glue concentrations [33]. These have been studied in [39] and typically consists of hexagonal platelets aligned at high angles (~ 70°) to the Al substrate. This confirms that the zinc samples produced using the protocols of this thesis match the structures of those produced under similar conditions elsewhere.

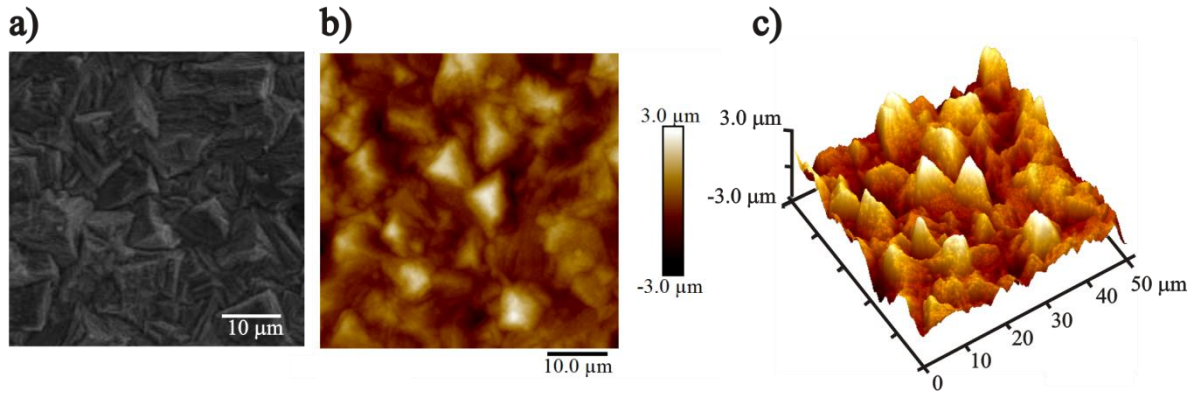

Figure 14: a) SEM, b) AFM top view and c) AFM 3D view images of a zinc sample produced on Al substrate after 30 minutes of deposition at cathodic current density of 44mA cm^{-2} from a standard electrolyte containing 3, 2.7 and 9 mg L^{-1} of glue, sodium silicate and licorice respectively.

Moreover, the AFM top view image (Figure 14b) when compared to the SEM image match well in structure. The AFM image was captured from the same sample as the SEM image, but over a different area of the surface. When comparing the two imaging techniques, it seems that the general size, shape and distribution of the surface features are alike, demonstrating that features shown in the AFM image are not modified by the AFM probe tip, thus ensuring that the surface characteristics of zinc samples captured using the AFM in tapping mode are reliable and not distorted. Furthermore, AFM imaging provides additional height information that is lacking in SEM. The height information in the top view image is represented by the color bar, where the lighter colours are elevation and the darker colours are depth of the surface. These variations of height are further visualized in the AFM 3D view (Figure 14c). The structures in the 3D image show that there is a distribution of features that range from a few to several micrometers in height and corrugation. As such, the collection of 3D data using AFM can be used to accurately quantify the growth and

roughness characteristic of zinc deposits and this is demonstrated with the application of scaling analysis.

4.2 Influence of deposition time on roughness quantified using scaling analysis

Scaling analysis and its application to quantify the surface roughness characteristics was demonstrated on zinc samples produced from the standard electrolyte containing 30G, 2.7SS, 9L. For this study, three independent zinc samples were produced at each deposition time (i.e., 3 replicates) and each sample was imaged on three different regions of the surface (i.e., in triplicate) resulting in 9 AFM images per deposition time. These images were originally collected at 100 × 100 μm and 512 × 512 pixels and the full results are presented in [74]. However, for this thesis, the same data was revisited after the images were cropped to 50 × 50 μm to have a size of 256 × 256 pixels to allow comparison of data from all experiments. The samples were produced with deposition times of 10, 30, 50, 70 and 90 minutes and their AFM top view and 3D view images are shown in Figures 15 to 19 consecutively. These images are presented with the same vertical and lateral scales so that the variations in surface features can be compared directly. It is visually apparent when observing these images that the surface features are relatively small in size both in lateral and height directions at a deposition time of 10 minutes and as deposition time increases these features increase in size both laterally and vertically. Furthermore, the distribution of surface features is relatively uniform in all images.

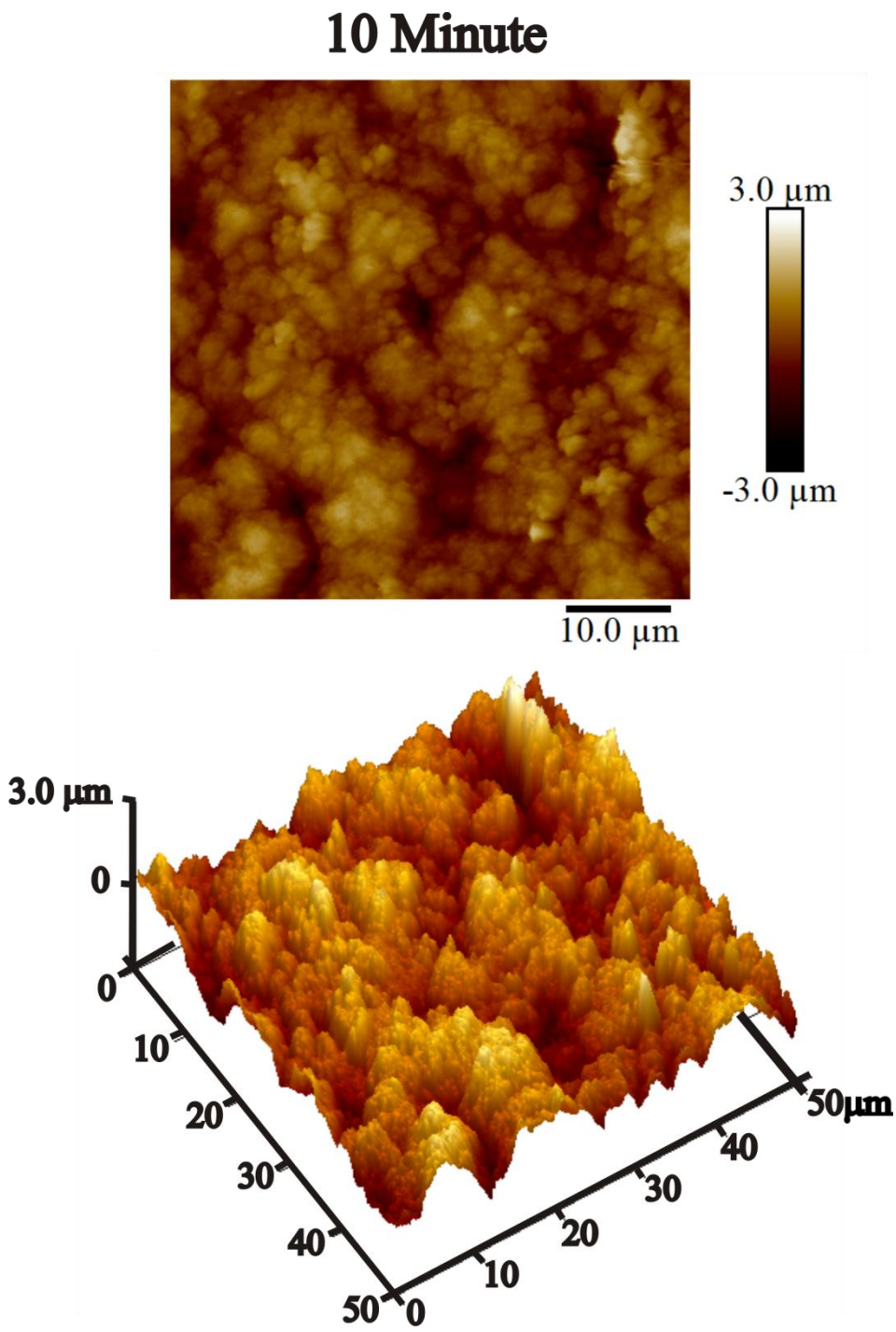

Figure 15: AFM images of a zinc sample deposited on an aluminum substrate over 10 minutes with a current density of -44 mA cm^{-2} from a standard electrolyte containing 30 mg L^{-1} glue, 2.7 mg L^{-1} sodium silicate, 9 mg L^{-1} licorice. Top: AFM top view. Bottom: AFM 3D view

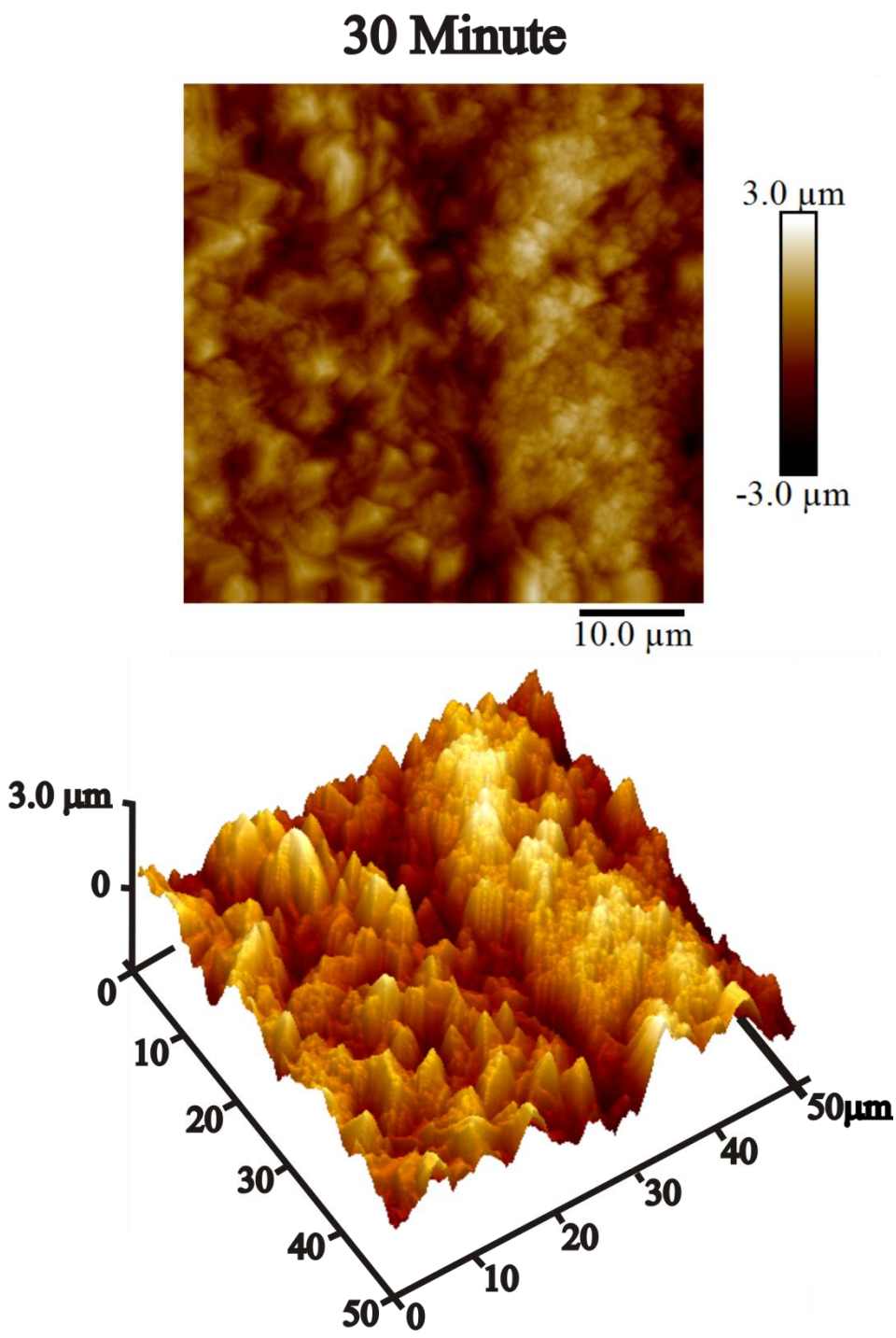

Figure 16: AFM images of a zinc sample deposited on an aluminum substrate over 30 minutes with a current density of -44 mA cm^{-2} from a standard electrolyte containing 30 mg L^{-1} glue, 2.7 mg L^{-1} sodium silicate, 9 mg L^{-1} licorice. Top: AFM top view. Bottom: AFM 3D view.

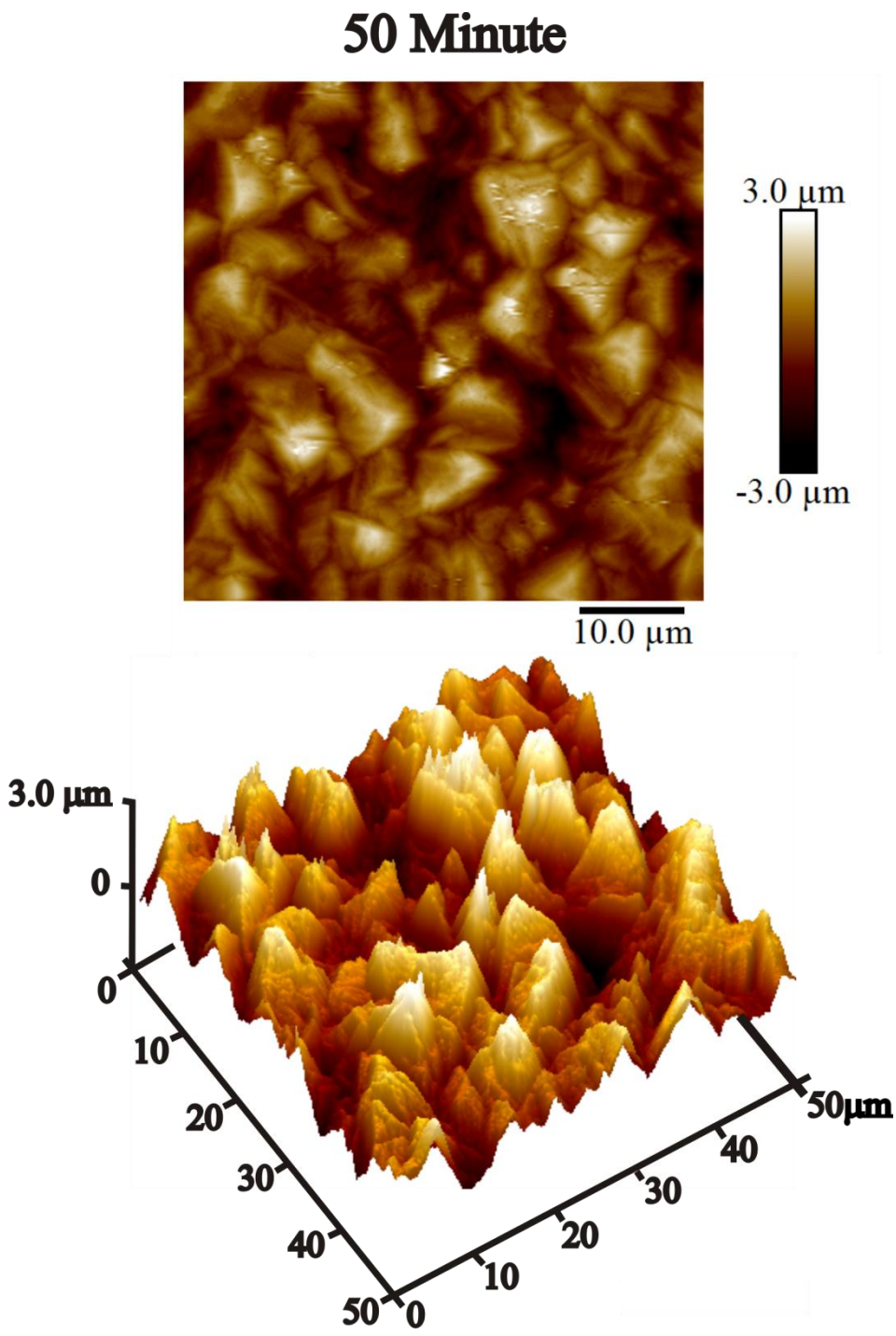

Figure 17: AFM images of a zinc sample deposited on an aluminum substrate over 50 minutes with a current density of -44 mA cm^{-2} from a standard electrolyte containing 30 mg L^{-1} glue, 2.7 mg L^{-1} sodium silicate, 9 mg L^{-1} licorice. Top: AFM top view. Bottom: AFM 3D view.

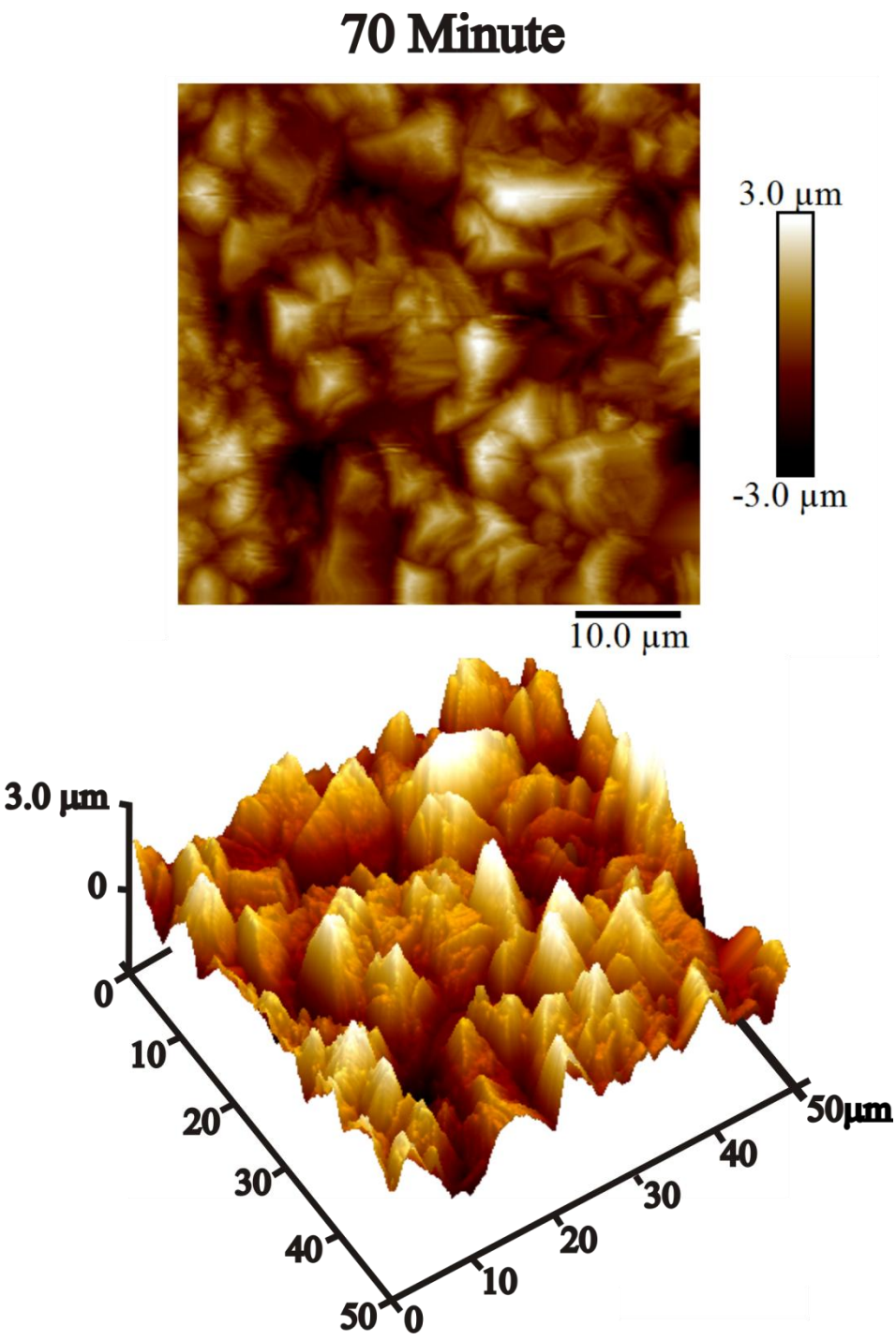

Figure 18: AFM images of a zinc sample deposited on an aluminum substrate over 70 minutes with a current density of -44 mA cm^{-2} from a standard electrolyte containing 30 mg L^{-1} glue, 2.7 mg L^{-1} sodium silicate, 9 mg L^{-1} licorice. Top: AFM top view. Bottom: AFM 3D view.

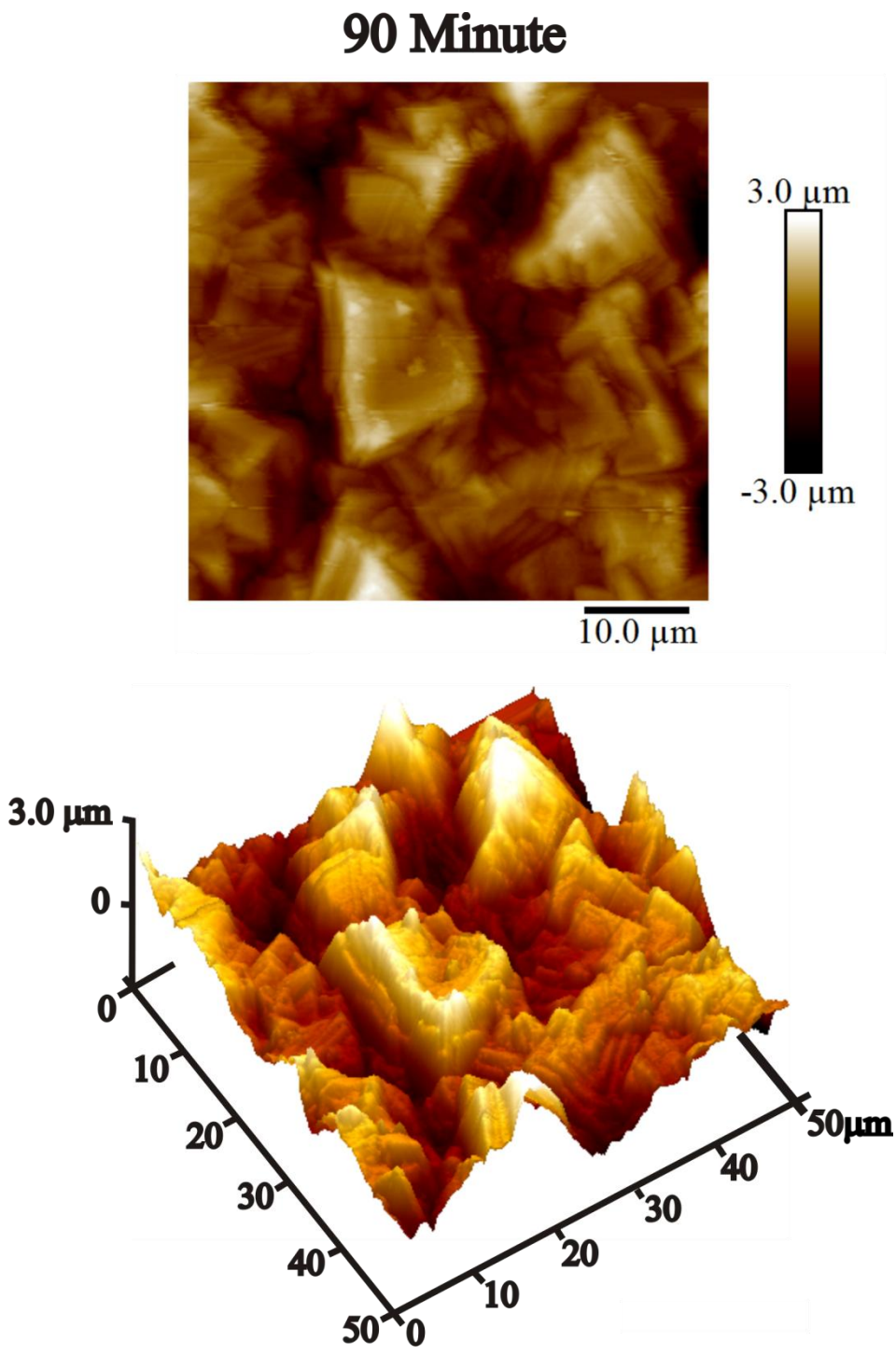

Figure 19: AFM images of a zinc sample deposited on an aluminum substrate over 90 minutes with a current density of -44 mA cm^{-2} from a standard electrolyte containing 30 mg L^{-1} glue, 2.7 mg L^{-1} sodium silicate, 9 mg L^{-1} licorice. Top: AFM top view. Bottom: AFM 3D view.

These visual growth trends are confirmed with the results of scaling analysis shown in Figure 20 for 10 minute (green) and 90 minute (blue) zinc deposits. Each trend in this figure represents the average of the individual scaling plots computed from the 9 AFM images collected at each deposition time and the error bars show the standard deviation. These plots show typical scaling behaviour, where at lower scaling lengths (L) there is a linear increase in the value of ξ until the critical length (L_c) is reached where the roughness plateaus. The same results are observed for the 90 minute deposit but the plateau is at a larger roughness value and occurs at a larger critical length. The average scaling plots obtained from 30, 50 and 70 minute deposits fall between these two trends but are not included in the graph for the purpose of visual clarity. The results presented in Figure 20 indicate that as deposition time increases from 10 to 90 minutes, the limiting roughness (δ, shown as horizontal dotted lines) and critical length (L_c, shown as vertical dotted lines) increase in value.

The numerical value of the limiting roughness was determined by taking the average the last 5 data points (i.e., roughness values) in a given scaling plot. This analysis was performed on each of the 9 scaling plots obtained per deposition time in order to get an average and standard deviation for the value of δ. With this approach, the results show that δ is 619 ± 70 nm after 10 minutes of deposition and 1213 ± 178 nm after 90 minutes of deposition under the conditions of this experiment.

The value of L_c was also extracted from the individual scaling plots and subsequently averaged over the 9 data sets per deposition time. However, L_c cannot be extracted without

the static exponent α. Because α is not time-dependent, it was not determined from each data set independently but rather from a global fit to the averaged scaling plots of the 5 time sets. This was achieved using a linear regression analysis (Excel LINEST) applied to the first 7 data points of the averaged 10, 30, 50, 70 and 90 minute scaling profiles simultaneously.

For the scaling plots in this thesis, the first 7 data points cover a difference of 0.6 in log L (i.e., a run of 0.6 on the x-axis on log scale). The regression gave a slope, intercept and the standard error. For the global fit to the 5 data sets, this resulted in $\alpha = 0.86$ with a standard error of 0.04; this is within the range of our result for the α value of 0.85 published in [74] when using the 100 × 100 μm images. As described in section 2.4.4 and equation 2.5, a value of $\alpha = 0.86$ gives n = 3.7, which indicates that zinc deposited onto an Al substrate from an electrolyte containing 30G, 2.7SS, 9L produces a self-affine surface with a growth mechanism that is controlled by surface diffusion with respect to deposition time. It is important to note that while our results in [74] are similar to the ones presented here, they were obtained from larger image size. The red line on Figure 20 shows the value of α; the statistical variation of 0.04 is not included on the plot.

After α was determined from the averaged scaling plots, it was applied to each of the 9 individual scaling plots per deposition time to extract L_c at the point where the α and δ lines intersect. This produced 9 L_c values per deposition time which were averaged and the standard deviation taken. From this analysis, the critical length (L_c), which represent the width of the features, increases from 3950 ± 515 nm from 10 minute deposits to 8624 ±

1471 nm for 90 minute deposits. Lastly, the 9 values of δ and L_c that were computed for each individual scaling plot were used to calculate the average and standard deviation for the δ/L_c ratio. This value cannot be extracted by visual inspection of the images alone. The analysis presented here shows that the values of δ/L_c vary from 0.157 ± 0.003 at 10 minutes to 0.141 ± 0.003 at 90 minutes.

This method of data analysis was used throughout this thesis; all calculations of L_c were performed using a static value of α (i.e., not including the standard error in α). While the standard deviations computed for L_c and δ/L_c were directly measured, they would be an smaller compared to those computed from error propagation (see appendix A).

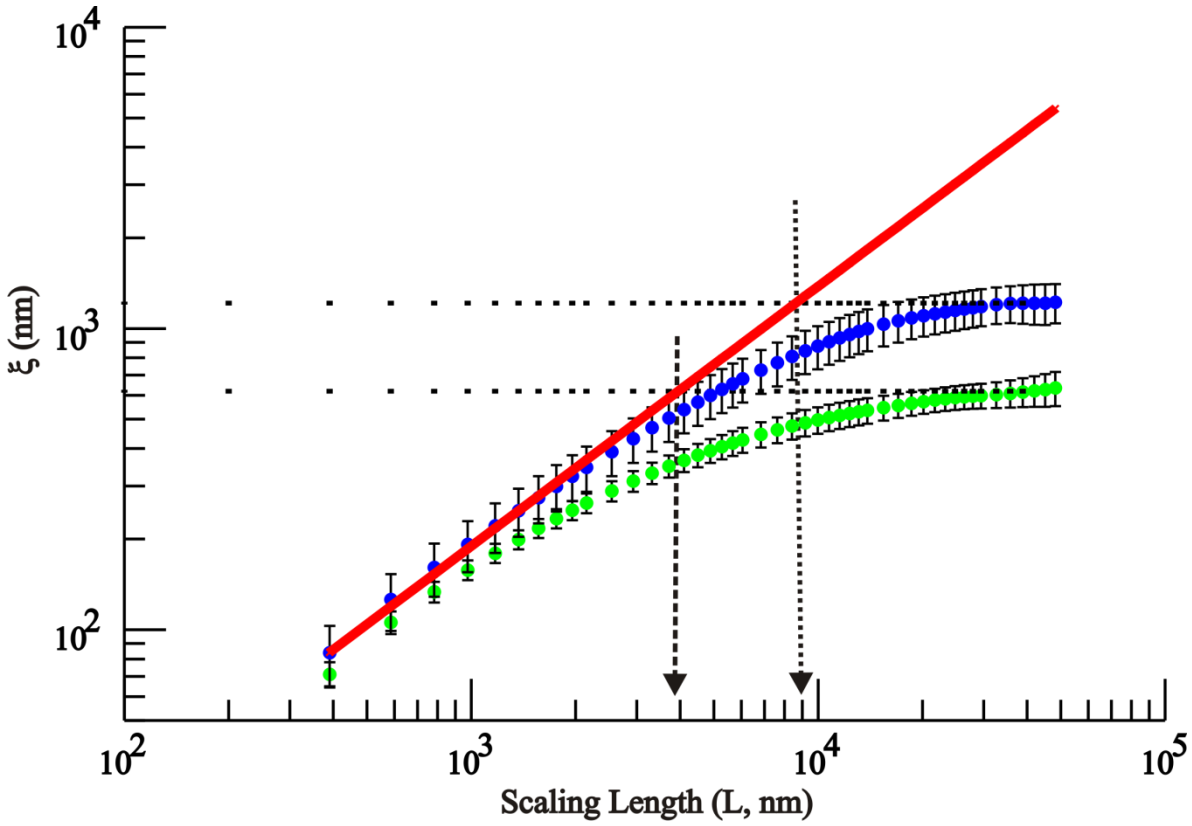

Figure 20: Scaling analysis result of 10 (green) and 90 minute (blue) zinc samples deposited on an aluminum substrate with a current density of -44 mA cm^{-2} from a standard electrolyte containing 30 mg L^{-1} glue, 2.7 mg L^{-1} sodium silicate, 9 mg L^{-1} licorice. This log ξ versus log L plot is to extract roughness parameters such as the static growth exponent (α, red line), limiting roughness (δ, horizontal dotted lines) and critical length (L_c, vertical dotted lines) of the zinc deposits at the indicated deposition times. The error bars represent standard deviation from 9 images per deposition time.

Once the roughness parameters δ, L_c, and δ/L_c are determined from scaling plots, they are plotted versus deposition time on a log-log graph to extract growth exponents: β, β/α and γ. In figure 21, a) log δ versus log t, b) log L_c versus log t and c) log δ/L_c versus log t are presented.

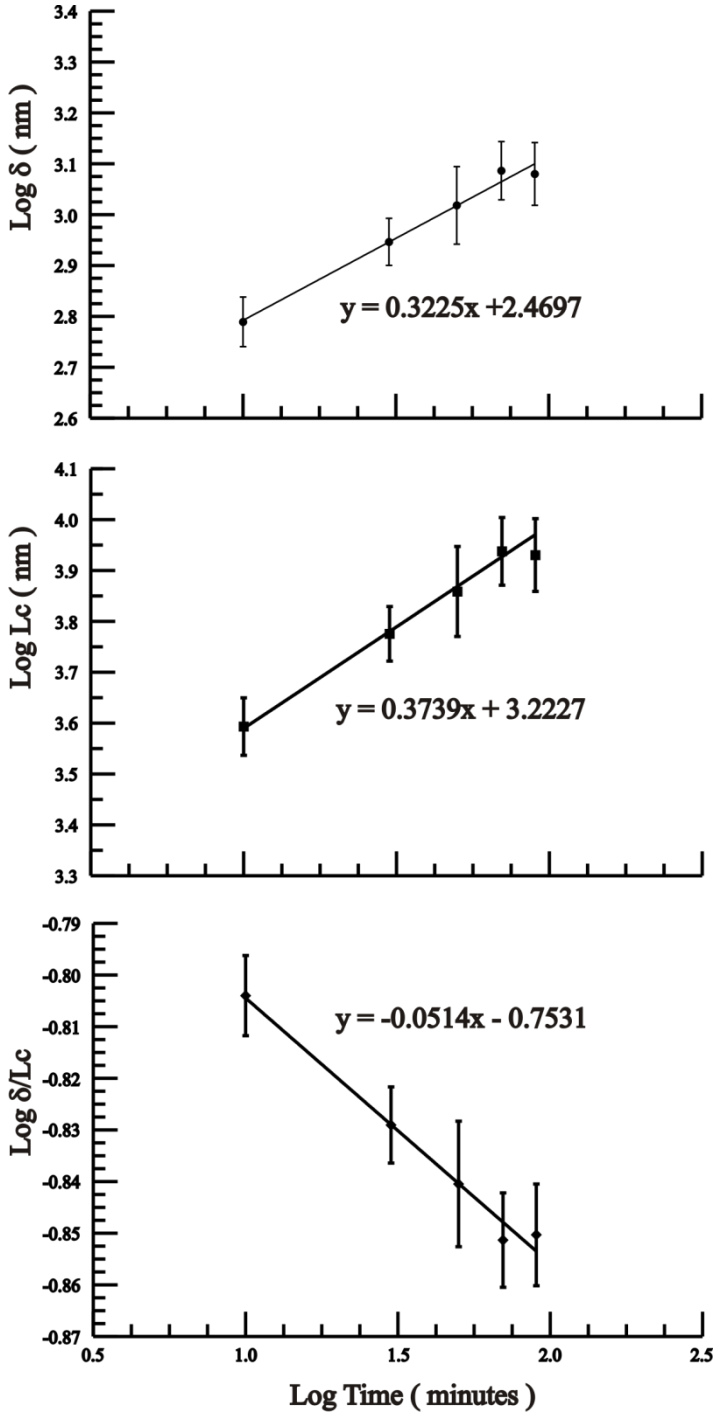

Figure 21: Roughness parameters: a) log δ, b) log L_c and c) log δ/L_c versus log t for zinc deposits produced on an aluminum substrate from a standard electrolyte containing 30, 2.7, 9 mg L^{-1} of glue, sodium silicate, and licorice, respectively. Growth exponents β, β/α and γ were determined from the slope of a), b) and c), respectively using linear regression analysis and error propagation.

The increase in both the limiting roughness (δ) and critical length (L_c) with deposition time is visualized in and might be expected since more zinc is being deposited with the increasing deposition time (see Figure 21a and b). However, the δ/L_c plot shows a decrease with deposition time in Figure 21c. This trend indicates that the growth in the lateral direction is faster than in the vertical one; these results are in-line with visual observation of AFM images, and with the action of levelling agents such as glue (where it is thought to inhibit deposition at the protruding parts of the surface and allow growth to happen in the recesses [70]). Given these results, it appears that scaling analysis is extracting the roughness parameters accurately at least under the conditions of the experiment.

The plots in Figure 21 were used to extract growth exponents a) β, b) β/α and c) γ from their slopes (shown by the equations in the respective figures and output from regression analysis). These are time-dependent exponents, as described in sections 2.4.5 and 2.4.6, and can indicate the rate at which surface features are changing.

The results show that the rate of lateral growth ($\beta/\alpha = 0.374 \pm 0.030$) is higher than growth in height ($\beta = 0.323 \pm 0.026$), indicating smoothing of surface features thus resulting in a decrease in aspect ratio ($\gamma = - 0.051 \pm 0.004$). These results are consistent with the mechanism of levelling agents in the system.

The values of β, β/α and γ give insight on the rate of the growth in surface feature height, width and aspect ratio respectively as described in Equations 2.2, 2.3 and 2.4. For example, a purely stochastic surface ($\alpha = 0$) with no smoothing at all has a high value of $\beta = 0.5$, indicating a growth in height only with no lateral growth of features resulting in $\beta/\alpha = 0$

[68]. A higher value of β/α indicates a growth rate faster in the lateral width of features and some form of a smoothing mechanism. Also, a surface with a smoothing mechanism would result in features to grow wider more rapidly than vertically and thus provide a more negative value of γ.

These exponents have been used to predict surface features of industrially relevant copper electrodeposits [70]. This was achieved with scaling analysis conducted on AFM images from a series of deposition times under 10 minutes. Projections into longer deposition times were made and compared with the results of White Light Interference Microscopy of copper electrodeposits after 16 hours, as well as 16 days. The limiting roughness of the 16 hour and 16 day deposits were comparable with projections from the short deposition times with remarkable accuracy. This linear projection requires that the mechanism of deposition does not change over the prolonged period.

This study demonstrates the applicability of the scaling analysis to zinc deposits as a function of deposition time. In the following section, the influence of glue will be presented using a single deposition time, however, with a range of glue concentrations.

4.3 Influence of glue on roughness characteristics of zinc electrodeposits

In this study, the glue concentrations of 3, 7.5, 15, 22.5, 30, 37.5 and 60 mg L^{-1} were investigated to observe the influence on roughness characteristics but at a single deposition time of 30 minutes. The electrolyte was prepared in the same manner as the previous study, where the standard electrolyte was modified to contain 2.7 mg L^{-1} sodium silicate and 9 mg L^{-1} licorice and one of the seven glue concentrations stated above resulting in seven

different electrolyte combinations. The 30 minute deposition time was chosen because, for this electrolyte, it allows a deposit that covers the substrate completely while it is easily stripped off of the substrate. Moreover, it allows deposit feature sizes that are within the operating range of the AFM. This study was completed in 3 replicates, i.e., 3 samples from each electrolyte condition and 3 AFM images per sample.

A representative SEM and top view AFM image of 30 minute zinc electrodeposits produced from 3, 7.5 and 15 mg L^{-1} of glue are shown in Figure 22a, b and c, respectively. Images of samples produced from glue concentrations of 22.5, 30 and 37.5 mg L^{-1} are shown in Figure 23a, b and c, respectively and Figure 24 represents a zinc deposit produced from an electrolyte containing 60 mg L^{-1} of glue. These AFM images are also shown in Figure 25a-g in 3D view. In Figure 22, the SEM and top view AFM images show, that as the concentration of glue is increased from 3 to 15 mg L^{-1}, there is little difference observed in the height of surface features from visual inspection. However, it is visually apparent that the surface features decrease in width as the glue concentration is increased. In fact, these trends of decreasing feature width continue in Figures 23 and 24 for samples produced from 22.5 to 60 mg L^{-1} of glue. This is further apparent in the 3D view (Figure 25a-e), where it can be seen that the variation in surface feature heights are approximately the same, while the feature widths decrease as glue concentration is increased from 22.5 to 60 mg L^{-1}. However, on close inspection of the sample produced from 60 mg L^{-1} glue (Figure 24 and Figure 25g), a new type of surface arrangement is observed. While there are numerous small features on this deposit, they exist on larger underlying features. This is most apparent for the sample produced with 60 mg L^{-1} glue, but is also visualized in the sample

produced from 37.5 mg L^{-1} glue (Figures 23c and 25f). This is an interesting result because there are two distinct feature sizes on a single surface; the observation is more clearly seen in the AFM images compared to the SEM.

Scaling analysis was conducted on the 9 images collected per electrolyte condition and averaged to give the data in Figure 26. Selected plots are presented for 30 minute deposits from the electrolyte containing a) 3, b) 30 and c) 60 mg L^{-1} of glue and the error bars represent the standard deviation of the 9 image sets. The static exponents α were again determined from the first 7 data points of the scaling plot (i.e., a run of 0.6 on the log x scale). Since each electrolyte conditions is different, the static exponent was not extracted from a global fit of each trend but rather from each plot individually.

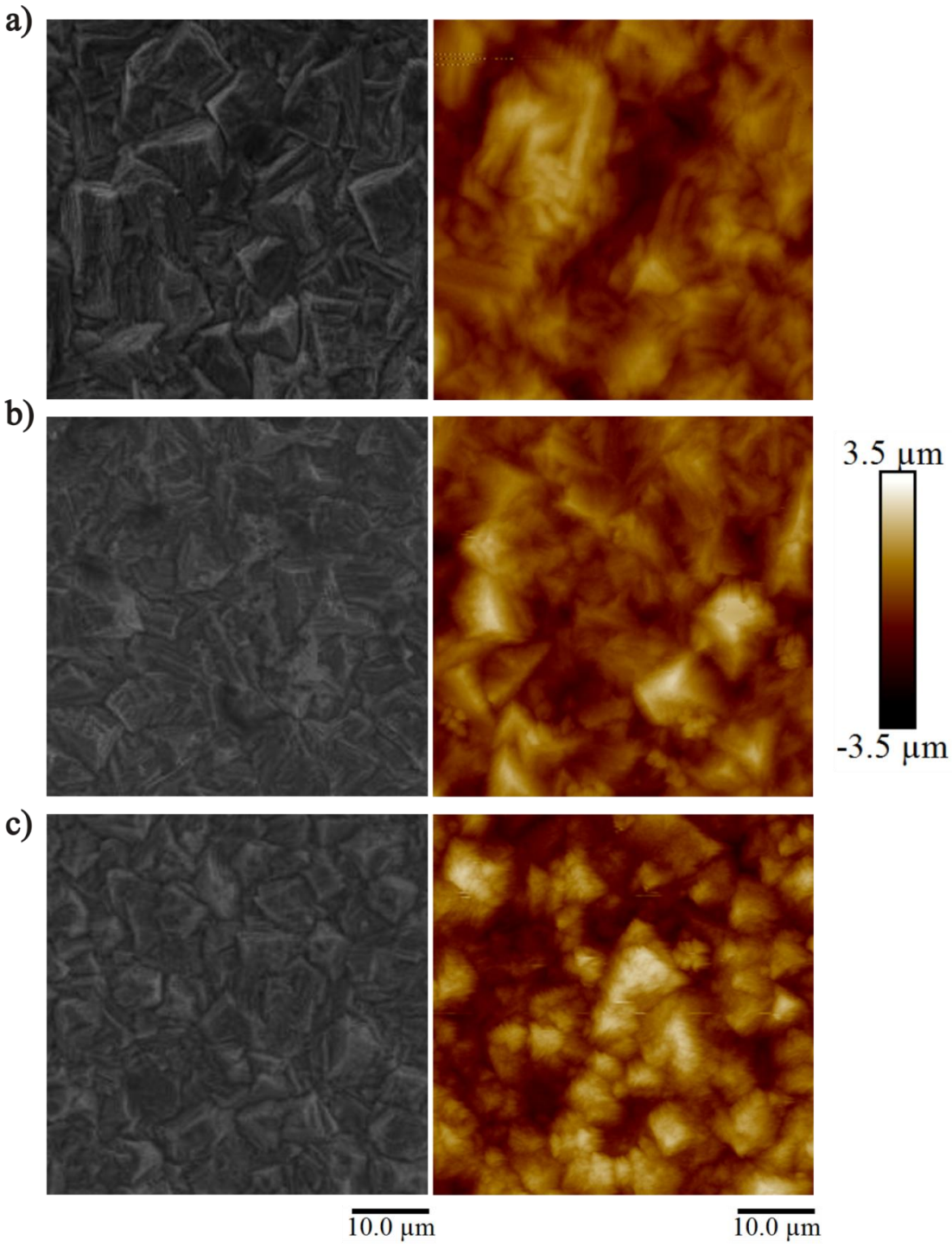

Figure 22: Representative SEM (left) and AFM top view (right) images of 30 min zinc deposits produced on an aluminum substrate from a standard electrolyte containing 2.7 mg L^{-1} sodium silicate, 9 mg L^{-1} licorice and a) 3, b) 7.5 and c) 15 mg L^{-1} glue. The height scale of all images was set to the same value for direct comparison.

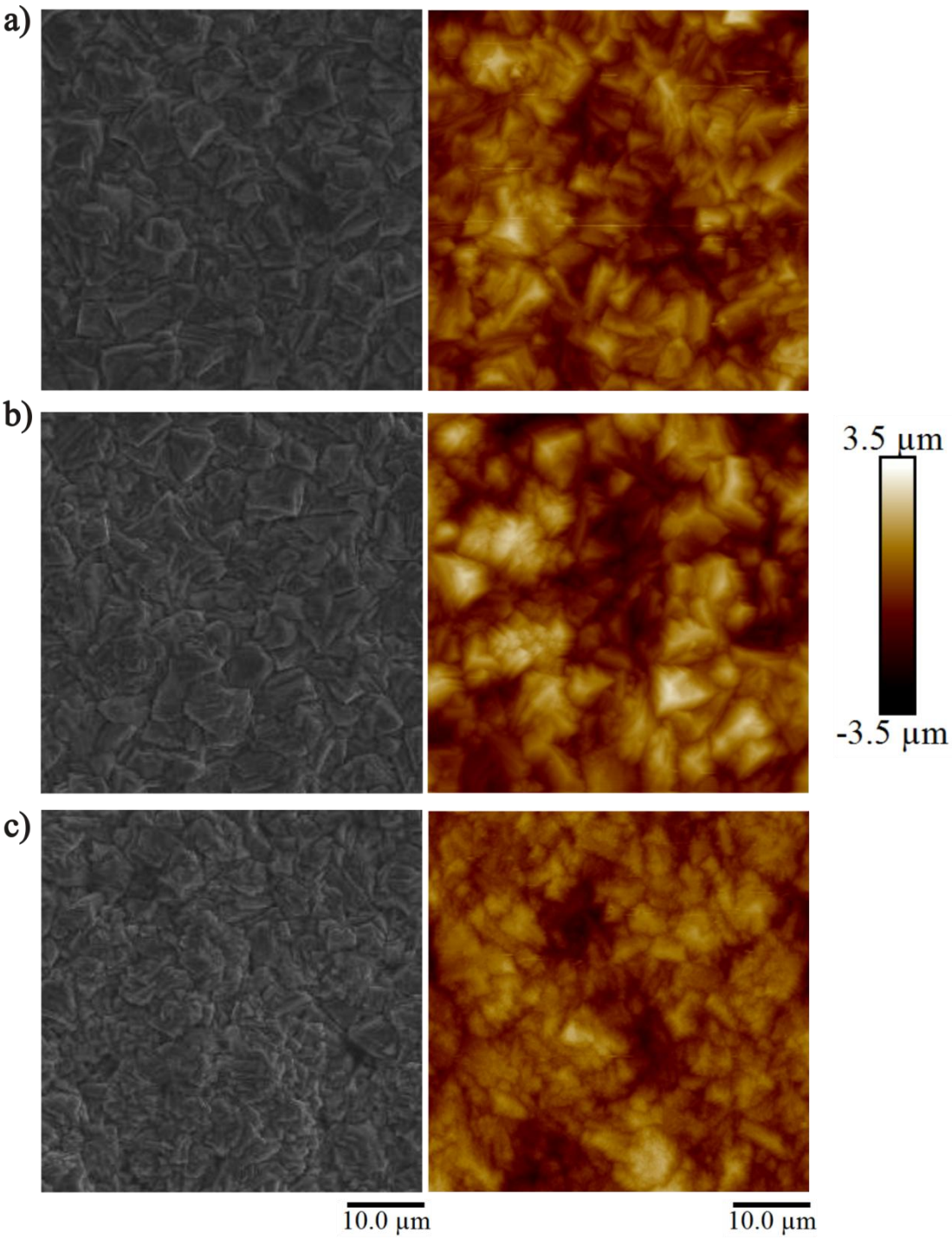

Figure 23: Representative SEM (left) and AFM top view (right) images of 30 min zinc deposits produced on an aluminum substrate from a standard electrolyte containing 2.7 mg L^{-1} sodium silicate, 9 mg L^{-1} licorice and a) 22.5, b) 30 and c) 37.5 mg L^{-1} glue. The height scale of all images was set to the same value for direct comparison.

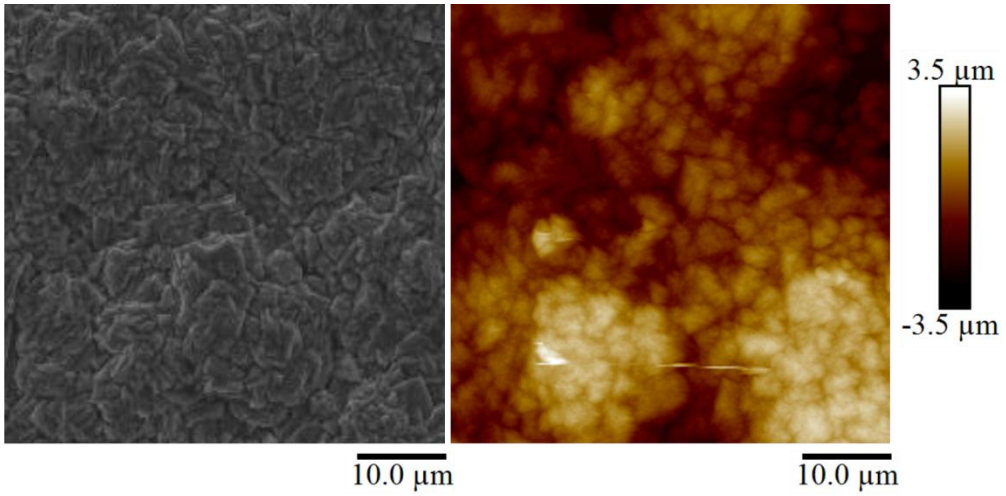

Figure 24: Representative SEM (left) and AFM top view (right) images of 30 min zinc deposits produced on an aluminum substrate from a standard electrolyte containing 2.7 mg L^{-1} sodium silicate, 9 mg L^{-1} licorice and 60 mg L^{-1} glue. The height scale of all images was set to the same value for direct comparison.

This was done because the static growth exponent is a function of electrolyte composition and not deposition time. Furthermore, it was noted that electrolytes containing more than 30 mg L^{-1} glue produced scaling plots with a second linear region at larger scale lengths. This is visually apparent in Figure 26c and in this study it is referred to as α' (as described in section 2.6). As noted previously, the extraction of α occurred over a run of 0.6 on log L as a result from fitting 7 data points. For our images, the same 0.6 run of log L within the α' region would consist of 18 data points due to the nature of the log plot. As such, in order to have a similar regression analysis to that performed on α, only every third data point was used in extracting α' from a seven-point analysis. With this approach, the correlation coefficient of α was 0.994 while for α' it was 0.998 and 0.999 for 37.5 and 60 mg L^{-1} glue

respectively. This strong correlation indicates a true second region of linear behaviour. Any samples created with less than 30 mg L^{-1} of glue had correlation coefficients well below 0.994 over this range and therefore a second linear region was not considered for those plots. For the averaged scaling plot (Figure 26c) of zinc sample produced from an electrolyte containing 60 mg L^{-1} glue has an $\alpha' = 0.500 \pm 0.001$. This exponent when used in equation 2.5, indicates a second or competing deposition mechanism. This process, described as bulk diffusion or progressive nucleation [70], results in large underlying features with smaller features on top of them.

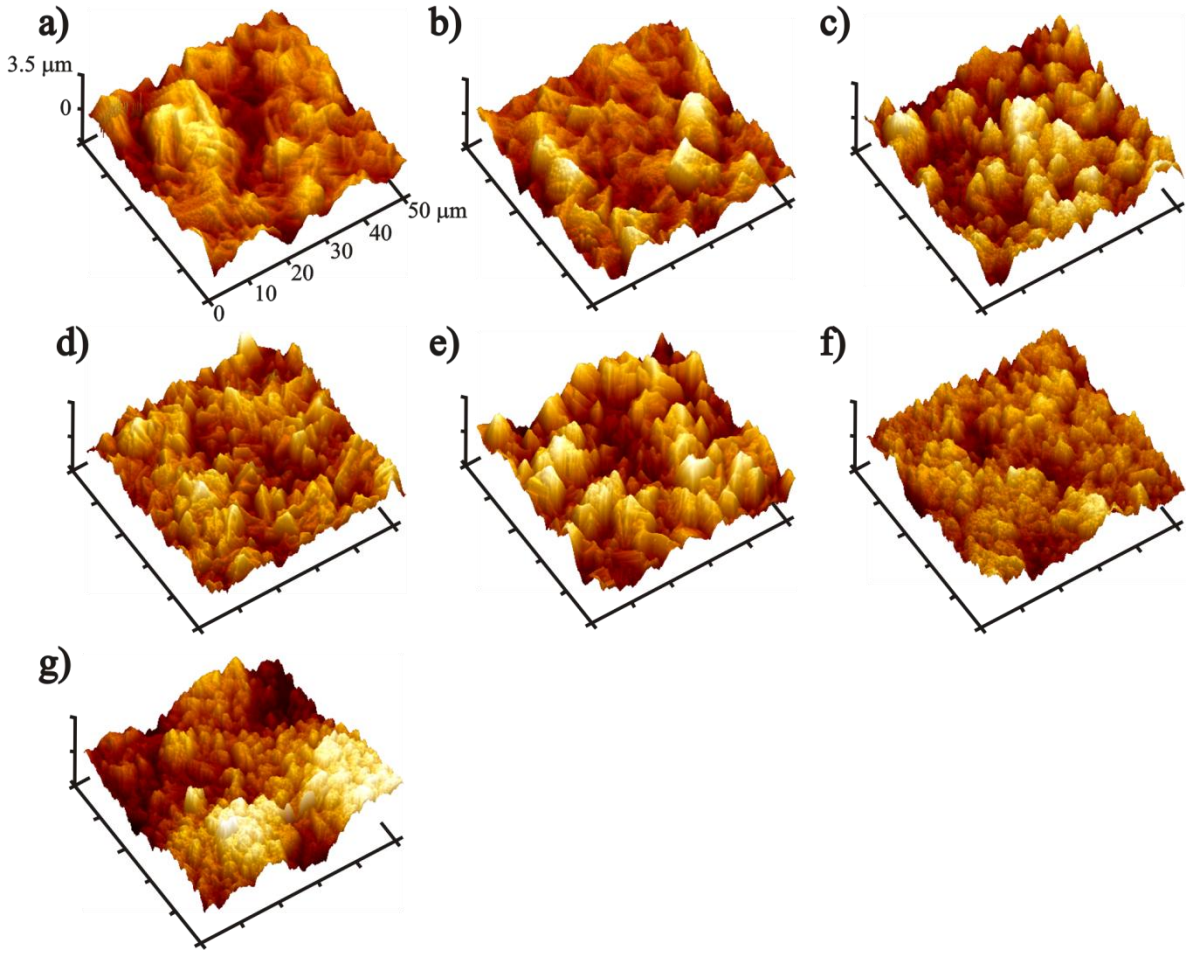

Figure 25: 3D view AFM images of 30 min zinc deposits produced on an aluminum substrate from a standard electrolyte containing 2.7 mg L^{-1} sodium silicate, 9 mg L^{-1} licorice and a) 3, b) 7.5, c) 15, d) 22.5, e) 30, f) 37.5 and g) 60 mg L^{-1} glue. The scales of all images were set to be the same and is only shown in a) for the purpose of clarity.

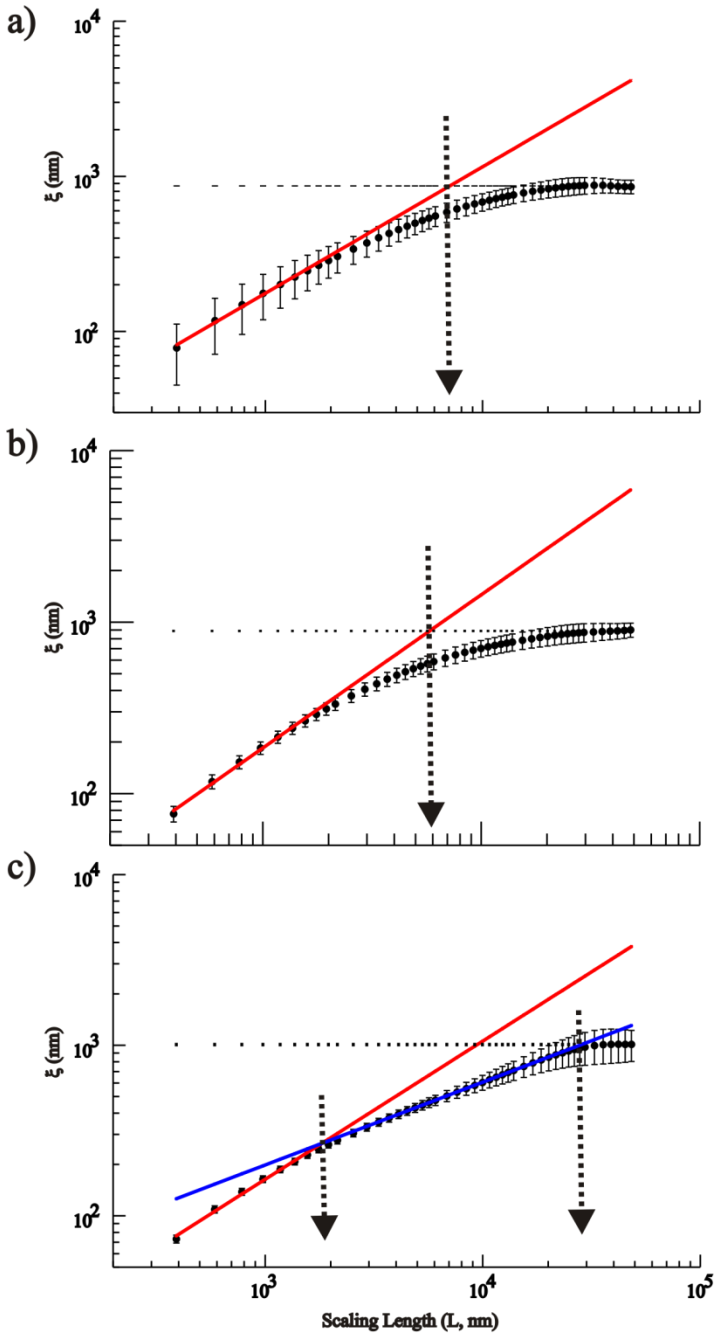

Figure 26 : Averaged scaling plots of zinc samples produced from an electrolyte containing a) 3, b) 30 and c) 60 mg L^{-1} glue. The error bars are the standard deviation from 9 AFM images, where the red line is the static growth exponent (α) and in c) the blue line is the second linear region (α'), where the second or competing mechanism leading to a surface with two distinct features is extracted. The horizontal dotted line is where limiting roughness (δ) is extracted and the vertical dotted lines are where L_c (a, b), L_c' and L_c'' (c) are extracted.

Moreover, the scaling plots in Figures 26a-c, show that δ does not increase or decrease significantly with elevated glue concentrations. This result is the same with what was observed visually from the AFM images. Furthermore, it demonstrates that surfaces with different morphology characteristics can lead to a similar limiting roughness values. In addition, the critical length is noted in Figures 26a and b to decrease when going from 3 to 30 mg L^{-1}, respectively. For glue concentrations higher than 30 mg L^{-1} the scaling plots with two linear regions are used to extract two critical lengths (L_c' and L_c''). For example, in Figure 26c, L_c' which is the width size of the smaller features is extracted from the intersection of α with δ and L_c', which represents the width of the larger underlying features is extracted from the intersection of α' and δ. The roughness characteristic are plotted versus glue concentration in Figures 27 and 28. The δ versus glue concentration (Figure 27a) plot shows no trend as all error bars overlap. Also, the L_c versus glue concentration (Figure 27b) plot shows that as glue levels are increased from 3 to 30 mg L^{-1} the feature widths appear to decrease, albeit with overlap in the error bars (see inset of Figure 27b) and once the amount of glue reaches the critical concentration of 37.5 mg L^{-1} deposition of two distinct surface features are apparent. Here, small features appear on top of larger underlying features consistent with the images. These two features are represented by gray (small features) and open (larger features) diamond symbols.

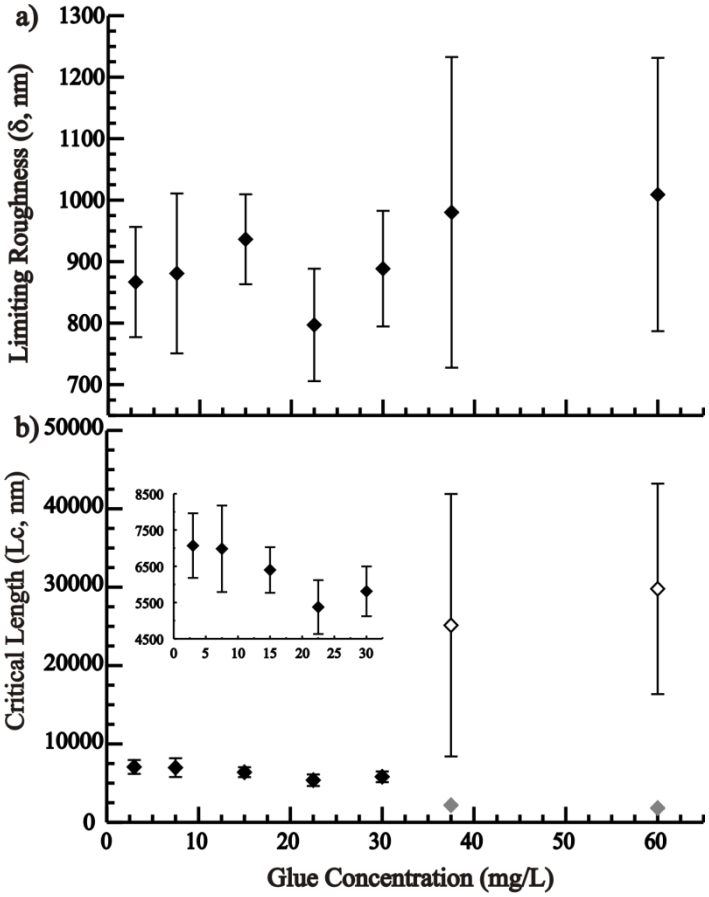

Figure 27: Analysis of roughness parameters of 30 min zinc deposits produced on an aluminum substrate from a standard electrolyte containing 2.7 mg L^{-1} sodium silicate, 9 mg L^{-1} licorice and varying glue concentrations: a) δ, b) L_c versus glue concentration. Each data point represents analysis of 9 images from three independent trials and the error bars are the standard deviation of this analysis. Data points with gray shading represent a roughness parameter of the small surface features and open symbols are used to represent the parameter of the larger underlying features. In b), the inset represents an expanded view of the data between 3 and 30 mg L^{-1} of glue.

The clearest trend is observed in the δ/L_c plot showing an increase in δ/L_c for the features (Figure 28a). This is seen in the inset of the figure that is restricted to glue concentrations between 3 and 30 mg L^{-1}. Moreover, as glue concentrations are increased further, it is seen

that the two different features result in two δ/L_c ratios where small features have a high ratio (gray diamonds) and the larger features have a lower ratio (open diamonds).

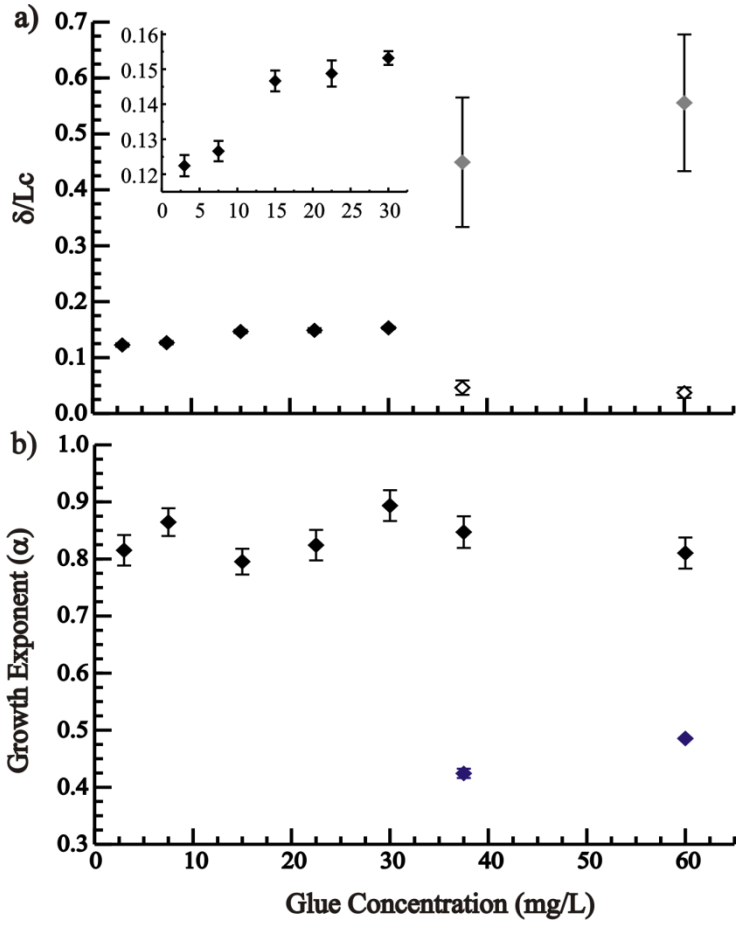

Figure 28: Analysis of roughness parameters of 30 min zinc deposits produced on an aluminum substrate from a standard electrolyte containing 2.7 mg L^{-1} sodium silicate, 9 mg L^{-1} licorice and varying glue concentrations: a) δ/L_c, b) α versus glue concentration. Each data point represents analysis of 9 images from three independent trials and the error bars represent the standard deviation of this analysis. Data points with gray shading represent a roughness parameter of the small surface features and open symbols represent the parameter of the larger underlying features. The blue symbol represents the second/competing static growth exponent (α'). In a), the inset represents an expanded view of the data between 3 and 30 mg L^{-1} of glue.

In Figure 28b, α and α' are shown. It can be noted that α fluctuates around 0.8 for glue concentrations between 3 and 30 mg L^{-1} while α' = 0.4 and 0.5 for 37.5 and 60 mg L^{-1}, respectively. This indicates that when glue concentrations are ≤ 30 mg L^{-1}, the growth mechanism is surface diffusion (n ~ 4) leading to smaller surface features.

Above 30 mg L^{-1}, it is noted that a second competing diffusion limited or progressive nucleation mechanism is in play to produce the larger underlying features. This may be due to the fact that, at higher glue concentrations, the surface diffusion of zinc adatoms (refer to Figure 3 in the introduction) is hindered by adsorbed glue. Because of this, the diffusion mechanism is altered or hindered resulting in nucleation and growth of zinc on the surface.

In summary, zinc surface features tend to decrease in width and increase in δ/L_c when glue concentration is increased while the deposition time, current density and other components of the electrolyte were held constant. Moreover, the results of the study show that, once a critical concentration of glue additive is reached in the electrolyte, a second growth mechanism also plays a role in influencing the morphology of the deposit. It is also of interest to note that zinc samples produced with two growth mechanisms were also very brittle; removal of these deposits from the substrate surface became difficult without breaking the sample. These results have been reported in the Journal of Applied Electrochemistry [74], where the analysis was conducted on the 100 × 100 μm with a size of 512 by 512 pixels and the results are consistent with what is shown here for the 50 × 50 μm images. In addition, the results of these experiments demonstrate the ability of the scaling analysis to be used to quantify and understand the morphology of zinc metal deposits as a function of deposition conditions. This prompt the question: how does a

variation in other additives influence zinc morphology? In the next Chapter, the effects of sodium silicate and licorice on zinc morphology are investigated.

Chapter 5: Influence of Sodium Silicate and Licorice on Zinc Electrodeposit Morphology

5.1 Variations in sodium silicate concentration with high levels of glue

In this section, the influence of sodium silicate on the roughness characteristics of zinc deposits is examined. Zinc samples were produced from the standard electrolyte modified with 30 mg L^{-1} glue, 9 mg L^{-1} licorice and a range of sodium silicate concentrations from 0, 1.35, 2.7, 5.4, 13.5 and 27 mg L^{-1}. Note that this is the same electrolyte composition as in Chapter 4 but with a range of sodium silicate and the deposition times are 10, 30, 50, and 70 minutes. For this initial study, the electrolyte was prepared and only one deposit at each deposition time was made from it, unlike the three made in the previous chapter. However, AFM images were acquired in triplicate on each sample. These three images per sample were acquired to give standard deviation and error analysis but on one trial only. Initially, zinc samples were deposited from an electrolyte containing 0 mg L^{-1} sodium silicate (i.e., 30G, 0SS, 9L) and were analyzed to see if typical scaling behaviour would manifest. In a plot of log ξ versus log L, shown in Figure 29c, there is a linear increase in the region $L << L_c$ followed by a plateau at $L > L_c$ similar to what was shown in Chapter 4 but with subtle differences in roughness parameters δ and L_c may be apparent on close inspection.

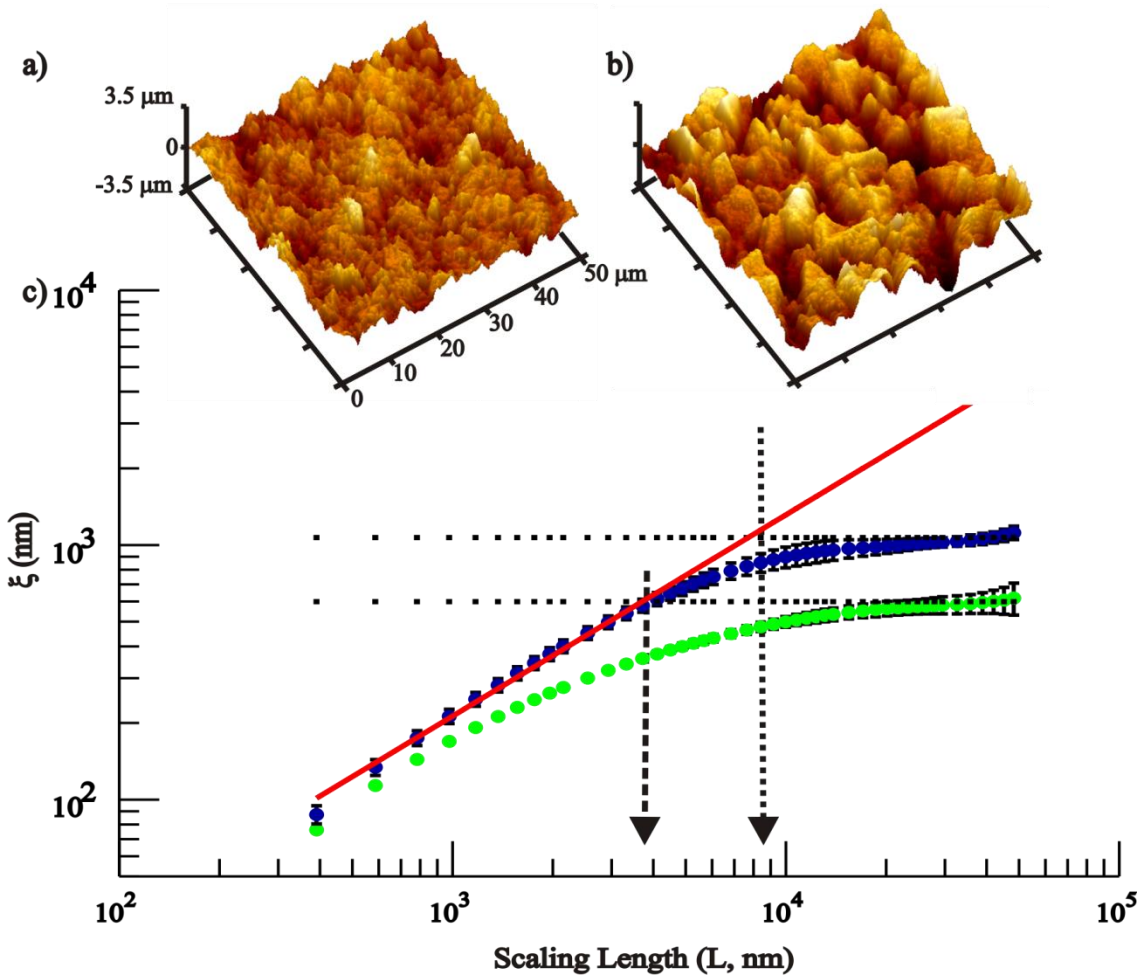

Figure 29 : AFM 3D view images of a) 10 minute and b) 70 minute zinc samples produced on an aluminum substrate from an electrolyte containing 0 mg L^{-1} sodium silicate, 30 mg L^{-1} glue, 9 mg L^{-1} licorice. Data in c) are the average scaling plots from 3 AFM images of one 10 minute (green) and one 70 minute (blue) deposits where the error bars represent standard deviation of 3 AFM images obtained on 1 sample per deposit condition. Horizontal dotted lines are to show the limiting roughness (δ) and the vertical dotted lines represent the critical length (L_c). The red line is the static exponent (α) and was globally fitted the first 7 data points of 10, 30, 50 and 70 minute averaged data using linear regression and error propagation.

In Figure 29 a) and b), representative AFM images are presented for 10 and 70 minute zinc samples respectively. It is visually evident from these images that as deposition time increases from 10 minutes to 70 minutes, the surface features increase in both height and

width. In Figure 29a, it can be seen that the surface features are small and numerous, whereas in Figure 29b the zinc grains are larger both in height and width and are fewer in number. This is confirmed with their respective scaling plots in Figure 29c for 10 minute (green) and 70 minute (blue) data sets. While 30 and 50 minute data are not presented in this plot, they were still used to calculate α by the usual method to obtain a value of 0.79 with a standard error in the slope of 0.07. This value again indicates a surface smoothing mechanism dominated by surface diffusion. Furthermore, when δ, L_c and δ/L_c are plotted on a log-log scale versus deposition time, the same trends as seen in the previous chapter are manifested. The roughness parameters versus deposition time are presented in Figure 30a) log δ, b) log L_c and c) δ/L_c. It is observed that the limiting roughness increases with deposition and a slope of $\beta = 0.311 \pm 0.039$ is extracted. Also, the critical length or grain size increases with deposition time with a slope $\beta/\alpha = 0.393 \pm 0.049$. Even in the absence of sodium silicate, the leveling properties are consistent with those in Chapter 4 which may indicate that leveling is dominated by glue.

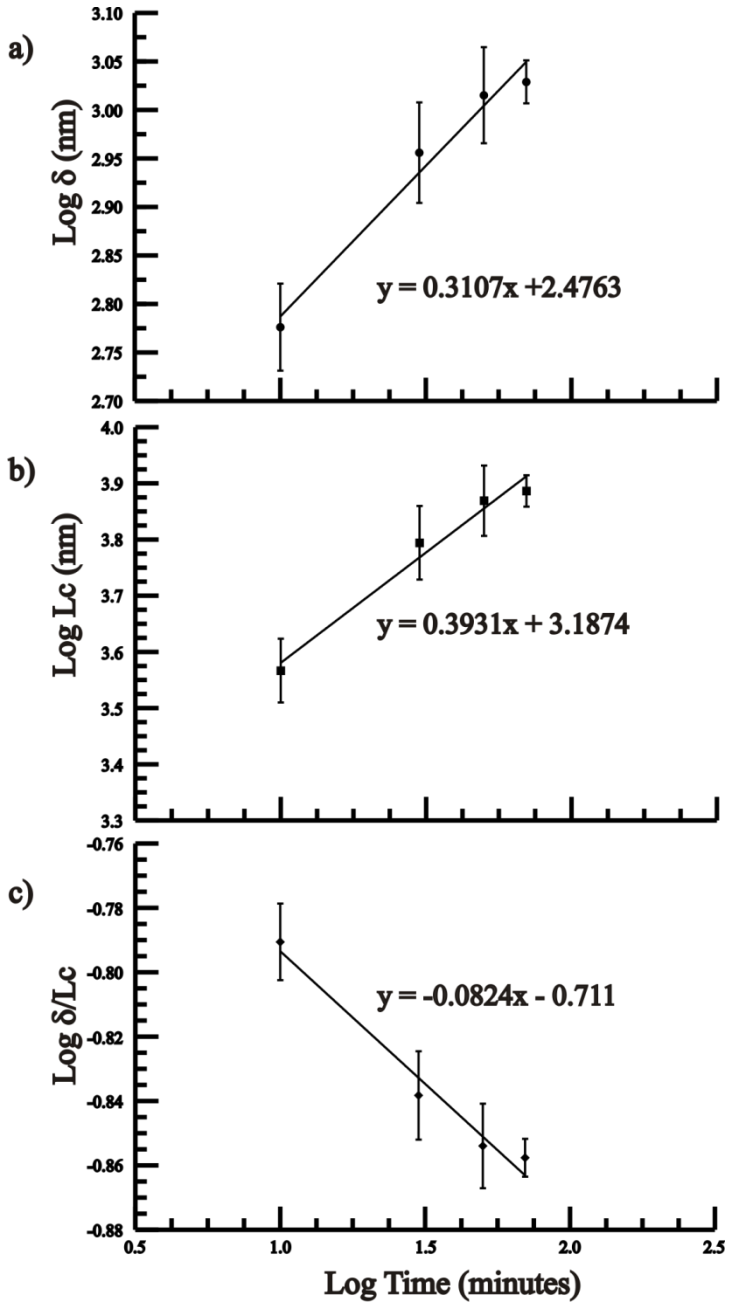

Figure 30: Average a) log δ, b) log L_c and c) log δ/L_c versus log deposition time of zinc samples electrodeposited on an aluminum substrate from an electrolyte with additive concentrations of 0 mg L^{-1} sodium silicate, 30 mg L^{-1} glue, 9 mg L^{-1} licorice. The error bars represent standard deviation of 3 AFM images obtained on one image per deposition condition. Equations of each trend line are included in their respective plot.

Therefore, this results in a decrease in δ/L_c and a slope of γ = -0.082 ± 0.010.

Interestingly, the scaling plots for samples produced from 1.35, 2.7 and 5.4 mg L^{-1} sodium silicate showed the typical scaling plot behaviour. However, at a 70 minute deposition time a sample produced from the higher end of sodium silicate concentrations (13.5 and 27 mg L^{-1}), give rise to scaling plots with two α values. This was confirmed with a second linear region having a correlation coefficient above 0.992; the result was shown in a conference proceeding [75]. It is emphasized that this observation was made from a single sample produced at a single deposition time. Even so, the analysis of δ, L_c and δ/L_c was performed for data with only one α value. Therefore, only 0, 1.35, 2.7 and 5.4 mg L^{-1} sodium silicate are discussed below. Also, since the standard error in γ was low, it indicates that surface features are growing in height and width at a relatively consistent rate. Therefore, for the remainder of this thesis, the δ/L_c ratios and γ values are emphasized while the log δ, log L_c are shown only in the Appendix B.

Figure 31 shows a comparison of the log δ/L_c versus log t of selected zinc samples produced from an electrolyte containing 0, 1.35, 2.7 and 5.4 mg L^{-1} sodium silicate. Except for the data produced from 1.35 mg L^{-1}, all of the trends overlap and no clear observations are immediately evident in this plot. In an attempt to extract trends, one could focus on a single electrolyte composition. Consider the four data points at log t = 1. It may be observed that when sodium silicate is increased with a small increment going from 0 (green circle) to 1.35 (red square) mg L^{-1}, there is a drop in the overall δ/L_c ratio. However, further increasing sodium silicate to 2.7 and 5.4 mg L^{-1} does not give rise to a further drop in δ/L_c but rather an increase back to the same value as 0 mg L^{-1}.

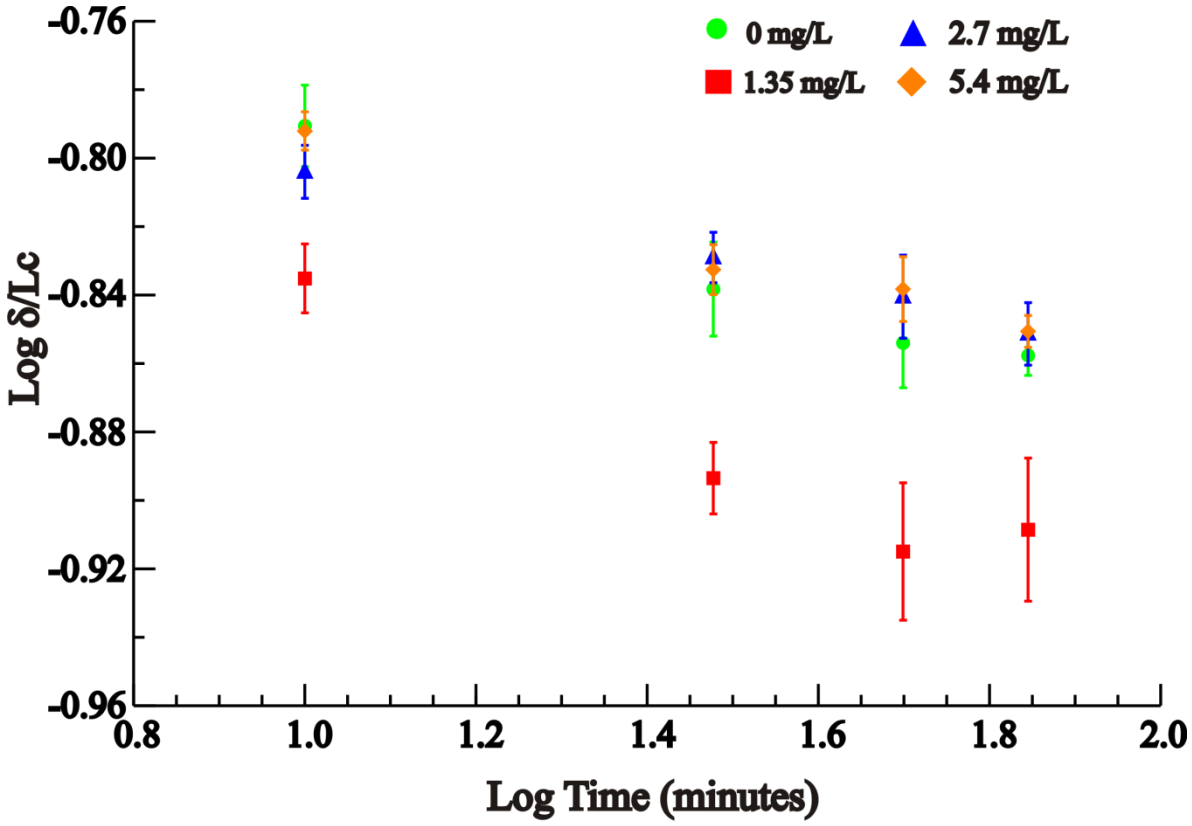

Figure 31 : Averaged log δ/L_c versus log t of zinc samples produced on an aluminum substrate from electrolyte containing 0 (green circle), 1.35 (red square), 2.7 (blue triangle) and 5.4 mg L^{-1} (orange diamond). Error bars represent the standard deviation of 3 images on one sample per deposition condition.

This may indicate that a small amount of sodium silicate reduces the δ/L_c ratio and produces smoother samples. However, any further increase in sodium silicate will make the deposits rougher. The slopes of the trends in Figure 31 provide the optical roughness growth exponent γ and indicate the growth rates of the surface features. Values of γ that are more negative indicate a slower growth rate in δ/L_c. The values of γ were extracted by regression analysis, and γ was then plotted as a function of sodium silicate composition. The results are shown in Figure 32 and while there is some scatter in the data, γ is most

negative at low sodium silicate concentrations. At higher concentrations, the values of γ become less negative (i.e., faster growth rate in roughness per critical length) over the range of data studied.

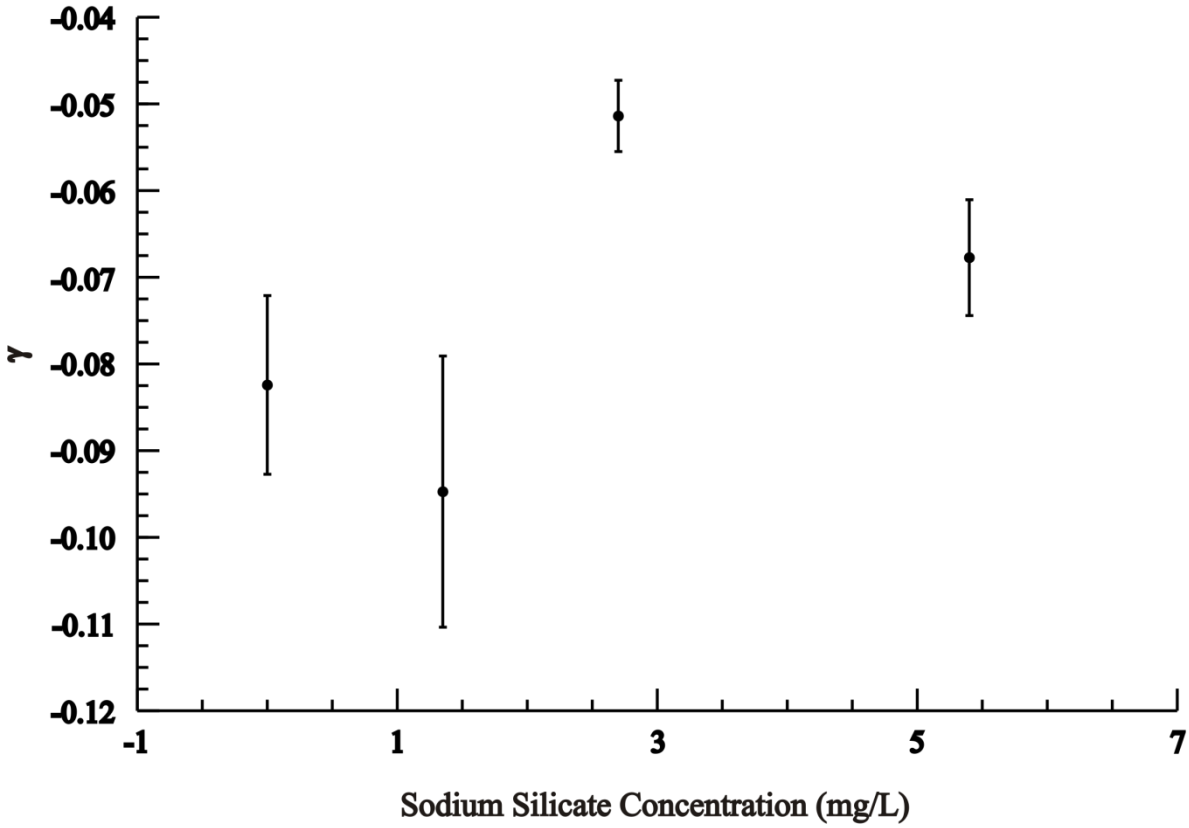

Figure 32 : Analysis of optical roughness exponent (γ) extracted from zinc deposits produced on an aluminum substrate from an electrolyte containing 30 mg L^{-1} glue, 9 mg L^{-1} licorice and sodium silicate ranged between 0 and 5.4 mg L^{-1}. The error bars represents standard error attained from slope analysis using linear regression with error propagation.

These results may indicate that a small amount of sodium silicate will have an impact on making smoother samples by affecting the growth rate of δ/L_c. However, the relative scatter in the data in Figure 32 is not clear evidence of this claim. Moreover, while each sample

was imaged in triplicate the data was not analysed in three independent replicates. Even so, it is possible that the other electrolyte components are masking the influence of sodium silicate. For instance, it was noted in the previous chapter that high glue concentrations (above 30 mg L^{-1}) gave rise to a second static growth exponent (α') in a single scaling plot. This was also noted in the current study for high sodium silicate levels and may indicate that operating near 30 mg L^{-1} glue concentration is on the cusp of two deposition mechanisms, which may pose problems if the other additive concentrations change subtly. This raises an interesting possibility that it is not only the amount of additives that are important but also their relative proportions in the electrolyte. To investigate whether there are more clear trends, a series of studies performed in triplicate/replicate were initiated at lower glue concentration while varying the amount of sodium silicate and licorice. The results are presented in the next section.

5.2 Influence of sodium silicate and licorice with low glue concentration

In this section, zinc samples were electrodeposited for 10, 20, 30 and 50 minutes from the standard electrolyte containing 60 g L^{-1} Zn, 160 g L^{-1} H_2SO_4 and 1 mg L^{-1} glue at a current density of -44 mA cm^{-2} with concentrations of sodium silicate and licorice independently varied. For example, when the influence of sodium silicate is studied, the concentration of sodium silicate is 0, 2, 4 and 15 mg L^{-1} and the concentration of licorice is kept constant at 5 mg L^{-1}. While, when the influence of licorice is studied, sodium silicate is kept constant at 2 mg L^{-1} and the amount of licorice ranged at 0, 5 and 15 mg L^{-1}. Also, the conditions that did not produce a complete deposit (i.e., a zinc layer where holes were visually observed) were not included in these studies. This only happened for 10 minute deposits.

The concentrations and deposition times studied in this section are listed in Table 5 for clarity.

Table 5: Portion of table 4 showing the concentrations of additives studied with deposition time and 50 × 50 μm AFM images that is discussed in this section.

Additive amounts (mgL^{-1})	Deposition times (minutes)
1G_2SS_5L	10*,20,30,50
1G_4SS_5L	10*,20,30,50
1G_15SS_5L	20,30,50
1G_2SS_0L	10,20,30
1G_2SS_15L	10,20,30

These studies were conducted as done in Chapter 4, where three samples were independently produced at each deposition condition and each sample had three AFM images taken on it resulting in a total of 9 data sets to be analyzed through scaling analysis. Furthermore, conditions that resulted in an average scaling profile with two α regions (i.e., a scaling profile with a second linear region with a slope correlation coefficient above 0.992) are not included in the analysis. In fact, this only occurred at a 50 minute deposition time of 1G, 0SS, 5L and this data set is not included in the analysis. Furthermore, the image size was restricted to 50 × 50 μm at 512 × 512 pixels of all of the above studies. These images were analyzed using the truncated scaling program with the binning by 2 at the start, in order to stay consistent with what has been shown so far.

For reference, the scaling profiles for a representative sample (produced from 1G, 2SS and 5L) show the normal behaviour as seen in Figure 33.

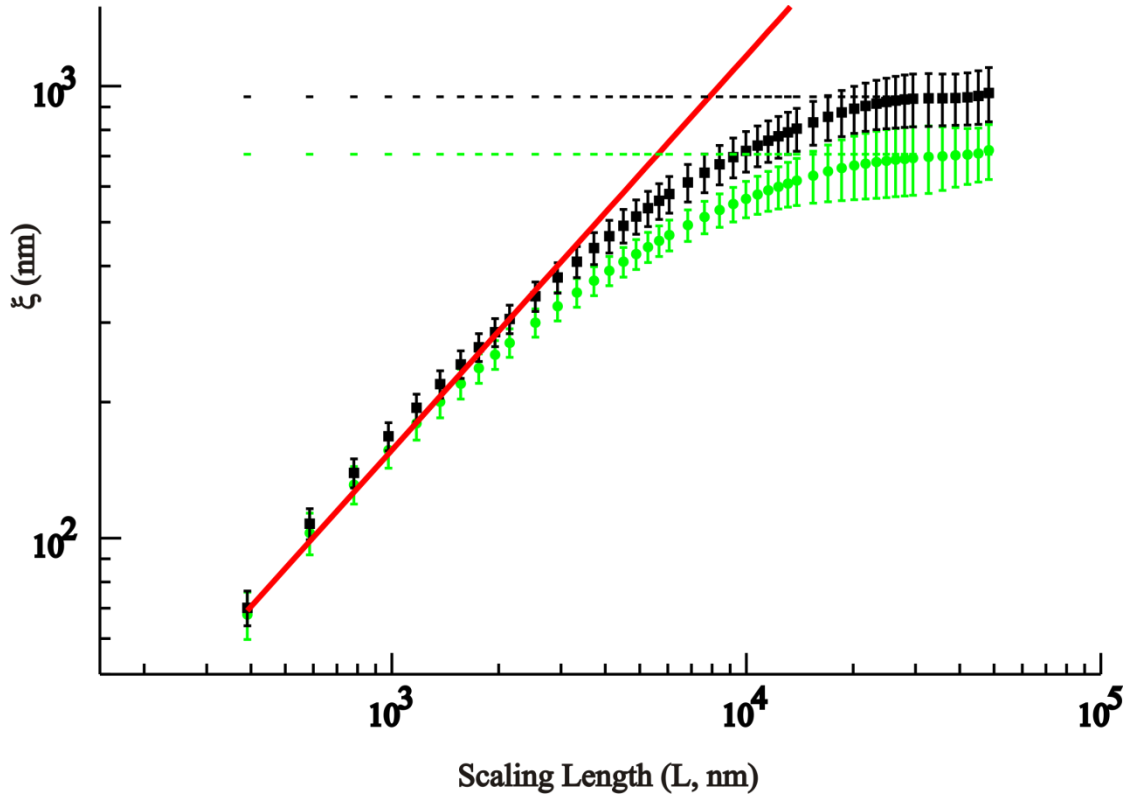

Figure 33: Scaling profiles of 20 (green circle) and 50 minute (black square) zinc sample deposited on an aluminum substrate from electrolyte containing 1 mg L^{-1} glue, 2 mg L^{-1} sodium silicate and 5 mg L^{-1} licorice at a current density of -44 mA cm^{-2}. This plot of log ξ versus log L shows the normal scaling behaviour where at lower scale lengths (L) there is a linear region where the static growth exponent (α, red line) is extracted, followed by a saturated region where the limiting roughness (δ, horizontal dotted lines) is extracted of the zinc deposits at respected deposition times. The error bars represent standard deviation from 9 images over 3 replicates.

Again, α and each of the parameters (δ, L_c and δ/L_c) were extracted in the same manner as described in Chapter 4. This was the standard analysis for zinc deposits produced from each electrolyte composition and while scaling profiles were always obtained, the discussion in this section is limited to trends in δ, L_c and δ/L_c or the respective scaling exponents. Additionally, because a 30 minute deposit is part of every study (see Table 4 and 6), the

description of data begins with this time set. In Figure 34 the values of log δ and log L_c for 30 minute deposits are presented in a bar graph with varied amounts of glue, sodium silicate and licorice.

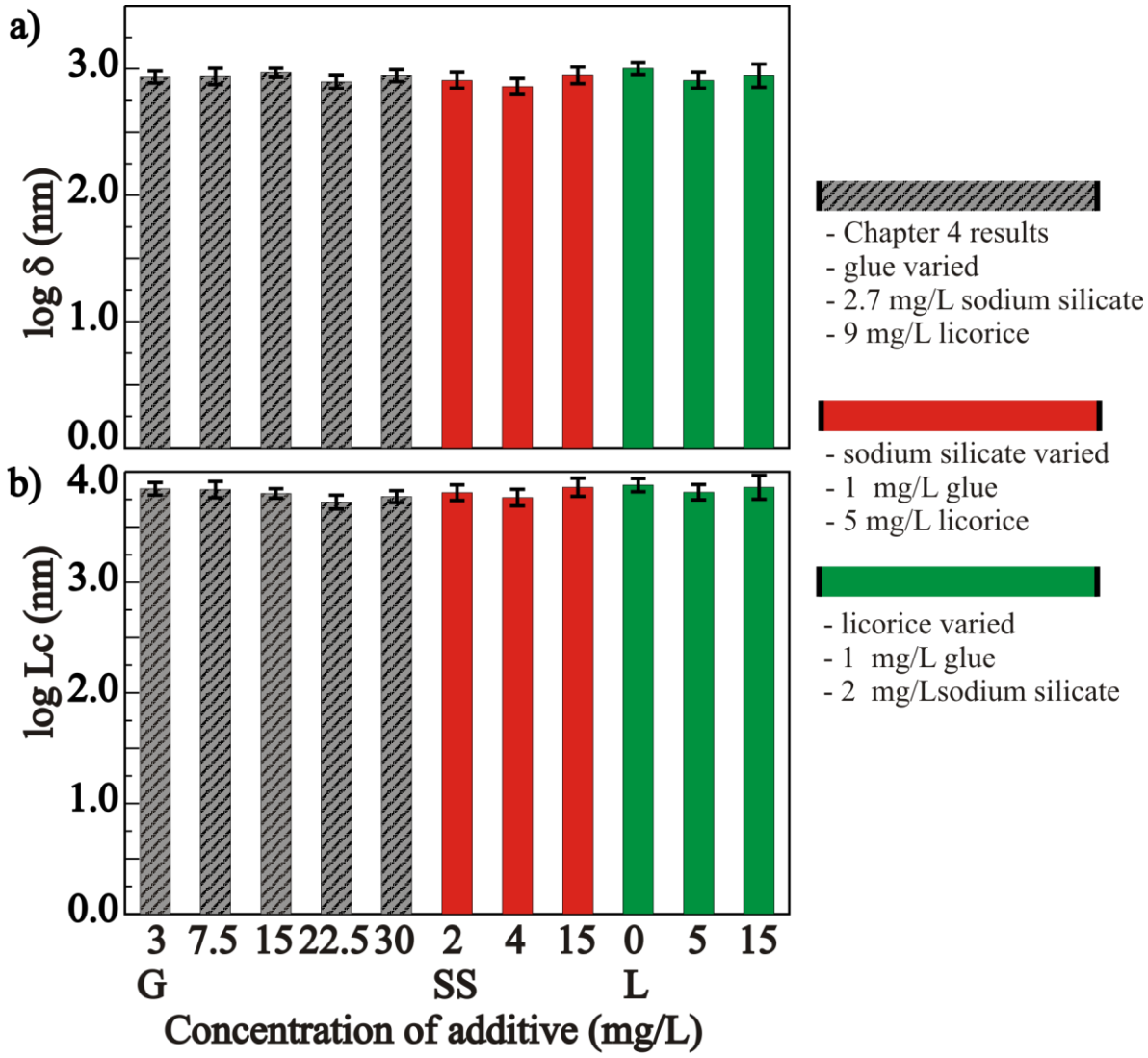

Figure 34: Bar graph showing the data for a) log δ and b) log L_c versus additives: glue, sodium silicate and licorice. This graph shows only the data at 30 minute zinc deposits and the data previously described in Chapter 4 is presented as striped bars. The sodium silicate study is shown as red bars and licorice study shown in green. Data that exhibited two α behaviour is not included. Error bars represent standard deviation in 9 data sets over 3 replicates.

Results that were presented in Chapter 4 (i.e., insets of Figure 27) are also included in Figure 34 (plotted as log L_c) and shown as striped bars. From Figure 34 a) and b) there are no clear trends that can be immediately drawn in both limiting roughness, δ, and critical length, L_c, as the error bars overlap. However, when the ratio log δ/L_c versus additive is plotted trends start to become apparent. Figure 35 is a bar plot of log δ/L_c versus additive.

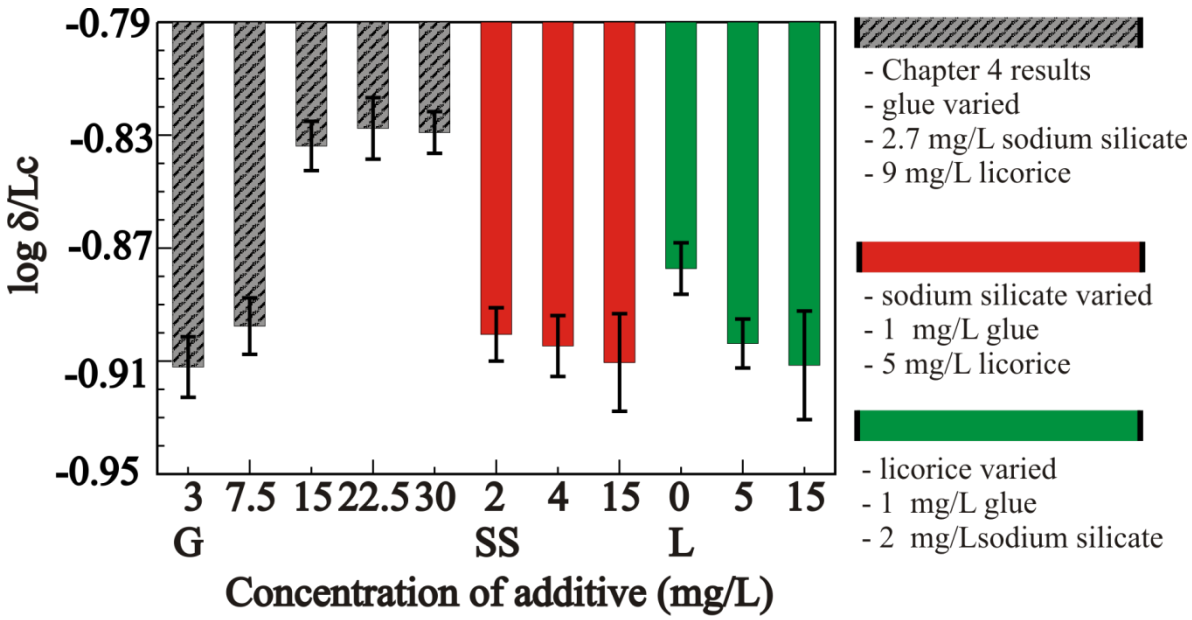

Figure 35: Bar plot of log δ/L_c versus amount of additives: glue, sodium silicate and licorice, varied. This plot only shows the data obtained at 30 minute deposit and data previously described in Chapter 4 is presented as striped bars. The sodium silicate study is shown as red bars and licorice study shown in green. Data that exhibited two α behaviour is not included. Error bars represent standard deviation in 9 data sets over 3 replicates.

As seen in the stripped bars of Figure 35, and as previously described in Chapter 4, as the amount of glue is increased (while sodium silicate and licorice are kept constant) it results in increasing values of δ/L_c. However, as shown in the red bars of Figure 35, at low and constant levels of glue and licorice, an increase in sodium silicate shows little influence on

δ/L_c except for an increased variability. This indicates that the roughness per period becomes less reproducible. Furthermore, in the green bars of Figure 35, when there is 0 mg L^{-1} licorice in the electrolyte the δ/L_c ratio is more positive (i.e., rougher) than when licorice level is increased to 5 mg L^{-1}. However, further increasing the licorice levels produces samples that have similar δ/L_c values to that of samples produced with electrolyte containing 5 mg L^{-1} licorice. This result may indicate that a small amount of licorice might act to produce morphologies with lower limiting roughness per periodicity. However, this may only be observed since the glue level is now considerably lower than other studies. In fact, it is difficult to extract any patterns when 3 variables (G, SS and L) are changing. Trends may become clear if the data is presented as a scatter of values above and below the median value. This can then be converted to a ternary diagram where each data point on the graph represents relative percent of each additive. Table 6 shows a list of all studies that were performed in triplicate and replicate (9 data sets - including studies that showed 2 α character) with the amounts of additive in mg L^{-1} and their relative percentage.

Table 6: Studies with 9 data sets presented in Chapters 4 and 5 with their concentration in mg L^{-1} and their relative percent composition.

Glue (mg L^{-1})	Sodium silicate (mg L^{-1})	Licorice (mg L^{-1})	% Glue	% Sodium silicate	% Licorice
3	2.7	9	20.4	18.4	61.2
7.5	2.7	9	39.1	14.1	46.9
15	2.7	9	56.2	10.1	33.7
22.5	2.7	9	65.8	7.9	26.3
30	2.7	9	71.9	6.5	21.6
1	2	5	12.5	25.0	62.5
1	4	5	10.0	40.0	50.0
1	15	5	4.8	71.4	23.8
1	2	0	33.3	66.7	0.0
1	2	15	5.6	11.1	83.3
Data with two α					
Glue (mg L^{-1})	**Sodium silicate (mg L^{-1})**	**Licorice (mg L^{-1})**	**% Glue**	**% Sodium silicate**	**% Licorice**
1	0	5	16.7	0.0	83.3
30	13.5	9	57.1	25.7	17.1
30	27	9	45.5	40.9	13.6
37.5	2.7	9	76.2	5.5	18.3
60	2.7	9	83.7	3.8	12.6

The data in Table 6 is presented as a ternary diagram in Figure 36. A ternary diagram has three axes where each represents the relative percent composition of each additive between 0 and 100%. To read the composition of each data point, a line is drawn from each axis to a point where they intersect. This is demonstrated in Figure 36 by three dotted lines that intersect for the electrolyte condition that has 1 mg L^{-1} glue, 4 mg L^{-1} sodium silicate and 5 mg L^{-1} licorice (shown in parenthesis) with a relative percentage of 10, 40 and 50 %, respectively.

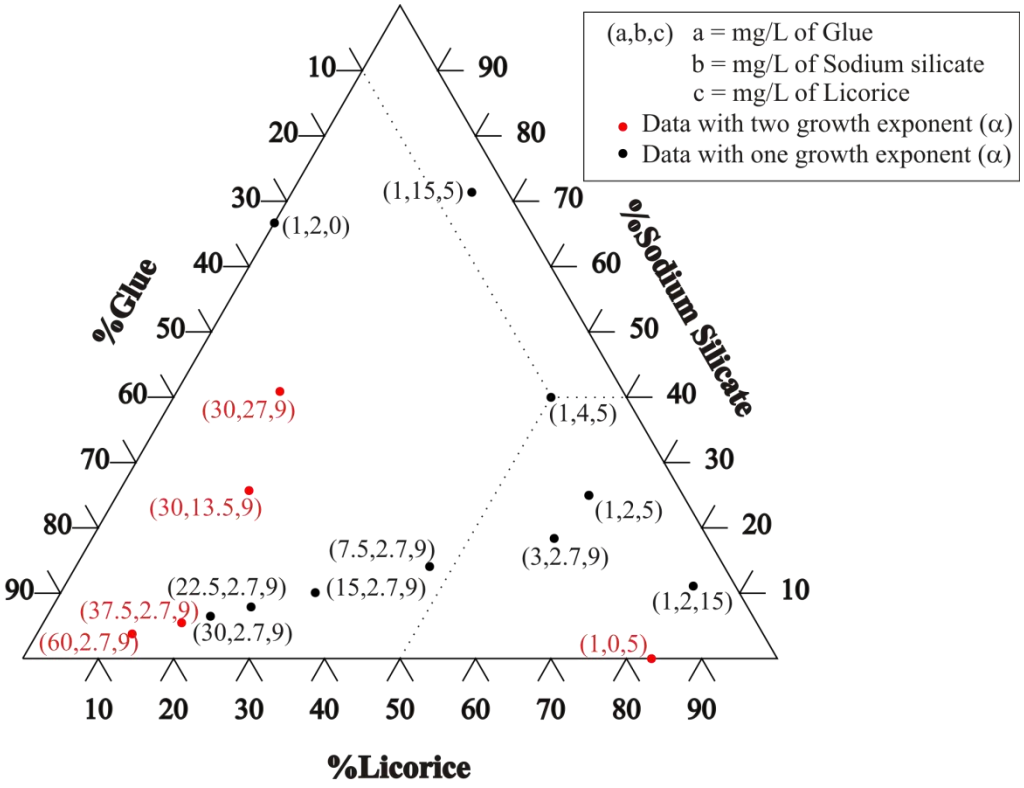

Figure 36: Ternary diagram showing experiments with both concentrations of additives in mg L^{-1} and their relative percent composition. As the legend suggests, in brackets next to the symbols are concentrations of each additive in mg L^{-1}. The percent of each component is represented on the axes. Red data points are electrolyte conditions that produced scaling plots with two-α behaviour. In order to read a data point, three lines are drawn from each axis to the point where they intersect. The dotted line is for the electrolyte condition that has 1 mg L^{-1} glue, 4 mg L^{-1} sodium silicate and 5 mg L^{-1} licorice with a relative percentage of 10, 40 and 50 %, respectively.

This diagram is presented to show the list of all of the studies conducted in triplicate that have been presented in the thesis thus far. However, it states nothing about the roughness parameters that have been extracted. This approach is described in the next section but only for data that did not show two-α character.

5.3 A comparative study using ternary diagrams

Ternary diagrams will be used to present the combined results of scaling analysis that have been performed on zinc electrodeposits with respect to the relative composition of each additive in the electrolyte. This approach allows a comparison of relative composition rather than focusing on each additive independently and provides a much better understanding of the overall system. These ternary diagrams will be used to show trends for δ, L_c and δ/L_c for 30 minute deposits, as well as scaling exponents β, β/α and γ. Because the scaling exponents were only obtained from data that showed single-α character, the ternary diagrams are limited to the data sets with a single growth exponent α. The ternary diagrams will show if the scaling parameter is either above or below a median value. For example, consider the scatter plot shown in Figure 37 that represents all the values of δ/L_c and their standard deviation versus concentration of the 3 additives (G,SS,L) obtained from the 30 minute deposits. Also, on Figure 37 a red dotted line shows the median value, which is used to distinguish between the data points that are above or below.

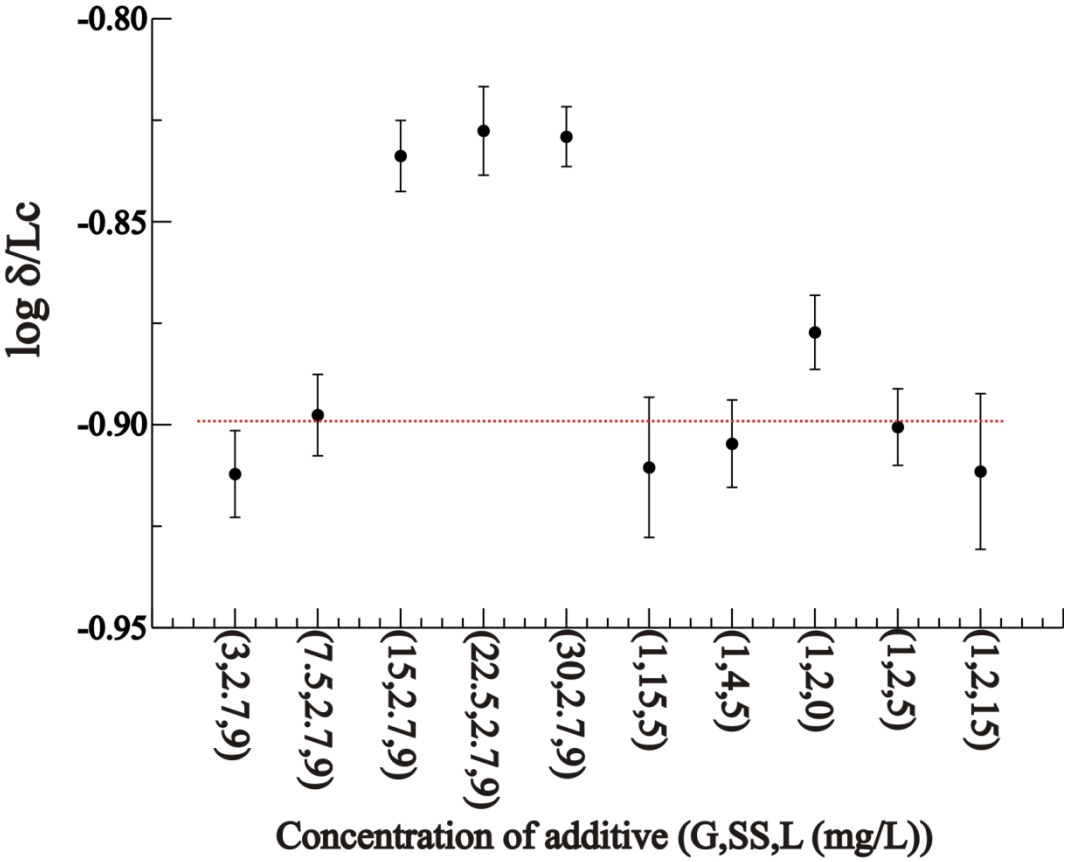

Figure 37: Scatter plot of log δ/L_c versus concentration of additives in mg L^{-1} showing a red dotted line for the median value of log δ/L_c = -0.8991. Error bars represent the standard deviation from the average of 9 data sets collected from 30 minute deposit.

For example, in Figure 37, experiments that have 15, 22.5 and 30 mg L^{-1} glue and 2.7 and 9 mgL^{-1} sodium silicate and licorice respectively, have average log δ/L_c and standard deviation values that are above the median value whereas, experiment with 3G, 2.7SS and 9L has an average log δ/L_c and standard deviation below the median value. Experiment 7.5G, 2.7SS, 9L, shows an average value above the median but the standard deviation cross it. If a data point is above the median value it, will be represented with a circle on the ternary diagram; if it is below the median value, it will be represented with a square

symbol. Additionally, closed symbols are used if the standard deviation is outside the median value. With this approach, the data is plotted on a ternary diagram, and a trend is more clear. Figure 38 is the ternary diagram representing the data points presented in Figure 37, but now organized to indicate if they are above or below the median value.

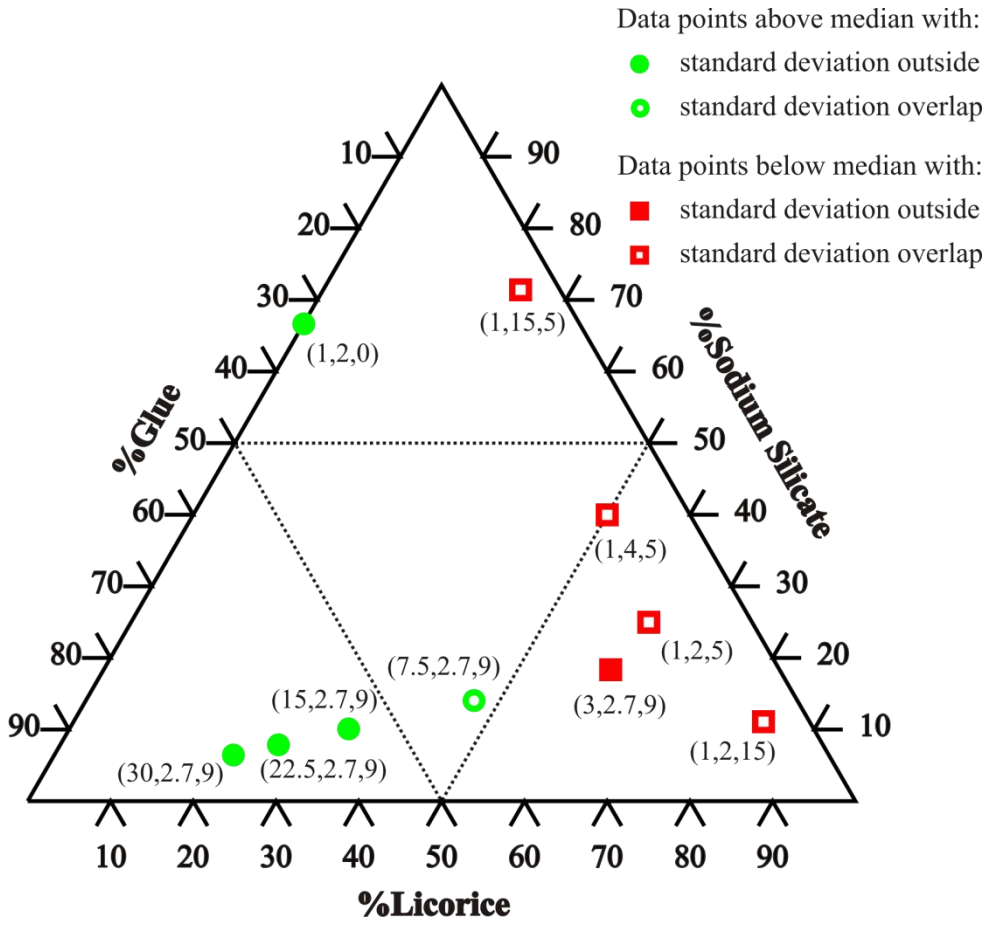

Figure 38: Ternary diagram of log δL_c values of 30 minute zinc deposits versus relative percent composition of each additive. Solid green circle represent conditions that result in values of log δL_c and their standard deviation above the overall median value. Open green circles show conditions that are above the overall median value but their standard deviation overlaps the median. Solid red square represents data points and their standard deviation below the overall median value. Open red square symbolizes data points below the median with standard deviation overlap. Median value of log δL_c = -0.8991. Note: the results shown on this ternary plot were obtained with the concentration ranges shown in parentheses near each data point (in mg/L) and may not necessarily extend to systems with a different concentration range.

On inspection of Figure 38, there is a clear divide between additive conditions that result in log δ/L_c values below (red squares) and above (green circles) the median value. The ternary diagram can now be used to make statements on the influence of the combination of additives. Recall that δ/L_c indicates the roughness to periodicity ratio of the surface features. When the electrolyte contains less than 30% glue and more than 60% licorice, then a wide range of sodium silicate can be used to produce morphologies with δ/L_c values that are lower than the overall median (at least for the 30 minute data shown in Figure 38). Under these conditions, the 30 minute deposits have a lower roughness over a given period of the surface. This is an interesting trend and we note that while most of the data points that are above the median value contain large quantities of glue, there is at least one case where the amount of glue is very low (1,2,0). This data set had an average δ/L_c that was above the median value, while a system with a similar glue and sodium silicate composition (1,2,15) was below. In this regard, it appears that it is the relative percentage of additives influence the morphology of zinc electrodeposits. However, in order to present a wider analysis, the gaps in the ternary diagram should be filled in by completing more experiments. Additional data points will in turn adjust the median values and give a more clear picture. In the next chapter, more experiments were conducted to complete the ternary diagram of δ/L_c, as well as those for roughness exponents α and γ and current efficiencies.

Chapter 6: Influence of Relative Percentage of Additive on Roughness Parameters and Current Efficiency Shown on Ternary Diagrams

In addition to the experiments presented in Chapters 4 and 5, twelve other experiments were initiated in efforts to produce a more complete ternary diagram that shows the influence of additives on current efficiency and roughness parameters such as δ/L_c and γ. Each of these studies was performed over a range of deposition times. However, due to time constraints, these additional studies were not completed in three replicates but rather from one sample per deposition time with three AFM images on each. Of the twelve additional experiments four of them showed two-α character and two studies showed poor fits (presumably from incomplete zinc deposition at the lower time scale – see appendix C for studies not included in the ternary diagrams). This leaves six additional studies to include in the ternary diagrams. All studies are shown in Table 7. Those marked with an asterisk indicate that they were produced from three images on one trial. While, other scaling parameters (δ and L_c) and scaling exponents (β and β/α) have also been plotted on a ternary diagram, they are presented only in the Appendix.

The additive concentration, deposition time and number of AFM images per study included in this chapter are shown in Table 7.

Table 7 : Additive concentrations and deposition time studies that do not include two growth mechanisms and poor fit data.

Additive concentrations studied (mg/L)	Deposition times (minutes)	Number of AFM images/deposition time
2.5G_3.5SS_4L*	10, 20, 30	3
6G_50SS_9L*	10, 30, 50	3
15G_38SS_9L*	10, 30, 50	3
22.5G_25SS_9L*	10, 30, 50	3
6G_5.4SS_9L*	10, 30, 50	3
15G_13.5SS_9L*	10, 30, 50	3
30G_0SS_9L*	10, 30, 50, 70	3
30G_1.35SS_9L*	10, 30, 50, 70	3
30G_5.4SS_9L*	10, 30, 50, 70	3
1G_2SS_5L	20,30,50	9
1G_4SS_5L	20,30,50	9
1G_15SS_5L	20,30,50	9
1G_2SS_0L	10,20,30	9
1G_2SS_15L	10,20,30	9
3G_2.7SS_9L-	30	9
7.5G_2.7SS_9L-	30	9
15G_2.7SS_9L-	30	9
22.5G_2.7SS_9L-	30	9
30G_2.7SS_9L	10, 30, 50, 70, 90	9

* studies with three images per deposition time
- only 30 minute deposits

In Figure 39, all additive conditions studied are presented to show the spread of data over the ternary diagram. Some of these data points are only of single time study from which we cannot extract β, β/α or γ but we can still extract δ, L_c and δ/L_c. These are marked by a minus symbol in the table. However, they are replicate data and are still useful in observing the influence of additive combination on roughness characteristics.

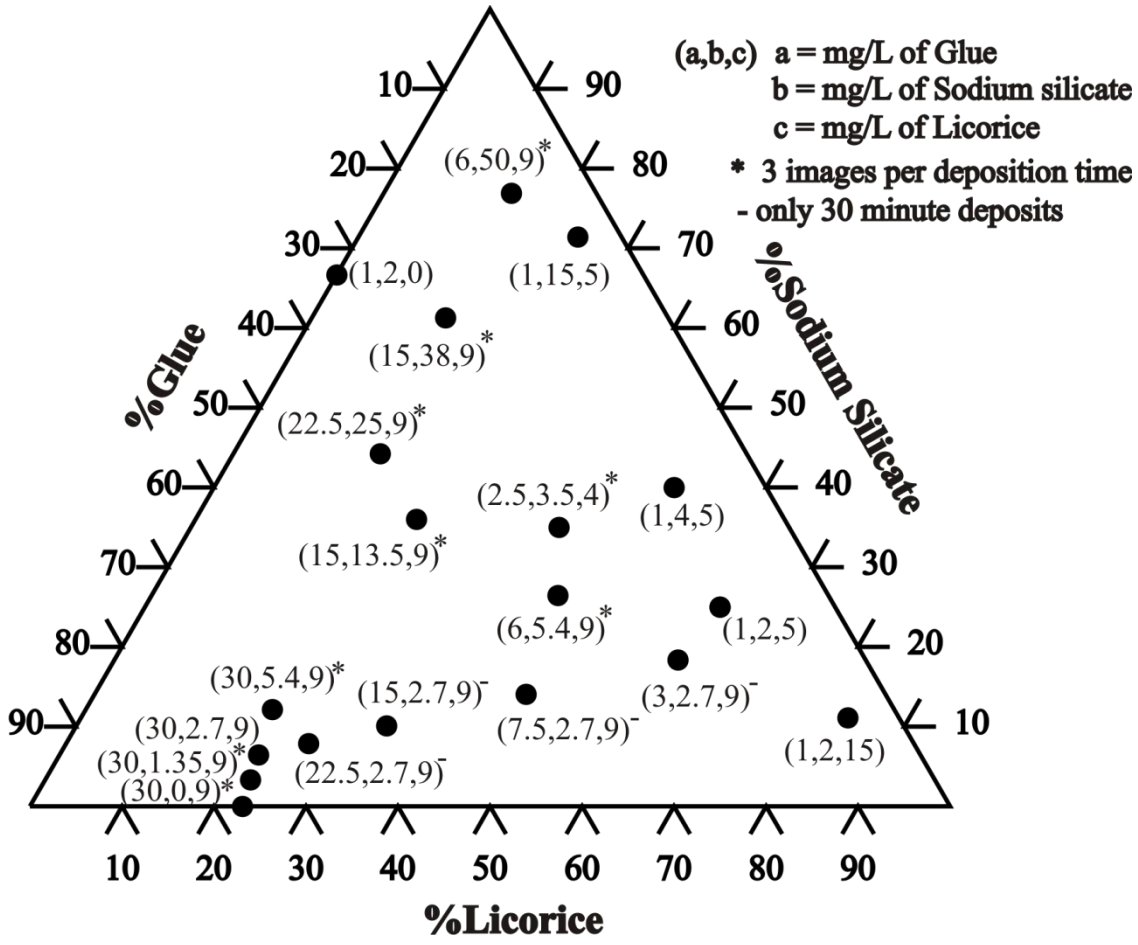

Figure 39: Ternary diagram showing the spread of experiment conditions. Each data point has the amount of each additive in mg L^{-1} inside the brackets. The 9 experiments with 3 images per deposition time are marked with an asterisks and electrolyte conditions that were only studied at 30 minute depositions and are marked by a minus symbol.

The extraction of roughness characteristics δ, L_c and δ/L_c, as well as all growth exponents such as α, β, β/α and γ, were obtained as before by linear regression. The median value was used to distinguish whether the average value was above or below the overall median value for each parameter. These differences are then plotted in the same manner as shown in the end of the last chapter. Briefly, circles symbolize data points that are above the median and

squares are for data that are below the median. Also, open symbols mean that the error bars overlap the median value. Lastly, data points that are the same as the median value are indicated by a open black star symbol. Furthermore, presenting data in this manner will enable the ability to discuss generalized trends for influence of relative amount of additives versus roughness characteristics. For example, the ternary diagram shown in Figure 40 is divided into four parts, each of these parts represents an area with relative amounts of the three additives.

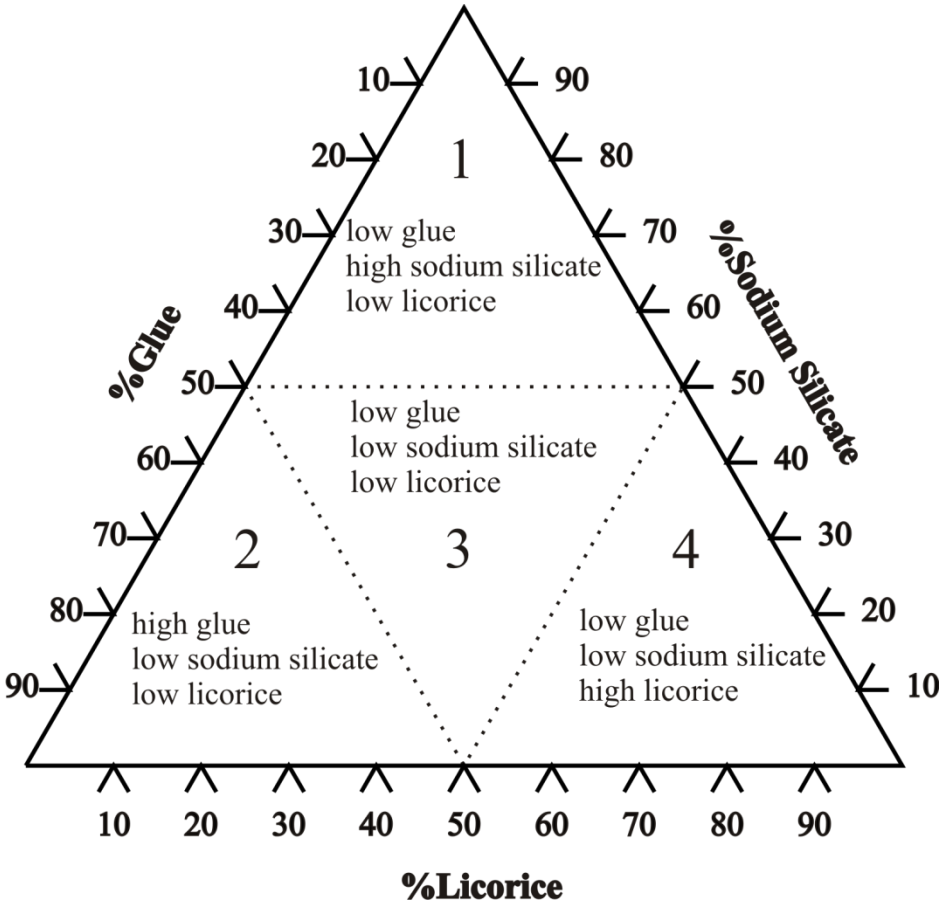

Figure 40: Ternary diagram divided into 4 sections which are labeled with relative amounts of each of the three additives.

As such, the ternary plot can now be seen to have one area where each additive is independently high (i.e., above 50%) and three areas where they are low (below 50%). This setup is useful to visualize the areas that are common in relative levels of each additive. For example, in Figure 40, it can be seen that sections 1, 3 and 4 have low glue in common. Whereas zones 2, 3 and 4 have low sodium silicate levels in common. Lastly, low licorice is common in regions 1, 2 and 3.

One of the most important parameter to the zinc electrowinning industry is the current efficiency (CE) of each electrolyte set. This was determined, as explained in the experimental section, and averaged over all times studied. In the following section this, data is presented on a ternary diagram showing values above and below the median CE.

6.1 Ternary diagram: Current efficiency

The current efficiency for each deposit was calculated and averaged over all deposition times and the standard deviation was obtained. In Figure 41, the average current efficiency is plotted on a ternary diagram.

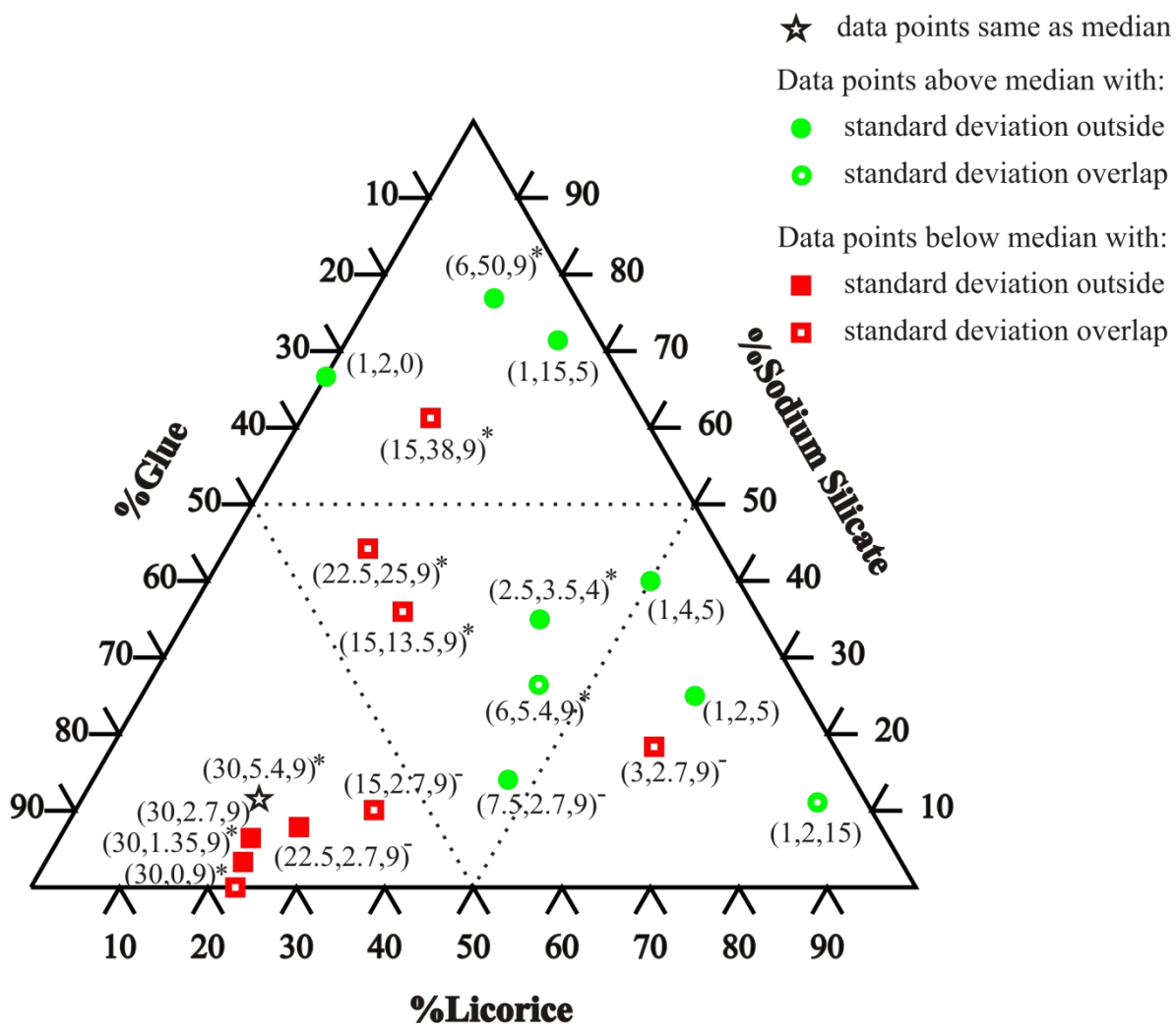

Figure 41: Ternary diagram showing the impact of relative amounts of additive on percent current efficiencies (% CE). As shown in the legend, the condition that resulted in %CE that was the same as the overall median value is symbolized by an open black star. Data points that were above the median value are indicated by the green circle and below are shown by a red square. Data points that had standard deviations outside the median are shown as solid symbols and data points with standard deviation overlapping the median value are shown as open symbols. Median % CE value = 84.60. Note: the results shown on this ternary plot were obtained with the concentration ranges shown in parentheses near each data point (in mg/L) and may not necessarily extend to systems with a different concentration range.

The ternary diagram demonstrates a clear trend for the current efficiency. The CE is generally above the median value in sections 1, 3 and 4 or when glue levels are less than

40% (low), while licorice levels are above 40% (intermediate to high) and over a wide % sodium silicate. Furthermore, when glue levels are above 40% the values of % CE are reduced below the median value. It seems that the highest current efficiencies are obtained when the glue level is below 40%. However, when studying the actual concentrations in parenthesis, the highest % CE were obtained for electrolyte compositions where glue did not exceed 7.5 mg/L.

While % CE is one of the main concerns of an operating cell house, it is not the only one. It is also important to produce uniform and levelled deposits that are easily removable from the substrate. In the next sections, these aspects are investigated using ternary diagrams.

6.2 Ternary diagram: Static exponent α

The static exponent, α, in addition to providing information on deposition mechanism, can also be used to make a statement on the relative uniformity of the deposit. Mechanistic aspects of additives have been discussed in the Chapters 4 and 5. Here, it will be used to comment on relative uniformity of deposits under various additive combinations for 30 minute deposits. As a reminder, values of α are between 0 and 1, where 0 indicates random morphology and 1 means that deposit morphology is uniform. As such, conditions that produce α values above the overall median value indicate more uniform deposits. It should be noted that α values in this thesis never reached a point below 0.78. Figure 42 is a ternary diagram showing the influence of additive conditions on α.

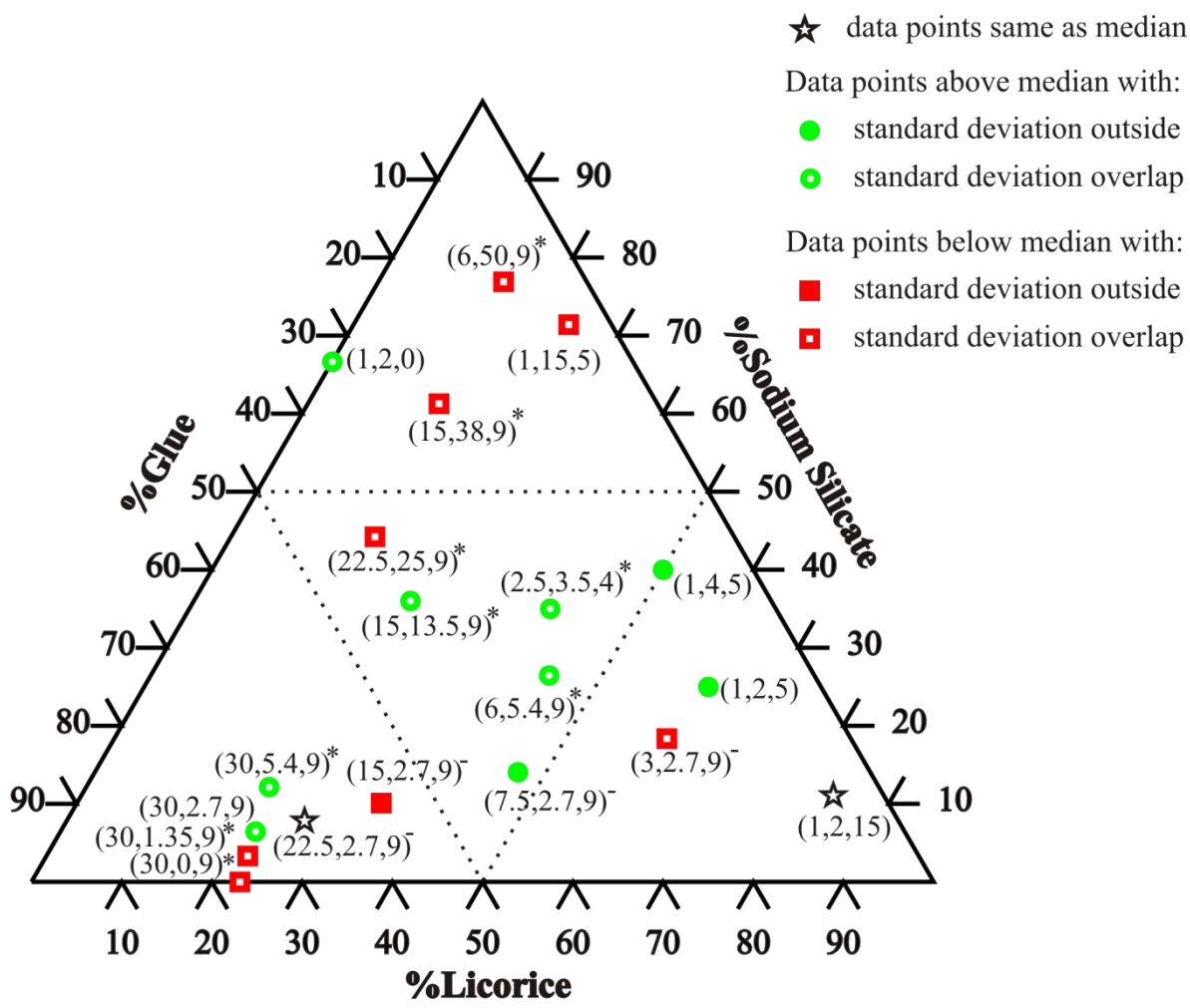

Figure 42: Ternary diagram showing static exponent α relative to overall median value (open black stars) of deposits produced from electrolytes containing additives with various relative percent compositions. Data points that were above the median value are indicated by the green circles and below are shown in red squares. Data points that had standard deviation outside the median are shown as solid symbols and data points with standard deviation overlapping the median value are shown as open symbols. Median α value = 0.82. Note: the results shown on this ternary plot were obtained with the concentration ranges shown in parentheses near each data point (in mg/L) and may not necessarily extend to systems with a different concentration range.

From Figure 42, it can be seen that there is an operating regime that will produce deposits with α values above the median. This regime is most consistent in sections 3 and to some extent section 4 that correspond to low glue, low sodium silicate and low licorice (section

3) or low glue, low sodium silicate and large licorice levels (section 4). At least within the conditions of our study, the ideal regime with uniformity above the median is when glue levels are around 10% (but not greater than 20%), and when sodium silicate level is 20 to 40% and licorice is 40 to 60%.

It is also important to understand how the relative concentration of additives can influence the grain size of deposits. This information can be obtained from looking at the ratio of roughness per periodicity (δ/L_c) and its rate of change (γ). Inspecting these two parameters will provide insight on how the roughness is spread out over a given period on the surface. and The optical roughness exponent will give an idea how it will change with time. These two parameters are evaluated in the next section.

6.3 Ternary diagram: Roughness per periodicity and its rate of change

In this section, an analysis of roughness per periodicity (δ/L_c) of surface morphology produced from additive combinations shown in Table 7 and over a 30 minute deposition is presented in a ternary diagram. This time was chosen because all experiments included this deposition time. While other roughness parameters are important, they show trends only in one aspect of roughness characteristic at a time (i.e., δ shows only limiting roughness), whereas δ/L_c allows for analysis of two aspects of growth on one plot (i.e., limiting roughness per periodic feature). Also, lower values of δ/L_c (or more negative values of log δ/L_c) indicate a morphology that has larger L_c compared to low values of δ, that is, a smoother surface. The results of the δ/L_c was treated in the same manner as done previously and plotted in a ternary diagram in Figure 43.

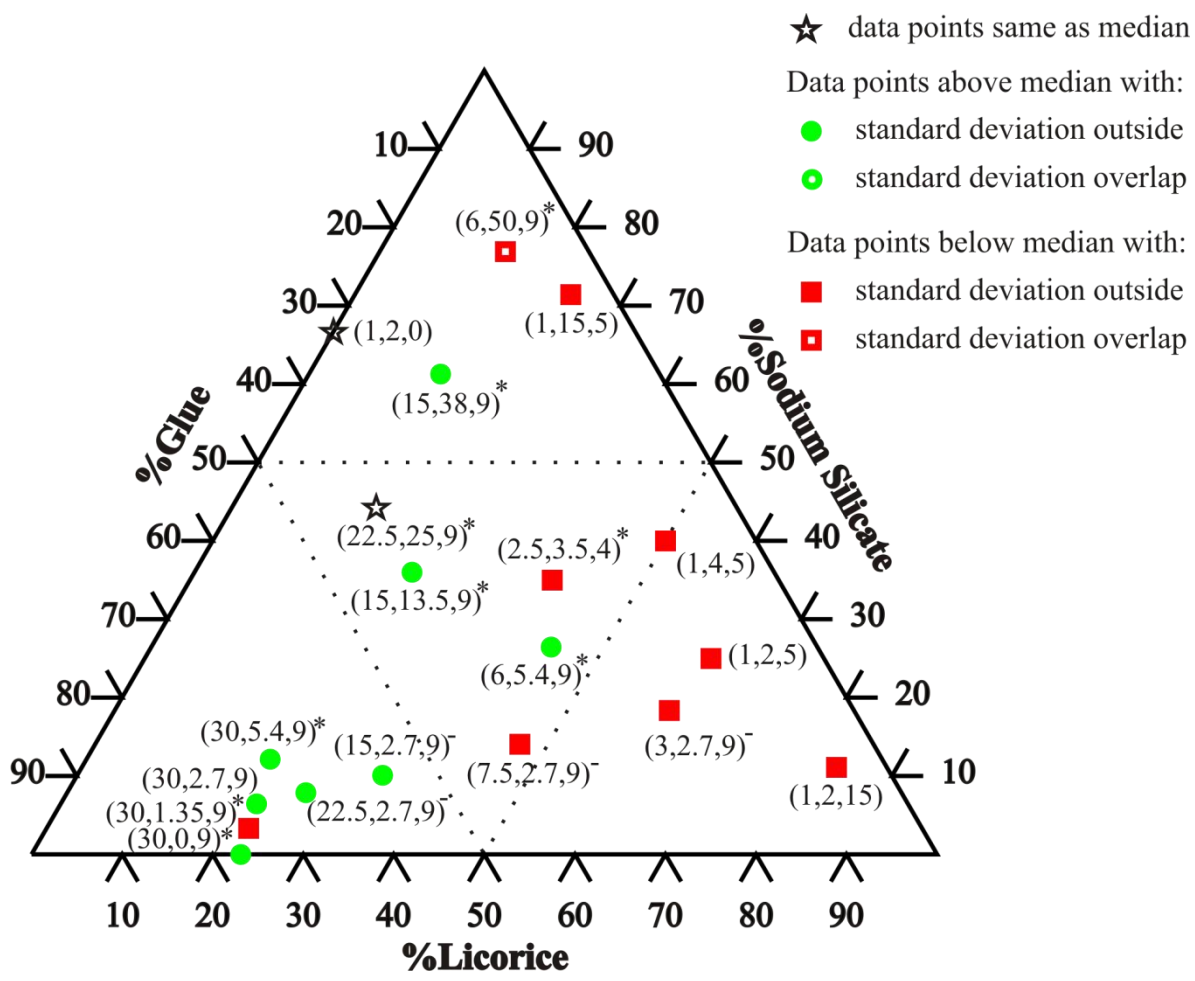

Figure 43 : Ternary diagram showing the values of log δ/L_c relative to overall median value (open black star) of 30 minute deposits produced from electrolytes containing additives with various relative percent compositions. Data points that were above the median value are indicated by the green circle and below are shown in red squared. Data points that had standard deviation outside the median are shown as solid symbols and data points with standard deviation overlapping the median value are shown as open symbols. Median log δ/L_c value = -0.88. Note: the results shown on this ternary plot were obtained with the concentration ranges shown in parentheses near each data point (in mg/L) and may not necessarily extend to systems with a different concentration range.

From the ternary plot in Figure 43, it can be seen that the conditions that produce deposits with δ/L_c values and their standard deviation that are below and outside the median point

are mostly present in section 4 when there is low glue, low sodium silicate, and intermediate to high licorice levels.

It is emphasized that the values in Figure 43 are a snapshot for 30 minute samples only and this may change with deposition time. The rate of change of δ/L_c with time is determined from the optical roughness exponent γ. The value of γ is extracted from the slope of the linear trend on a log δ/L_c versus log deposition time plot. A more negative value of γ indicates that with deposition time L_c is growing more rapidly than δ, thereby producing smoother surfaces over prolonged deposition. Again, the data was treated in the same manner as previously shown and is presented in a ternary diagram shown in Figure 44. Here, some data points that were shown in other figures are missing because additional time series above 30 minutes were not available for those samples and are required in order to extract γ.

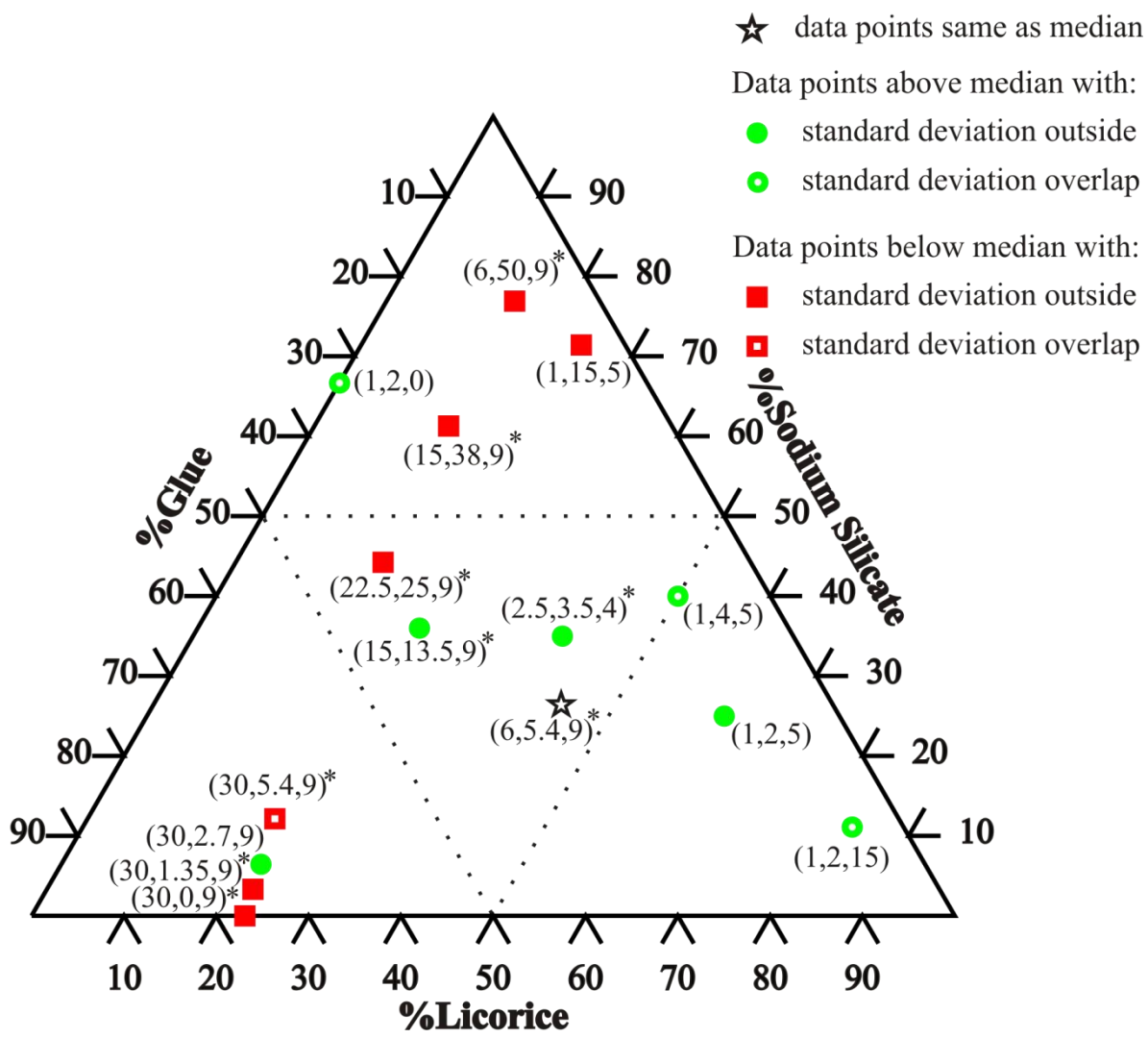

Figure 44: Ternary diagram showing γ (rate of change of δL_c) relative to overall median value (open black star) of deposits produced from electrolytes containing additives with various relative percent compositions. Data points that were above the median value are indicated by the green circle and below are shown in red squares. Data points that had standard deviation outside the median are shown as solid symbols and data points with standard deviation overlapping the median value are shown as open symbols. Median γ value = -0.06. Note: the results shown on this ternary plot were obtained with the concentration ranges shown in parentheses near each data point (in mg/L) and may not necessarily extend to systems with a different concentration range.

From these results, it can be seen that when glue and sodium silicate are low while licorice is intermediate to high (sections 3 and 4), the value of γ is above, or more positive than the median value. This indicates that δ is growing faster than L_c and will produce rougher surfaces over a prolonged deposition time. The importance of this result is realized when comparing it with section 4 in Figure 43 that showed the smoothest surface features (i.e., the lowest δ/L_c at 30 minutes). Therefore, those 30 minute deposits, although smoother on average, are growing with a rate that will produce rougher surfaces with prolonged deposition time. In contrast, from Figure 44 it is clear that section 1 produces deposits with a slower growth rate since the γ values, and their standard error, is generally below or more negative than the overall median. This result seems to indicate that γ values are dependent on the relative licorice concentration. This may be related to a change in electrolyte viscosity leading to a change in surface tension at the electrode/electrolyte interface. It is well known that licorice (as described in the introduction) is a surfactant used as acid mist suppressant in the electrowinning cell houses and as such may be influencing γ.

Ternary diagrams showing the results of δ, β, L_c and β/α are presented in the Appendix D.

In summary, scaling analysis in combination with ternary diagrams were used to demonstrate the influence of relative % composition of the three additives (glue, sodium silicate and licorice) on current efficiency, value of δ/L_c over a 30 minute deposition time and γ. The results show that low glue, low sodium silicate and large licorice levels (i.e., section 4) will produce samples with large CE and α values and smooth 30 minute deposits (indicated by the low δ/L_c values). However, the growth exponent (γ) indicates that these

surfaces may become rougher than other samples over prolonged deposition times. In contrast, electrolytes with low glue, high sodium silicate and low licorice levels (i.e., section 1) will produce samples with large CE, low α values and rougher 30 minute deposits (indicated by the larger δ/L_c values), However, the growth exponent (γ) indicates that these surfaces may be smoother than other samples over prolonged deposition times.

It should be noted that while trends are shown in these ternary diagrams, these studies need to be completed in replicates to get more accurate conclusion.

Chapter 7: Conclusions and Future Studies

7.1: Imaging techniques

SEM and AFM imaging was used to capture high-resolution images of zinc electrodeposits. The SEM images obtained from our samples were in good comparison to those of zinc deposited under similar condition in literature. Furthermore, AFM and SEM images of the same samples compared well, indicating that the AFM probe tip does not influence the morphology of the zinc images captured. In future, studies the results could be verified and validated using optical profilometery. The application of optical profilometery might be beneficial to obtain larger image sizes, which would provide in turn better conclusions on growth morphology.

7.2: Influence of deposition time on roughness characteristics

The influence of deposition on roughness characteristics were investigated using AFM images of zinc samples electrodeposited for 10, 30, 50, 70 and 90 minutes. The results that

were visually observed from the AFM images were confirmed and quantified using scaling analysis. It was found that with an increase in deposition time, the surface features grew both in height and width. This result is in-line with what one would expect because as deposition time increases so does the amount of deposited material. Additionally, a static growth exponent ($\alpha = 0.86 \pm 0.04$) indicated that a self-affine surface with a growth mechanism dominated by surface diffusion is produced when deposition is performed using electrolyte containing additive levels of 30 mg L^{-1} glue, 2.7 mg L^{-1} sodium silicate and 9 mg L^{-1} licorice. Moreover, the rate of change in zinc grain widths ($\alpha/\beta = 0.374 \pm 0.030$) occurred faster than growth in height ($\beta = 0.323 \pm 0.026$), indicating surface features are growing wider faster rather than taller.

In future studies, it would be beneficial to be able to confirm the predictive ability of scaling analysis on zinc electrodeposits. This could be done by performing a 24 and 48 hour deposit and imaging these samples using optical profilometery and applying scaling analysis to see if the growth exponents β and β/α and γ of shorter depositions (minutes in length) would indeed predict the limiting roughness (δ) and critical length (L_c) observed at prolonged deposition times, as observed in the literature for copper electrodeposits [70].

7.3: Influence of glue concentration

Glue concentrations of 3, 7.5, 15, 22.5, 37.5 and 60 mg L^{-1} were used to produce 30 minute zinc samples. These samples were imaged using SEM and AFM. The two imaging techniques compared well. Also, SEM and AFM images showed that as glue concentration was increased, the surface features decreased in width. Furthermore, at high glue

concentrations a new type of morphology consisting of larger underlying features with small features on top of them were identified in both imaging techniques. These results were further confirmed and quantified using scaling analysis from the data collected by AFM. The analysis showed that under glue concentrations between 3 and 30 mg L^{-1}, the dominating growth mechanism was surface diffusion leading to smaller width size of features with higher aspect ratios as glue concentration increased. Additionally, a second or competing static growth exponent ($\alpha' = 0.500 \pm 0.001$ at 60 mg L^{-1}) was quantified at the higher glue concentrations that result in the new type of morphology indicating that, at the extreme glue concentration, a bulk diffusion or progressive nucleation is competing with the surface diffusion mechanism resulting in two distinct morphologies on one surface. Furthermore, the roughness characteristics (δ, L_c and δ/L_c) of all deposition conditions were quantified.

7.4: Influence of sodium silicate and licorice

Sodium silicate levels between 0 and 27 mg L^{-1} in an electrolyte containing 30 mg L^{-1} glue and 9 mg L^{-1} licorice were investigated by performing electrodeposition to produce zinc samples with deposition times of 10, 30, 50 and 70 minutes. These samples were imaged using AFM, followed by scaling analysis. The results show that when there is a small increase in sodium silicate concentration (0 to 1.35 mg L^{-1}), there is a decrease in δ/L_c over all deposition times. However, further increase in sodium silicate amount in the electrolyte did not show this trend. This result led the investigation to analyze zinc samples that were produced from electrolytes with lower glue concentrations (1 mg L^{-1}) over a range of sodium silicate levels (0, 2, 4 and 15 mg L^{-1}) and the concentration of licorice was kept

constant at 5 mg L^{-1}. In the case where the influence of licorice is studied, sodium silicate was kept constant at 2 mg L^{-1} and licorice amounts used were 0, 5 and 15 mg L^{-1}. Analysis of the zinc sample produced with lower glue demonstrated that, as sodium silicate concentrations increased, the roughness per periodicity (δ/L_c) was more variable. Furthermore, the licorice study showed that, when there is 0 mg L^{-1} licorice in the electrolyte, the δ/L_c is more positive (i.e., rougher). In contrast, when licorice level is increased to 5 mg L^{-1}, there is a decrease in δ/L_c. However, further increasing the licorice levels to 15 mg L^{-1} produce samples that have similar δ/L_c values compared to those produced with electrolyte containing 5 mg L^{-1} licorice. This result indicates that a small amount of sodium silicate and licorice might act to produce morphologies with lower limiting roughness per periodicity. The data was presented on a ternary plot to observe influence of relative concentrations of additives on δ/L_c. The ternary plot showed a clear divide between additive conditions that resulted in lower and higher values of δ/L_c relative to the overall median. When the electrolytes contained 30% or less glue and a wide range of sodium silicate and licorice, we observe morphologies with δ/L_c less than overall median. This prompted more experiments to fill in missing points on the ternary diagram.

7.5: Ternary diagrams: %CE, δ/Lc, and γ

Ternary diagrams were used to make comments on the influence of relative composition of additives in the zinc electrolyte on current efficiency, roughness per periodicity (δ/L_c), and its rate of growth (i.e., optical roughness, γ). Samples were produced from a variety of additive combinations with a range of deposition time within each set. The current and

voltage data collected during deposition, coupled with weights measured after drying of samples, were used to calculate current efficiency. The results were plotted in a ternary diagram to display relative composition of additives versus %CE and δ/L_c and γ. Ternary diagrams showed that low glue, low sodium silicate and large licorice levels (i.e., section 4) will produce samples with large CE and α values and smooth 30 minute deposits (indicated by the low δ/L_c values). However, the growth exponent (γ) indicates that these surfaces may become rougher than other samples over prolonged deposition times. In contrast, electrolytes with low glue, high sodium silicate and low licorice levels (i.e., section 1) will produce samples with large CE, low α values and rougher 30 minute deposits (indicated by the larger δ/L_c values). The growth exponent (γ) indicates that these surfaces may be smoother than other samples over prolonged deposition times.

In order to obtain more accurate and conclusive ternary diagrams describing the influence of relative concentration of each additive future studies will need to be conducted to have replicate data (i.e., 9 images per deposition condition) similar to those seen in Chapter 4, Sections 5.2 and 5.3.

References

[1] D.R. Lide, G. Baysinger, L.I. Berger, eds., CRC Handbook of Chemistry and Physics, 87th ed., Taylor and Francis, Boca Raton, FL., 2007.

[2] R.J. Sinclair, The Extractive Metallurgy of Zinc By, 13 (2005) 15–31.

[3] J. Leja, Surface Chemistry of Froth Flotation, Plenum Press, New York and London, 1982.

[4] M. Moats, E. Guerra, J.A. Gonzalez, Zinc electrowinning and opperating prodecdures, in: Zinc Lead Metall., 2008: pp. 309–314.

[5] E. Guerra, M. Bestetti, Physicochemical Properties of ZnSO4-H2SO4-H2O electrolyte of Relevance to Zinc Electrowinning, J. Chem. Eng. Data. 51 (2006) 1491–1497.

[6] A. C. Scott, R.M. Pitblado, G.W. Barton, a. R. Ault, Experimental determination of the factors affecting zinc electrowinning efficiency, J. Appl. Electrochem. 18 (1988) 120–127. doi:10.1007/BF01016215.

[7] V.A. Ettel, B.V. Tilak, Comprehensive Treatise of Electrochemistry: Electrolytic Refining and Winning of Metals, Plenum Press, New York, 1981.

[8] J.O.B. and G.A. Razumney, Fundamental Aspects of Electrocrystallization, 1st ed., Plenum Press, 1967. doi:10.1136/pgmj.53.616.112-b.

[9] F.C. Walsh, M.E. Herron, Electrocrystallization and electrochemical control of

crystal growth: fundamental considerations and electrodeposition of metals, J. Phys. D. Appl. Phys. 24 (1991) 217–225. doi:10.1088/0022-3727/24/2/019.

[10] R. Parsons, Adv. Electrochem. Electrochem. Eng., 1961.

[11] D. Dhak, M. Mahon, E. Asselin, a. Alfantazi, Characterizing industrially electrowon sticky zinc deposits, Hydrometallurgy. 111–112 (2012) 136–140.

[12] D.J. Robinson, T.J. O'Keefe, On the effects of antimony and glue on zinc electrocrystallization behaviour, J. Appl. Electrochem. 6 (1976) 1–7.

[13] A.C. Beshore, B.J. Flori, G. Schade, T.J. O'Keefe, Nucleation and growth of zinc electrodeposited from acidic zinc solutions, J. Appl. Electrochem. 17 (1987) 765–772.

[14] T. Greul, J. Gerdenitsch, C. Commenda, R. Sagl, M. Arndt, J. Duchoslav, et al., Coating substrate relationship after initial electrolyte contact in the electrodeposition of zinc on steel, Surf. Coatings Technol. 253 (2014) 8–13.

[15] S. Khorsand, K. Raeissi, M.A. Golozar, Effect of Oxalate Anions on Zinc Electrodeposition from an Acidic Sulphate Bath, J. Electrochem. Soc. 158 (2011)

[16] S. Nusen, N. Yottawee, S. Daopiset, T. Chairuangsri, The role of surface grinding, intermetallic precipitates and halide ions on zinc deposition and adhesion on aluminium cathode in zinc electrowinning, Hydrometallurgy. 113–114 (2012) 143–154.

[17] J. Pan, Y. Wen, J. Cheng, J. Pan, Z. Bai, Y. Yang, Zinc deposition and dissolution in

sulfuric acid onto a graphiteresin composite electrode as the negative electrode reactions in acidic zinc-based redox flow batteries, J. Appl. Electrochem. 43 (2013) 541–551.

[18] Ping Gu, R. Pascual, M. Shirkhanzadeh, S. Saimoto, J.D. Scott, The influence of Al substrate intermetallic precipitates, Hydrometallurgy. 37 (1995) 267–281.

[19] K. Raeissi, A. Saatchi, M.A. Golozar, J.A. Szpunar, Texture and surface morphology in zinc electrodeposits, J. Appl. Electrochem. 34 (2004) 1249–1258.

[20] B.C. Tripathy, S.C. Das, G.T. Hefter, P. Singh, Zinc electrowinning from acidic sulphate solutions Part II : E € ects of triethylbenzylammonium chloride, J. Appl. Electrochem. 28 (1998) 915–920.

[21] W. Zhang, G. Houlachi, Electrochemical studies of the performance of different Pb–Ag anodes during and after zinc electrowinning, Hydrometallurgy. 104 (2010) 129–131.

[22] O. Aaboubi, J. Douglade, X. Abenaqui, R. Boumedmed, J. Vonhoff, Influence of tartaric acid on zinc electrodeposition from sulphate bath, Electrochim. Acta. 56 (2011) 7885–7889.

[23] A.M. Alfantazi, D.B. Dreisinger, Foaming behavior of surfactants for acid mist control in zinc electrolysis processes, Hydrometallurgy. 69 (2003) 57–72.

[24] A.M. Alfantazi, D.B. Dreisinger, The role of zinc and sulfuric acid concentrations on zinc electrowinning from industrial sulfate based electrolyte, J. Appl. Electrochem.

31 (2001) 641–646.

[25] J.C. Ballesteros, P. Díaz-Arista, Y. Meas, R. Ortega, G. Trejo, Zinc electrodeposition in the presence of polyethylene glycol 20000, Electrochim. Acta. 52 (2007) 3686–3696.

[26] C.Y. Cheng, M.D. Urbani, P. Miovski, D. Kittelty, a. F. Otero, R.M. San Martín, Evaluation of saponins as acid mist suppressants in zinc electrowinning, Hydrometallurgy. 73 (2004) 133–145.

[27] S.C. Das, P. Singh, G.T. Hefter, The effects of 4-ethylpyridine and 2-cyanopyridine on zinc electrowinning from acidic sulfate solutions, J. Appl. Electrochem. 27 (1997) 738–744.

[28] D. Dhak, E. Asselin, S. DiCarlo, A. Alfantazi, An Investigation on the Effects of Organic Additivies on Zinc Electrowinning from Industrial Electrolyte, ECS Trans. 6 (2010) 267–280.

[29] P. Díaz-Arista, Y. Meas, R. Ortega, G. Trejo, Electrochemical and AFM study of Zn electrodeposition in the presence of benzylideneacetone in a chloride-based acidic bath, J. Appl. Electrochem. 35 (2005) 217–227.

[30] A. Gomes, M.I. da Silva Pereira, Zn electrodeposition in the presence of surfactants. Part I. Voltammetric and structural studies, Electrochim. Acta. 52 (2006) 863–871.

[31] K.O. Nayana, T. V. Venkatesha, Synergistic effects of additives on morphology, texture and discharge mechanism of zinc during electrodeposition, J. Electroanal.

Chem. 663 (2011) 98–107.

[32] A. Recéndiz, I. González, J.L. Nava, Current efficiency studies of the zinc electrowinning process on aluminum rotating cylinder electrode (RCE) in sulfuric acid medium: Influence of different additives, Electrochim. Acta. 52 (2007) 6880–6887.

[33] A.E. Saba, A.E. Elsherief, Continuous electrowinning of zinc, Hydrometallurgy. 54 (2000) 91–106.

[34] J. Torrent-Burgués, E. Guaus, Effect of tartaric acid in the electrodeposition of zinc, J. Appl. Electrochem. 37 (2007) 643–651.

[35] G. Trejo, H. Ruiz, R.O. Borges, Y. Meas, Influence of polyethoxylated additives on zinc electrodeposition from acidic solutions, J. Appl. Electrochem. 31 (2001) 685–692.

[36] X. Wu, Z. Liu, X. Liu, The effects of additives on the electrowinning of zinc from sulphate solutions with high fl uoride concentration, Hydrometallurgy. 141 (2014) 31–35.

[37] V.M. Alkatsev, M.I. Alkatsev, V.A. Lin, I. V Darchiev, Influence of Impurities in Electrolyte (Tin , Germanium , and Antimony) on Current Efficiency within Electrowinning of Zinc, Metall. Nonferrous Met. 55 (2014) 327–330.

[38] I. Ivanov, Increased current efficiency of zinc electrowinning in the presence of metal impurities by addition of organic inhibitors, Hydrometallurgy. 72 (2004) 73–

78.

[39] D.J. MacKinnon, J.M. Brannen, P.L. Fenn, Characterization of impurity effects in zinc electrowinning from industrial acid sulphate electrolyte, J. Appl. Electrochem. 17 (1987) 1129–1143.

[40] L. Mureşan, G. Maurin, L. Oniciu, G. Delia, Influence of metallic impurities on zinc electrowinning from sulphate electrolyte, Hydrometallurgy. 43 (1996) 345–354.

[41] T. Boiadjieva, M. Monev, A. A Tomandl, H. Kronberger, G. Fafilek, Electrochemical studies on Zn deposition and dissolution in sulphate electrolyte, J. Solid State Electrochem. (2008) 671–677.

[42] J. Yu, L. Wang, L. Su, X. Ai, H. Yang, Temperature effects on the electrodeposition of zinc, J. Electrochem. Soc. 150 (2003) C19–C23.

[43] Q.B. Zhang, Y.X. Hua, T.G. Dong, D.G. Zhou, Effects of temperature and current density on zinc electrodeposition from acidic sulfate electrolyte with [BMIM]HSO4 as additive, J. Appl. Electrochem. 39 (2009) 1207–1216.

[44] A.R. Ault, E.J. Frazer, Effects of certain impurities on zinc electrowinning in high-purity synthetic solutions, J. Appl. Electrochem. 18 (1988) 583–589.

[45] V.F.C. Lins, M.M.R. Castro, C.R. Araújo, D.B. Oliveira, Effect of nickel and magnesium on zinc electrowinning using sulfate solutions, Brazilian J. Chem. Eng. 28 (2011) 475–482.

[46] D.J. Mackinnon, J.M. Brannen, Zinc deposit structures obtained from high purity

synthetic and industrial acid sulphate electrolytes with and without antimony and glue additions, J. Appl. Electrochem. 7 (1977) 451–459.

[47] D.J. Mackinnon, R.M. Morrison, J.E. Mouland, P.E. Warren, The effects of Dowfroth, antimony and Saponin on zinc electrowinning from Kidd Creek electrolyte, J. Appl. Electrochem. 21 (1991) 213–220.

[48] G. Hodjaoglu, I. Ivanov, Zinc recovery from sulphate electrolytes , containing copper and ferrous ions, Bulg. Chem. Comm. 43 (2011) 37–41.

[49] D.J. MacKinnon, J.M. Brannen, V.I. Lakshmanan, The effects of chloride ion and organic extradants on electrowon zinc deposits, J. Appl. Electrochem. 10 (1980) 321–334.

[50] D. Majuste, E.L.C. Martins, A.D. Souza, M.J. Nicol, V.S.T. Ciminelli, Role of organic reagents and impurity in zinc electrowinning, Hydrometallurgy. 152 (2015) 190–198.

[51] T. Robinson, K.C. Sole, M.S. Moats, F.K. Crundwell, M. Moritmitsu, L. Palmu, Developments in Base Metal Electrowinning Cellhouse Design, Electrometall. 2012. (2012) 147–156.

[52] D. Dhak, M. Mahon, E. Asselin, A. Alfantazi, The effects of mixtures of acid mist suppression reagents on zinc electrowinning from spent electrolyte solutions, Hydrometallurgy. 108 (2011) 1–10.

[53] C.L. Pearson, Handbook of Adhesive Technology, Revised and Expanded, CRC

Press (Marcel Dekker), United States of America, 2003.

[54] R.C. Kerby, H.E. Jackson, Y. Wang, Evaluation of organic additives for use in zinc electrowinning, Metall. Trans. B. 8 (1977) 661–668.

[55] J. Speight, Chemical and process design handbook, McGraw-Hill, New York, 2002.

[56] J.J. Henderson, H.L. Montague, Process for Electrowinning Zinc, 2863810, 1958.

[57] H.J. Schwartz, Fuel cells - From Fundamentals to Applications, 2006.

[58] L.A. Baltina, O. Kunert, A.A. Fatykhov, R.M. Kondratenko, High-Resolution 1H and 13C NMR of Glycyrrhizic Acid and Its Esters, Chem. Nat. Compd. 41 (2005) 432–435.

[59] T. Biegler, "Interpretation and Polarization Measurements in Zinc Electrolyte," Application of Polarization Measurements in the Control of Metal Deposition, Elsevier Science, Amsterdam, 1984.

[60] T.N. Andersen, R.C. Kerby, T.J. O'Keefe, Techniques for Control Techniques for Industrial Electrodeposition from Aqueous Solutions, J. Met. 37 (1985) 36–43.

[61] R.C. Kerby, Application of Polarization Measurements in the Control of Metal Deposition, Elsevier, New York, 1984.

[62] L. Reimer, Scanning Electron Microscopy, Springer-V erlag Berlin Heidelberg GmbH, 1998.

[63] G. Binnig, C.F. Quate, Atomic Force Microscope, Phys. Rev. Lett. 56 (1986) 930–

933.

[64] W.R.B. and N. Hilal, Atomic Force Microscopy in Process Engineering, 2009.

[65] F. Moreno-Herrero, J. Gomez-Herrero, AFM: Basic Concepts, At. Force Microsc. Liq. Biol. Appl. (2012) 1–34.

[66] R. Schmitz, AFM Atomic Force Microscopy, (2005) 1–24.

[67] S.H.C. Cohen, M.T. Bray, M.L. Lightbody, Atomic Force Microscopy/Scanning Tunneling Microscopy, n.d.

[68] R.S. Williams, W.M. Tong, Kinetics of Surface Growth: Mechanisms of Smoothening and Roughening, Annu. Rev. Phys. Chem. 45 (1994) 401–438.

[69] A.-L. Barasbasi, H.E. Stanley, Fractal Concepts In Surface Growth, 1st ed., Cambridge University Press, New York, 1995.

[70] T. Zhao, D. Zagidulin, G. Szymanski, J. Lipkowski, Application of atomic force microscopy and scaling analysis of images to predict the effect of current density, temperature and leveling agent on the morphology of electrolytically produced copper, Electrochim. Acta. 51 (2006) 2255–2260.

[71] M. Hiane, J. Ebothé, Growth velocity and the topography of Ni-Zn binary alloy electrodeposits, Eur. Phys. J. B. 22 (2001) 485–495.

[72] T.J. Oliveira, F.D.A. Aarão Reis, Effects of grains' features in surface roughness scaling, J. Appl. Phys. 101 (2007) 1–7.

[73] T.J. Oliveira, F.D.A. Aarão Reis, Roughness exponents and grain shapes, Phys. Rev. Lett. 83 (2011) 1–7.

[74] S.S. Mahboob, K. Swanson, J.A. Gonzalez, J.L. Shepherd, On the use of atomic force microscopy and scaling analysis to quantify the roughness of zinc electrodeposits produced from an industrial acid sulfate electrolyte containing glue, J. Appl. Electrochem. 46 (2016) 1–11.

[75] S.S. Mahboob, J.L. Shepherd, J.A. Gonzalez, IMPC 2016 : XXVIII International Mineral Processing Congress Proceedings, (2016) 1–11.

Appendix

A. Difference between using standard error and standard deviation and its influence on critical length and ratio of limiting roughness per critical length *(δ/L_c)*.

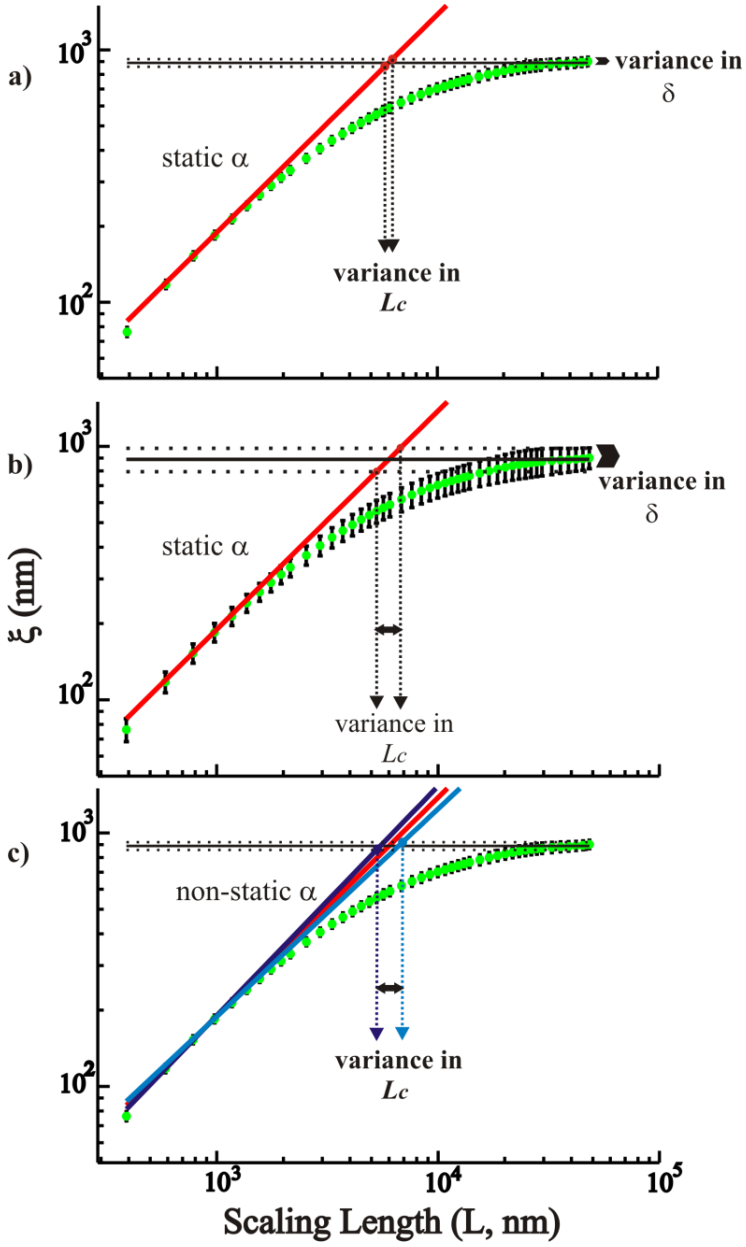

In this plot, nine scaling trends of 30 minute data (30G, 2.7SS, 9L) shown in Chapter 4 are averaged. Error bars in a) and c) represent standard error (i.e., the standard deviation

divided by the square root of sample size), and in b) they represent standard deviation (i.e., the approach used in the thesis). A red line in the plot represents a static α; the variation due to standard error is shown by light blue (lower limit) and dark blue (upper limit) in c). The limits of a non-static α was obtained through linear regression using Excel LINEST function. From this plot, it can be noted that using standard error results in the smallest variance (plots a and c) in the limiting roughness (δ), whereas using standard deviation results in larger variance (plot b – the approach used in this thesis). Recall that values of critical length are extracted from the intercept of the α and δ lines. As such, when using a static α and standard error (plot a), it is clear that the variance in L_c is small. In contrast, when standard deviation is used with a static α (plot b), we observe a larger variance in L_c. Moreover, if a non-static α (plot c) is used with standard error, the variance in L_c is the largest.

Note that the limiting roughness (δ) is extracted independently from the plateau of the scaling plots, thus this approach will not underestimate values of δ. While it underestimates values of L_c and δ/L_c, it does not to the extent it would if a static α and standard error were used. Lastly, if a non-static α was used with standard error it would result in overestimates. As such, in order not to overestimate and underestimate values of Lc and δ/Lc, the approach of static α with standard deviation is applied in the analysis of error in this thesis. These results are shown in bar plots below for clarity.

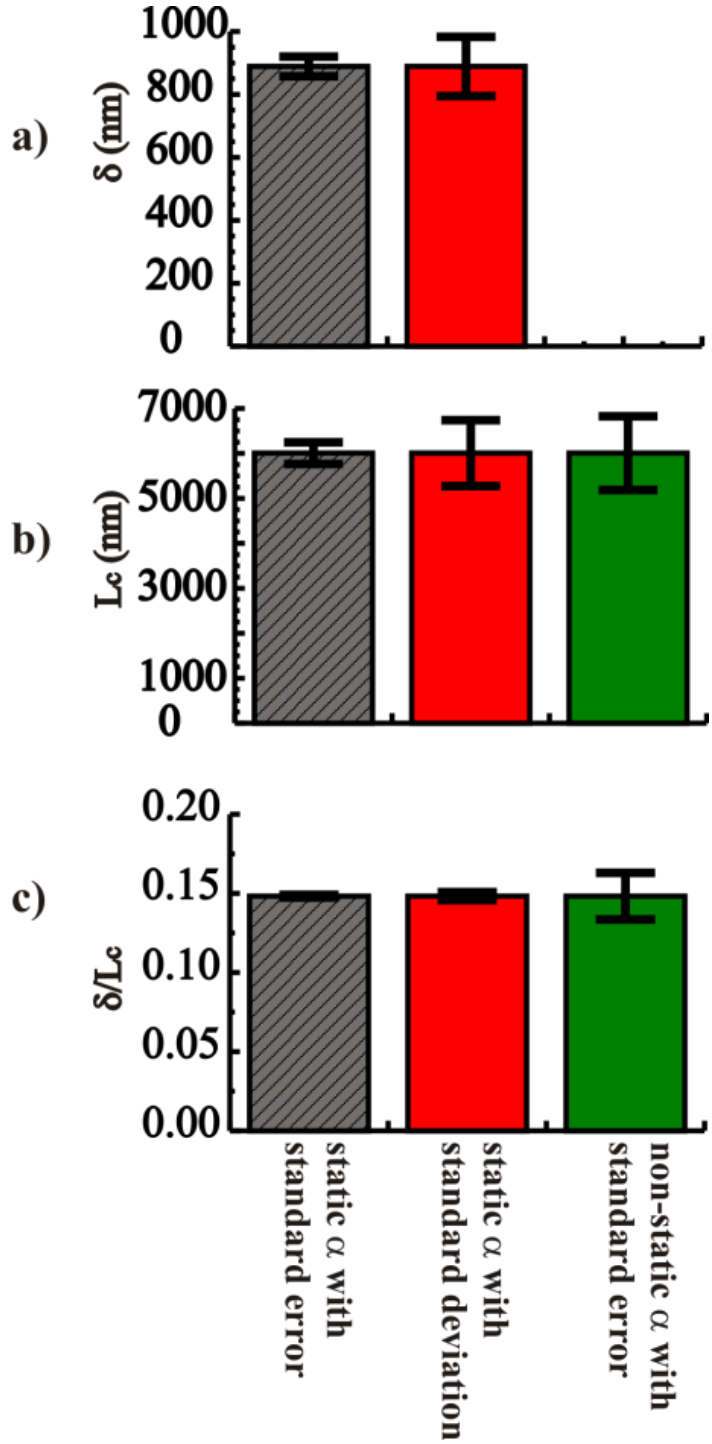
a)
δ (nm)
1000
800
600
400
200
0
b)
Lc (nm)
7000
5000
3000
1000
0
c)
δ/Lc
0.20
0.15
0.10
0.05
0.00
static α with standard error
static α with standard deviation
non-static α with standard error

B. Results of log δ and log Lc versus log deposition time

In this plot, the results of limiting roughness and critical length from performing scaling analysis on images of samples produced from electrolyte containing a range of sodium silicate (0 to 27 mg/L) with 30 mg/L glue and 9 mg/L licorice. These plots demonstrate that values of δ and Lc for each electrolyte condition results in similar values and makes it difficult to base the analysis on these parameters alone. Therefore, the best way to analyze the influence of levelling additives is to compare the ratio of these two parameters instead.

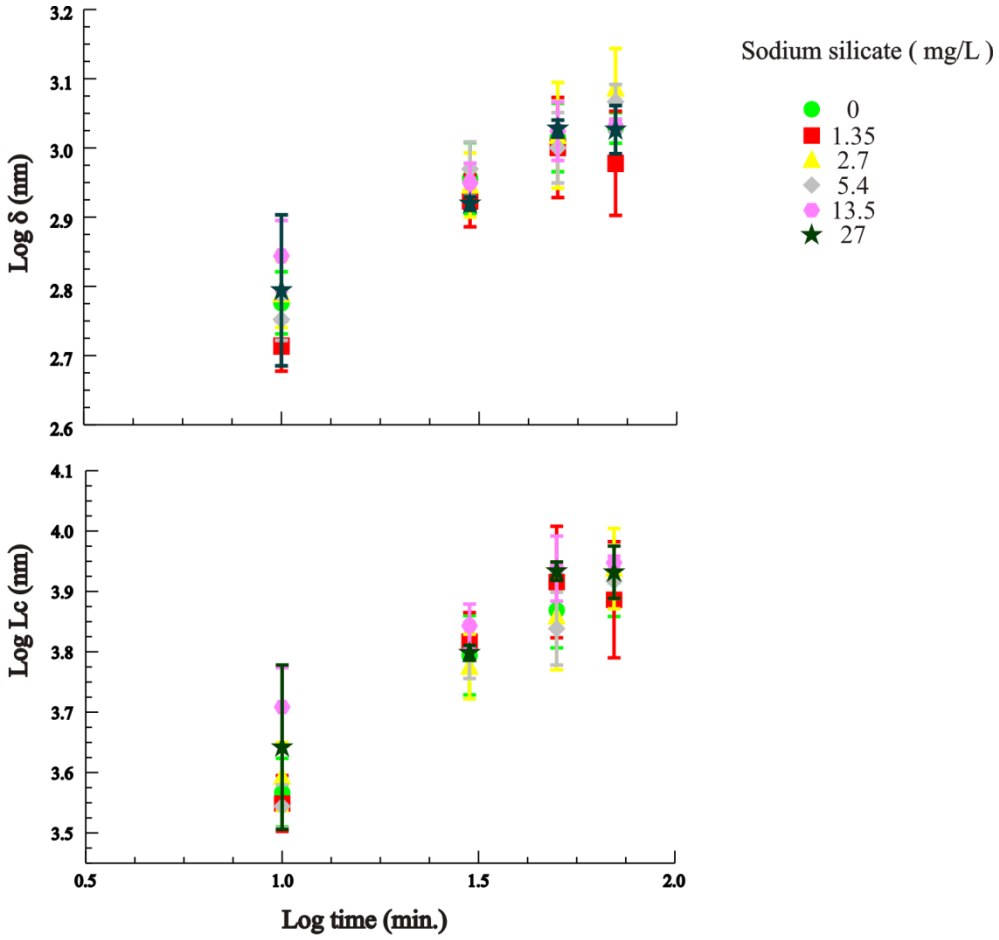

C. List of data points not used in ternary diagram and example of data with poor fit

Additive amounts (mgL^{-1})	Deposition times (minutes)	Reason for not including in ternary diagram
2G_0.5SS_7.5L	10, 20, 30	poor data fit
3.5G_1SS_5.5L	10, 20, 30	2 α
5G_2.5SS_2.5L	10, 20, 30	2 α
5G_6SS_9L	10, 20, 30	poor data fit
6G_30SS_9L	10, 30, 50	2 α
1.5G_1.35SS_9L	10, 30, 50	2 α
1G_0SS_5L*	10,20,30,50	2 α and poor fit
30G_13.5SS_9L*	10, 30, 50, 70	2 α
30G_27SS_9L*	10, 30, 50	2 α
37.5G_2.7SS_9L+	30	2 α
60G_2.7SS_9L+	30	2 α
	+ data shown in Chapter 4 * data shown in Chapter 5	

Here is an example of a data set with poor fit when log L_c is plotted versus log (time). This data set was a result of analysis of zinc samples produced from an electrolyte with 1 mg/L glue, 0 mg/L sodium silicate and 5 mg/L licorice. When a data set resulted in one or more point and their error bar appeared to be outside the linear regression trend, it was considered a bad fit and was not included in the ternary diagrams.

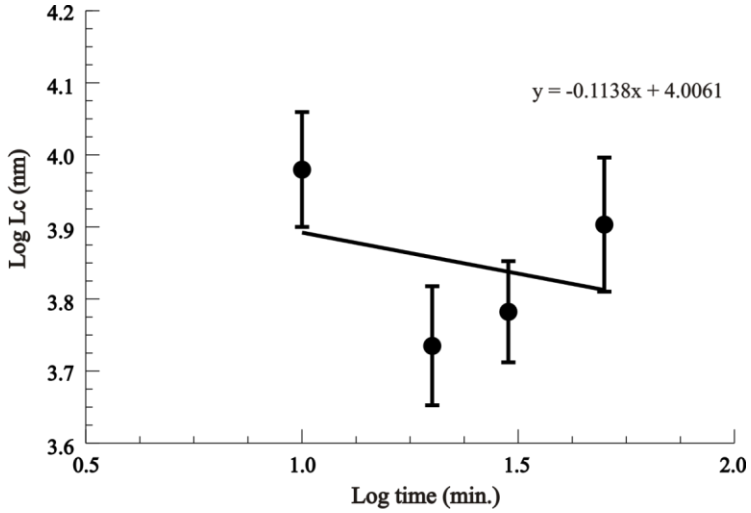

D. Ternary diagram showing δ and Lc of the 30 minute deposits and β, β/α of studies presented in Chapter 6

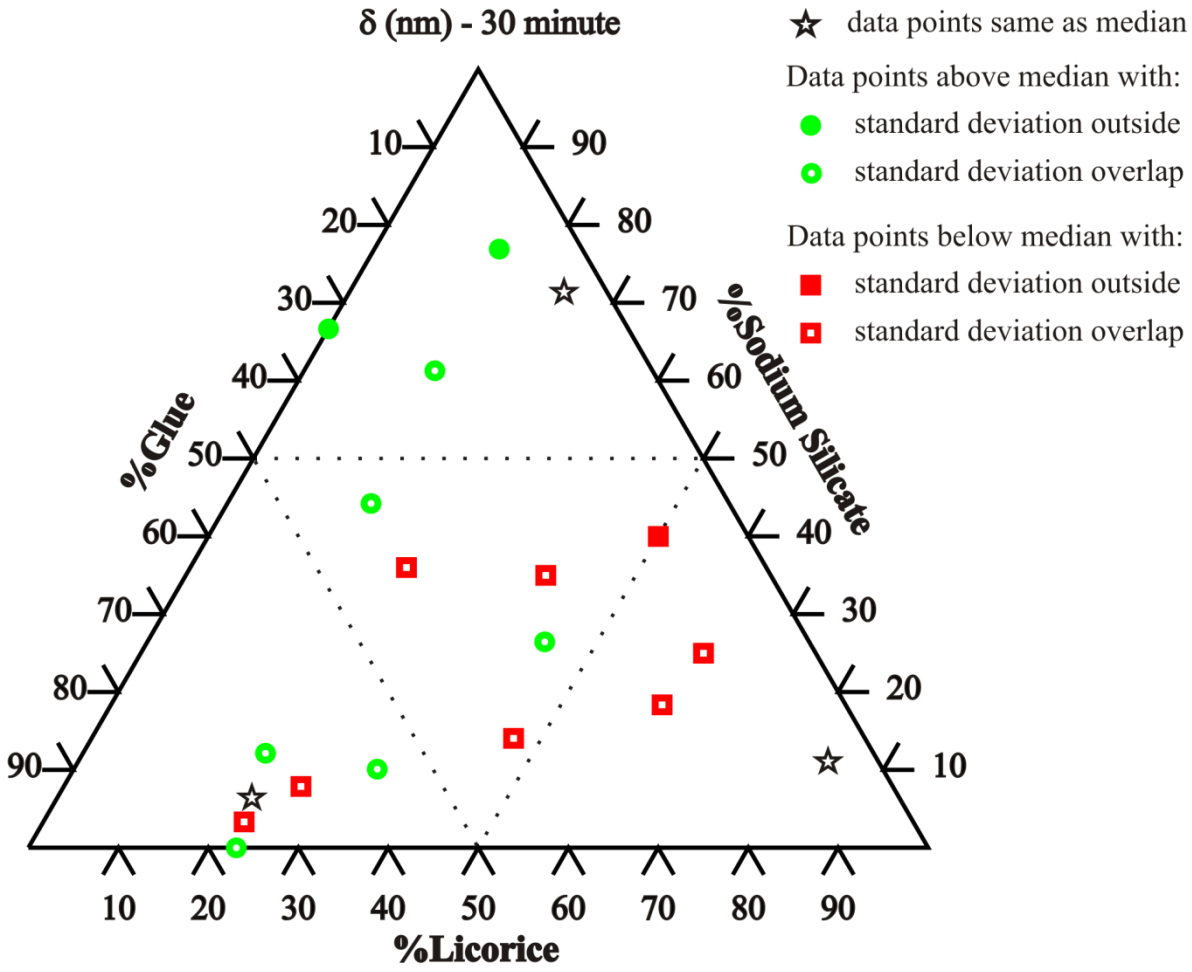

Note: the results shown on this ternary plot were obtained with the concentration ranges shown in parentheses on Figure 39 and may not necessarily extend to systems with a different concentration range.

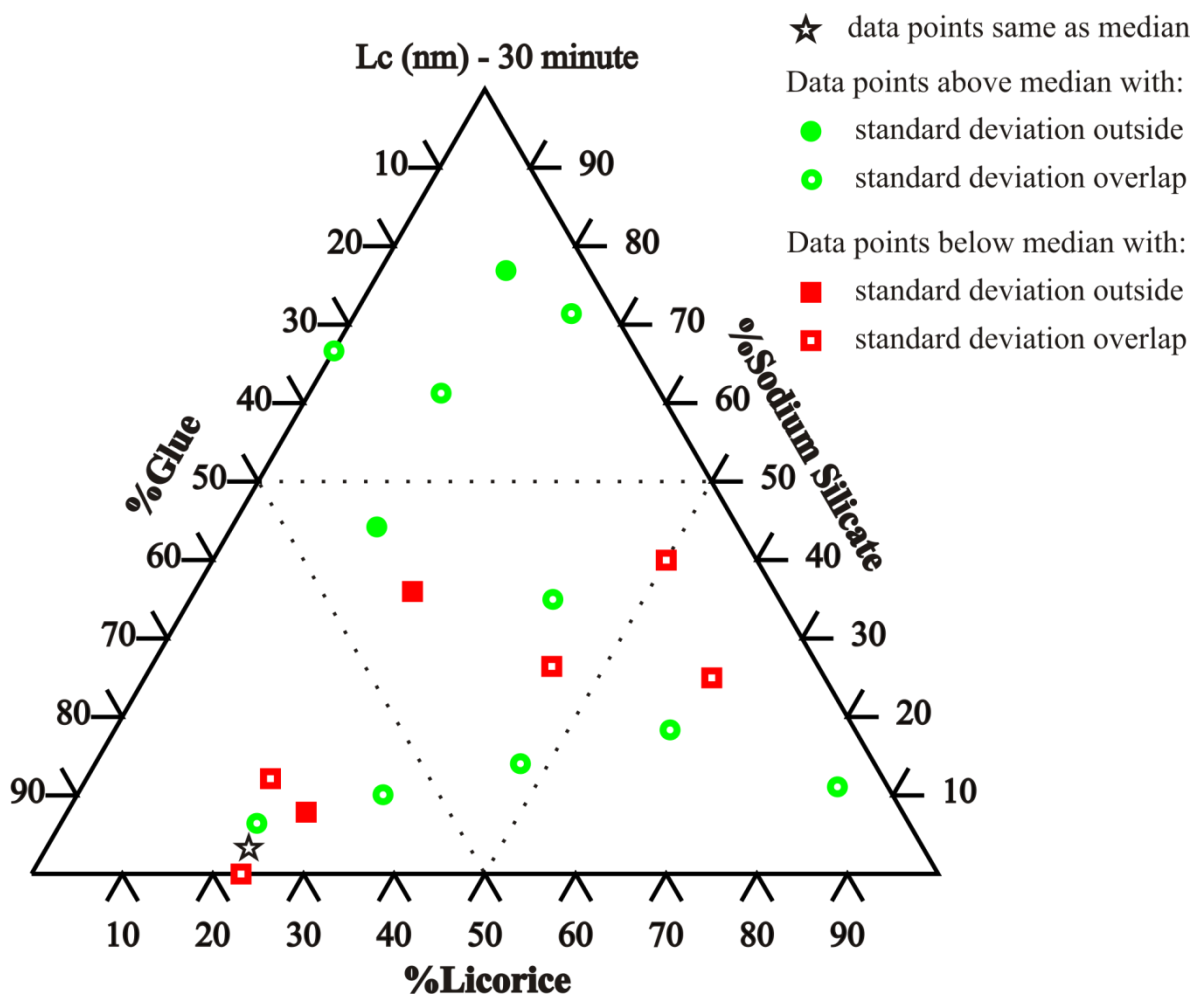

Note: the results shown on this ternary plot were obtained with the concentration ranges shown in parentheses on Figure 39 and may not necessarily extend to systems with a different concentration range.

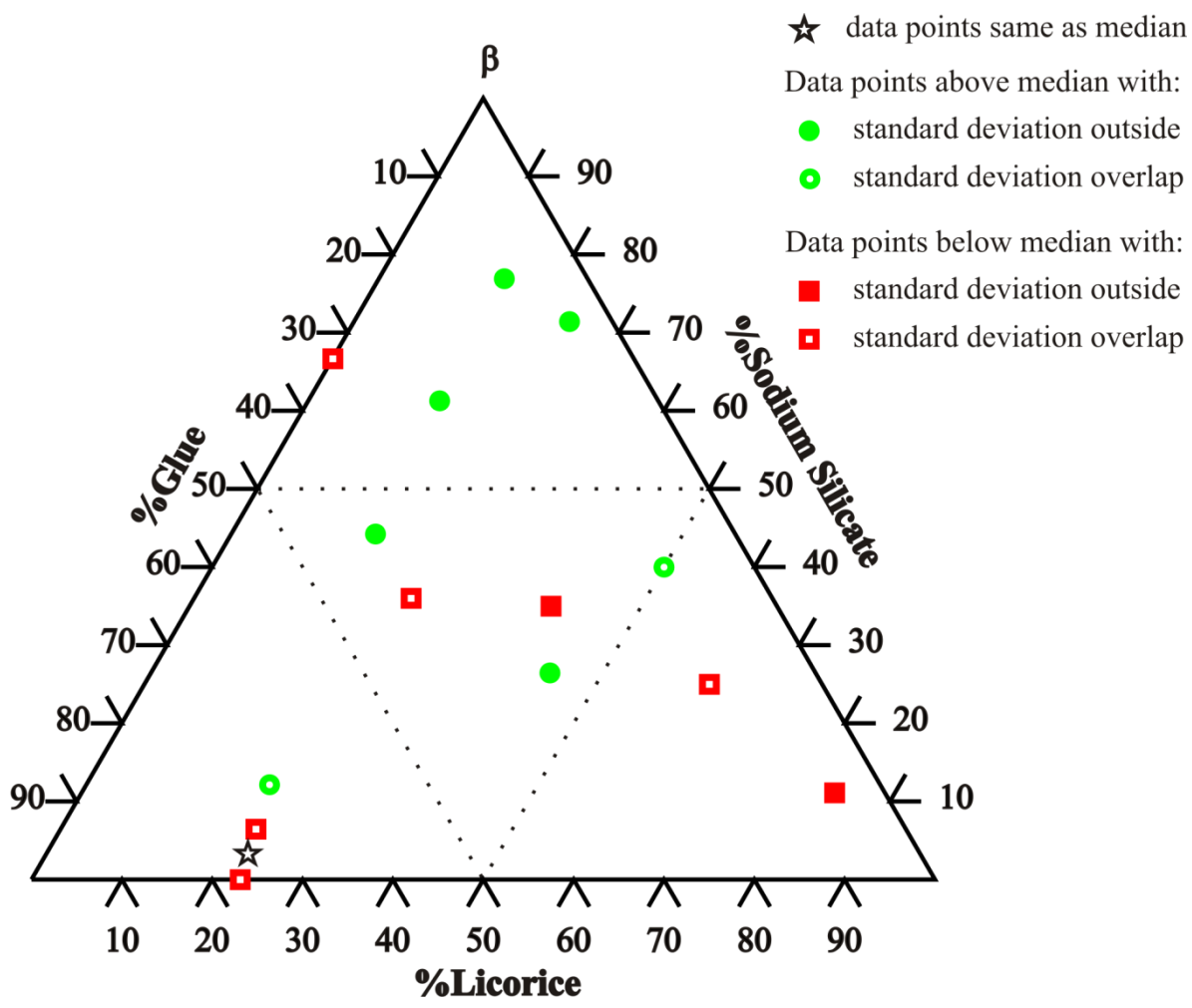

Note: the results shown on this ternary plot were obtained with the concentration ranges shown in parentheses on Figure 39 and may not necessarily extend to systems with a different concentration range.

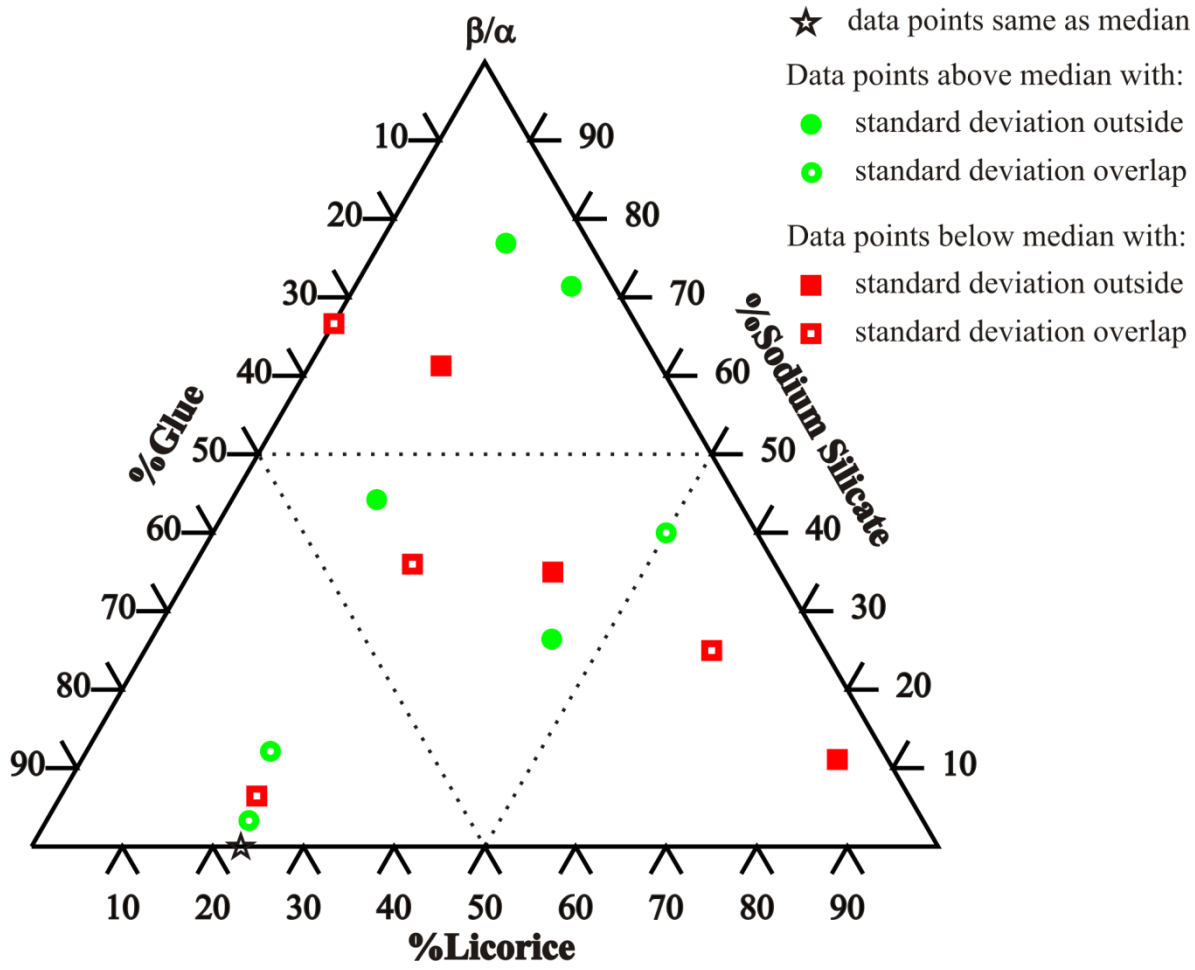

Note: the results shown on this ternary plot were obtained with the concentration ranges shown in parentheses on Figure 39 and may not necessarily extend to systems with a different concentration range.